iJERGS International Journal of Engineering Research And General Science

Journal which deals with research, Innovation and Originality

International Journal Of Engineering Research and General Science

ISSN 2091 - 2730

ISSN 2091-2730

Table of Content

CHIEF EDITOR BOARD

Message from IJERGS

This is the Second Issue of the Sixth Volume of International Journal of Engineering Research and General Science. A total of 13 research articles are published and we sincerely hope that each one of these provides some significant stimulation to a reasonable segment of our community of readers.

In this issue, we have focused mainly on the Innovative Ideas. We also welcome more research oriented ideas in our upcoming Issues.

Author's response for this issue was really inspiring for us. We received many papers from many countries in this issue but our technical team and editor members accepted very less number of research papers for the publication. We have provided editors feedback for every rejected as well as accepted paper so that authors can work out in the weakness more and we shall accept the paper in near future.

Our team have done good job however, this issue may possibly have some drawbacks, and therefore, constructive suggestions for further improvement shall be warmly welcomed.

IJERGS Team,

International Journal of Engineering Research and General Science

E-mail – feedback@ijergs.org

Design and implementation of Open & Close Loop Speed control of Three Phase Induction Motor Using PI Controller

Ibtisam Naveed[1], Adnan Sabir[2]

[1](Electrical Engineering, NFC institute of Engineering and Fertilizer Research Faisalabad, Pakistan)
[2](Software Engineering, COMSATS institute of information Technology, Sahiwal Pakistan)

ABSTRACT- The induction motors were characterized by complex, highly non-linear and time-varying dynamics, and hence their speed control is a challenging problem in the industry. The aim of this paper is to present the speed control of three phase induction motors by variable frequency drive. The variable frequency drive for induction motors is achieved using SPWM which provide better efficiency and higher performance. The motor speed is investigated both at fixed load and variable load. Moreover a close loop PI controller was designed at rated load based on dynamic behavior of error signal. It has been found that by designing a proper PI controller the motor starting current is reduced significantly. Moreover at rated torque efficiently speed of motor can be controlled. PI speed controller not help to reduce dynamic performance of the system but also help to reduce the steady state error, the error sensibility, high performance and smooth speed response. The complete mathematical model of the system is described and simulated in MATLAB/SIMULINK. The simulation results provide a smooth speed response and high performance under various dynamic operations.***Keywords*—** Induction Motor, PI controller, SPWM technique, Voltage Source Inverter (VSI)

1. Introduction

Induction motor is the most widely used in industry because of its high robustness, reliability, low cost, high efficiency and good self starting capability. Moreover during the last few years, feasible controls of induction motor has received a lot of attention with the development of Power electronic devices like IGBT, MOSFET etc. and make an active research area for engineers. The speed control of induction motor is more important to achieve maximum torque and efficiency [1-2]. Various methods based on speed and torqueses with different technique are deployed for speed control of induction motors. These methods mostly are scalar control, vector or field-oriented control, direct and flux control, sliding mode control, Fuzzy logic Control (FLC) and the adaptive control [3-6].Direct Torque Control (DTC) based method gives faster and robust responses of various parameters in the induction motors but the output responses of torque and flux are noisy [7]. FLC based proportional controller (PI) has high accuracy and less circuit complexity. However FLC controllers are less sensitive to system parameters variations and therefore difficult to achieve robustness [8]. The benefit of SPWM technique is that not only provide better efficiency but also help to increase the performance of induction motor when compared with fixed frequency motor drive. The advantage of using SPWM help to shrink the harmonic content of output voltage compared to single pulse width modulation and multi-pulse modulation. In this paper, a three phase inverter, controlled by SPWM technique driving a three phase induction motor at fixed and variable load is presented. The harmonic analysis also performed using FFT tool to observe the harmonics content in Voltage Source Inverter. Moreover the close loop system PI controller is designed which help to maintain the speed of the motor at rated torque.

2. Modeling of Induction Motor

The dynamic model is used to obtain the transient and steady state behavior of induction motor. Analysis of the dynamic behavior of Induction Motor are described the equation of induction motor. The stator and rotor voltage equation of motor is described as:

$$\begin{aligned} v_{ds} &= R_s i_{ds} - \omega_s \psi_{qs} + p\psi_{ds} \\ v_{qs} &= R_s i_{qs} + \omega_s \psi_{ds} + p\psi_{qs} \end{aligned} \qquad (1)$$

Where $R_s i_{ds}$ is stator winding voltage drop, $\omega_s \psi_{qs}$ is speed voltage term and $p\psi_{qs}$ is transient term.

$$\begin{aligned} v_{dr} &= R_r i_{dr} - s\omega_s \psi_{qr} + p\psi_{dr} \\ v_{qr} &= R_r i_{qr} + s\omega_s \psi_{dr} + p\psi_{qr} \end{aligned} \qquad (2)$$

Where $s\omega_s\psi_{dr}$ is rotor speed voltage created in the Rotor windings moving at slip speed w.r.t to the synchronously rotating flux wave. Power input to stator and rotor equations described as:

$$P_s = v_{ds}i_{ds} + v_{qs}i_{qs} \quad (3)$$

$$P_r = v_{dr}i_{dr} + v_{qr}i_{qr} \quad (4)$$

The torque and Speed equation is described as:

$$T_e = \frac{3}{2}\left(\frac{P}{2}\right)\left(\lambda_{qr}I_{dr} - \lambda_{dr}I_{qr}\right)$$
$$\omega_r = \int \frac{P}{2*J}\left(T_e - T_L\right) \quad (5)$$

Where, P denote the no. of poles ; J: moment of inertia ,after driving the torque and speed equation in terms of dq flux linkage and current of the stator, the dq axis transformation should now be applied to the machine input(stator) voltage [9].

2.1 Block diagram of open loop system

The block diagram of system consists of three main parts. The DC voltage source, Voltage Source inverter and three phase induction motor. The output of Voltage source inverter can be found using this equation.

$$V_{rms} = 0.612 * m * V_{dc} \quad (6)$$

Where m is a modulation index of VSI and V_{dc} is the DC voltage.

The speed and driving Torque of motor can be found as

$$Ns = \frac{120 * f}{P} \quad (7)$$

Where Ns is synchronous speed in rpm, f is frequency in Hz and P is the No. of poles.

$$T_n = \frac{P_m}{w} \quad (8)$$

Where P_m is motor power in watt and w is rad/sec and T_n is in Nm.

ISSN 2091-2730

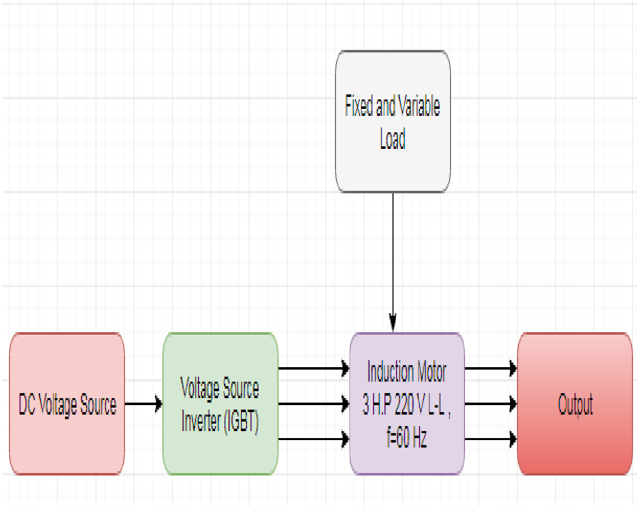

Fig. 2.1 The block diagram of open loop speed control of three phase induction motor

2.1.1 MATLAB/ Simulink Model implementation at rated load

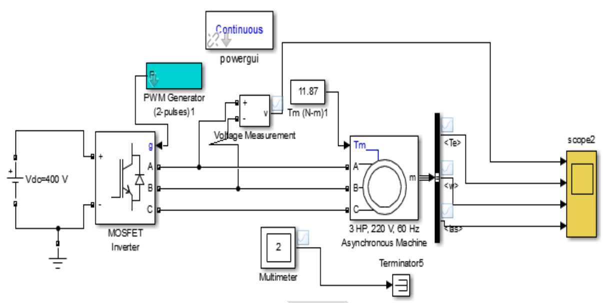

Fig. 2.2 An open loop Matlab/Simulink model for speed control of three phase induction motor at fixed/rated load

The nominal voltage 220 V_{rms} (L-L) for the input of three phases IM is calculated by Eq. (6) which is a function of dc voltage and modulation index factor (m). The synchronous speed of induction motor is calculated using Eq. (7) which is 1800 rpm (188.496 rad/sec). The nominal torque for IM is calculated using Eq. (8) which is 11.87 (Nm). For the sake of simplicity and check the effect of speed of IM at rated and variable load the PWM is generated by build in block by keeping carrier frequency at 1080 Hz. The block has been discretized so that the pulses change at multiples of the specified time step. A time step of 10 µs corresponds to +/- 0.54% of the switching period at 1080 Hz.

2.1.1.1 Simulation Result of open loop speed control of IM at rated load

At starting the motor speed increase to 181.8 rad/sec (1736 rpm) and then decrease and reaches its steady-state value of 175.5 rad/s (1675 rpm) after 0.1 s at rated load 11.87 Nm. At starting, the magnitude of the 60 Hz current increase gradually and reaches to steady state value of 12 A peak (8.48 A RMS). As expected, the magnitude of the 60 Hz voltage contained in the chopped wave stays at 311 V.

Also notice that at starting the electromagnetic torque reaches at highest value of 32 Nm and come to steady state at a value of 11.87 Nm corresponding to the load torque at nominal speed. Moreover it is noticed that all the harmonics (multiples of the 1080 Hz switching frequency) are filtered by the stator inductance, so that the 60 Hz component is dominant.

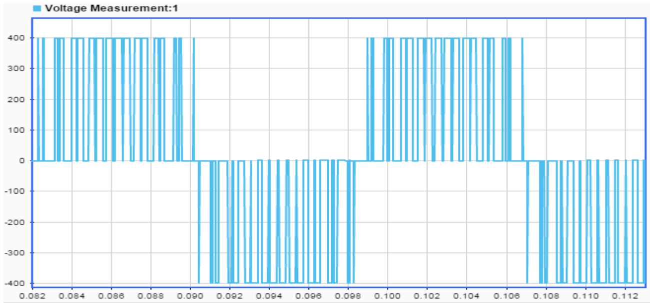

Fig. 2.3 RMS Line voltage at the output of VSI

Fig. 2.3 An open loop Matlab/Simulink model for speed control of three phase induction motor at fixed/rated load

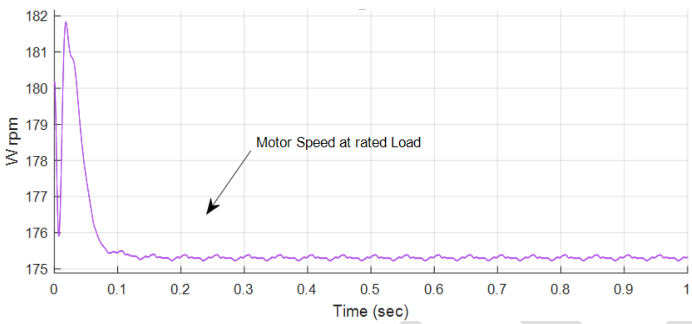

Fig. 2.4 Nominal speed of IM at rated load

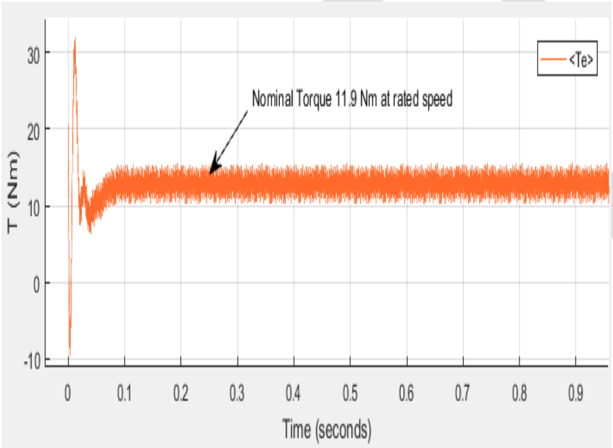

Fig. 2.5 Nominal Electromagnetic torque of IM at rated speed

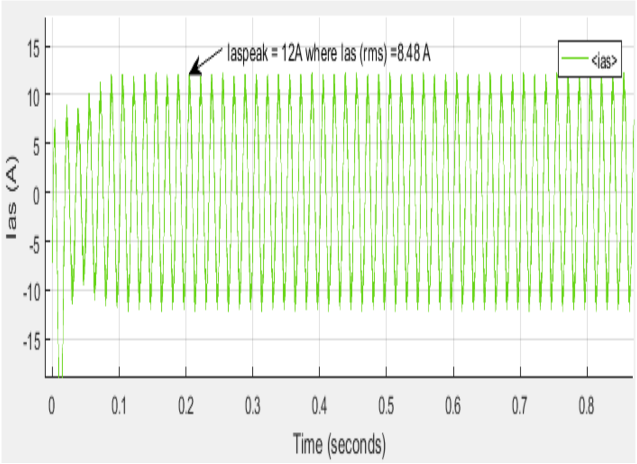

Fig. 2.6 Stator current of IM at rated load

The internal measurement of VSI block is done by millimeter. The simulation result is carried for 20 msec. A positive current indicate that a current is flowing in the MOSFET/IGBT while a negative current indicate that the current flowing in the antiparallel diode.

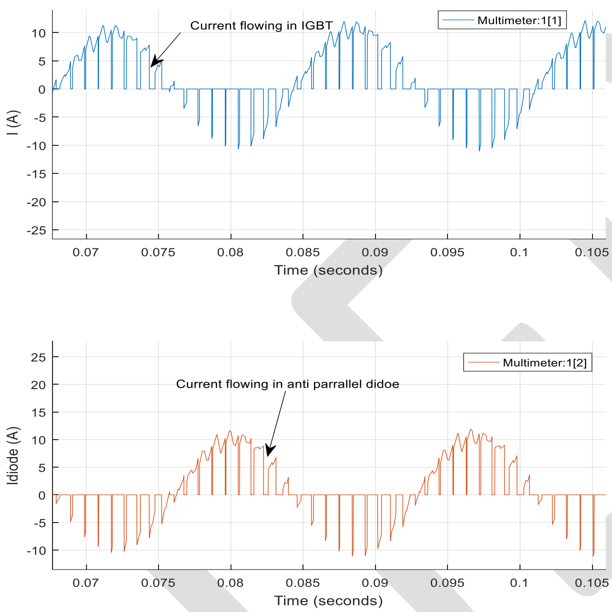

Fig. 2.7 Internal current flowing in the IGBT

2.1.1.2 MATLAB/ Simulink Model implementation at variable load

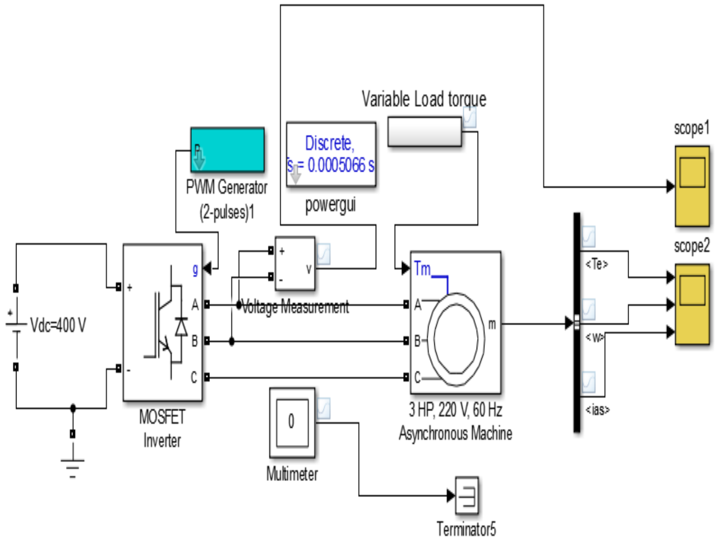

Fig. 2.8 An open loop Matlab/Simulink model for speed control of three phase induction motor at variable load

By keeping above all parameter same, the variable load at the input of motor is applied as follows;

Tm = 0 Nm $\quad 0 < t < 0.5$

Tm = 11.87 NM $\quad t > 0.5$

2.1.1.3 **Simulation Result of open loop speed control of IM at variable load**

The simulation results of three phase IM at variable load is shown indicate that At starting the motor speed increase to 192.7 rad/sec (1840 rpm) because of inertia and inrush current and eventually decrease and reach a value of 187.6 rpm (1791 rpm) which is slight close to synchronous speed for interval of $0 < t < 0.5$. As load on motor increase then speed of motor decrease and reach its steady-state value of 175.5 rad/s (1675 rpm) after 0.5 s corresponding load 11.87 Nm. At interval $0 < t < 0.5$ the magnitude of the 60 Hz current observed 4.836 peak (3.4195 A RMS) and increase gradually with increasing load and reaches to steady state value of 12 A peak (8.48 A RMS) for interval $t > 0.5$. As expected, the magnitude of the 60 Hz voltage contained in the chopped wave stays at 311 V.

Moreover it is noticed that all the harmonics (multiples of the 1080 Hz switching frequency) are filtered by the stator inductance, so that the 60 Hz component is dominant.

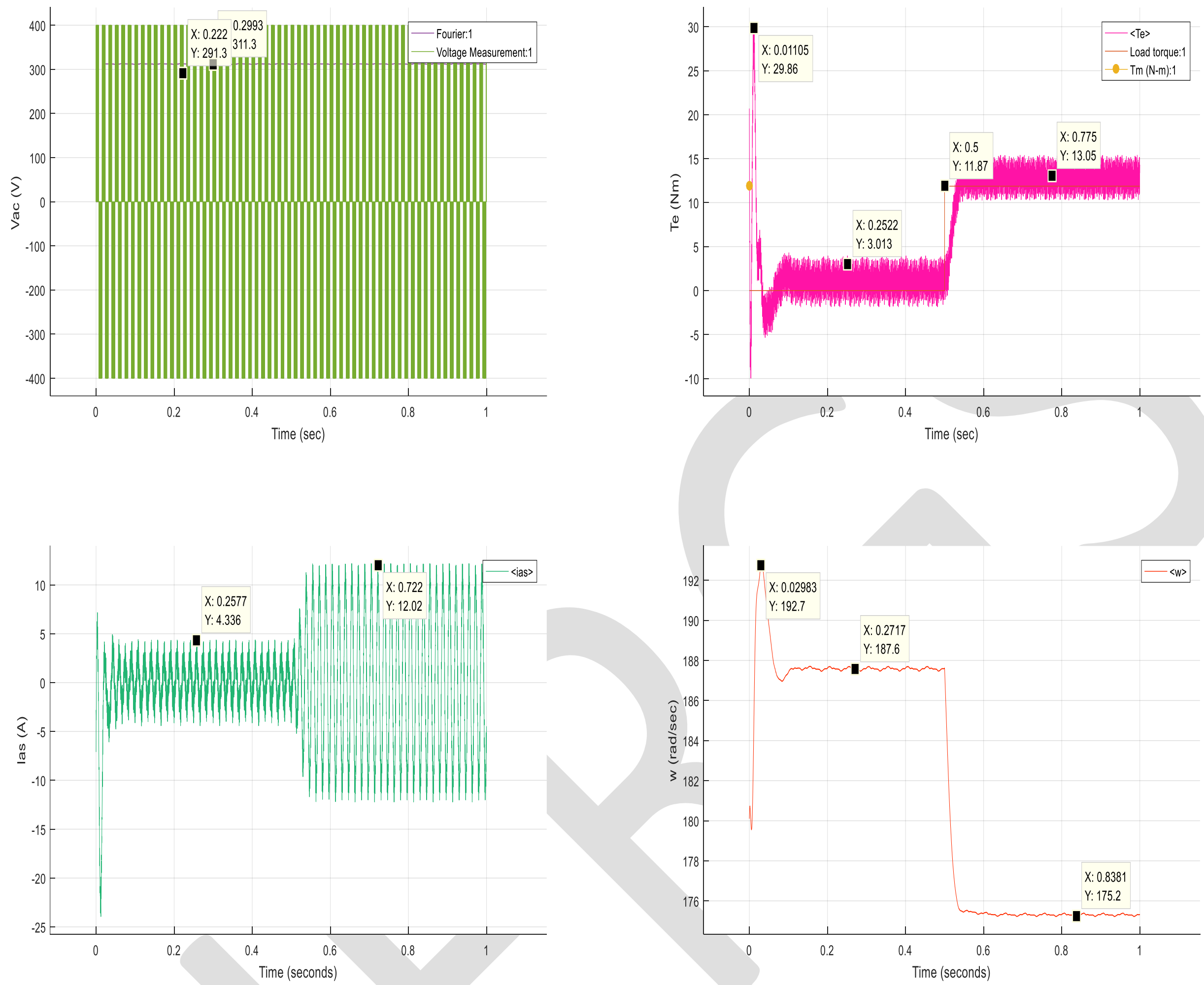

Fig. 2.9 The simulation results of three phase IM at variable load **(a)** Vab voltage **(b)** Electromagnetic Torque **(c)** Stator current Ias A **(d)** Motor Speed (rpm)

3. Harmonic Analysis

The harmonic analysis also performed to observe the harmonic content in the output voltage of inverter. Harmonics are displayed in percent of the fundamental component. The total harmonic present in the output voltage is 79.40%.The magnitude of the fundamental of the inverter voltage (312.8 V) compares well with the theoretical value 311 V for modulation index 0.90. Harmonics occur around multiples of carrier frequency (n*18 +- k). Highest harmonics (30%) appear at 16th harmonic (18 - 2) and 20th harmonic (18 + 2).

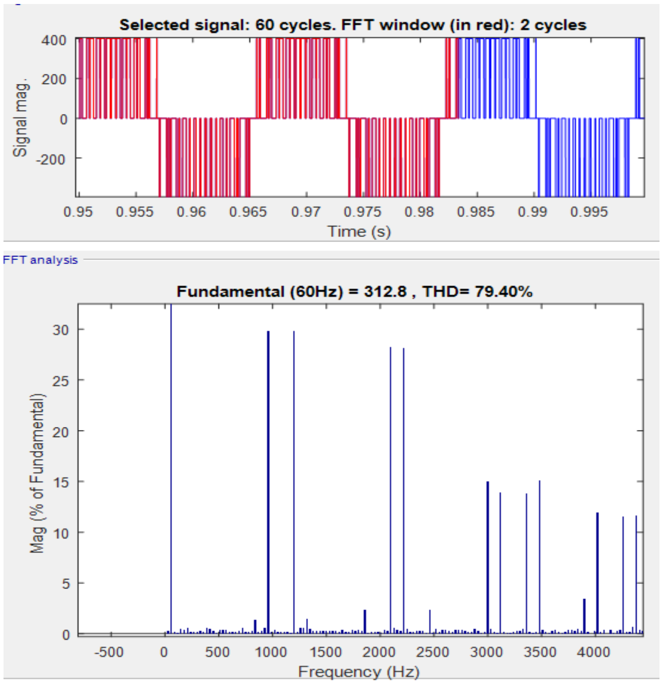

Fig.3.1 The harmonic analysis of motor line-line voltage

4. Block diagram of close loop system

The block diagrams of close loop system consist of PI controller, VSI and three phase induction motor. The measured speed is compared with reference speed and desired signal is generated which is fed to the input of voltage source inverter.

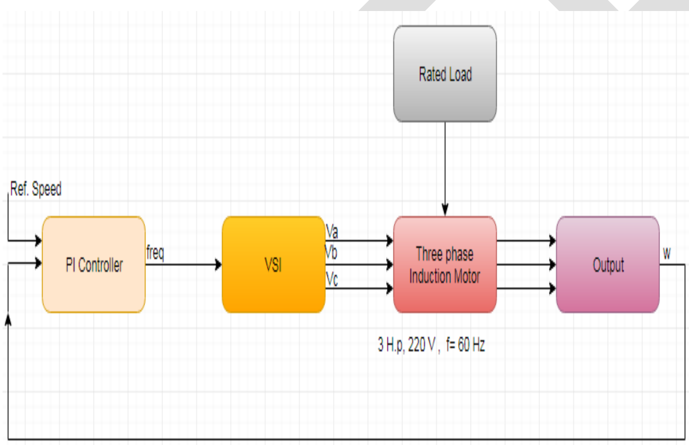

Fig 4.1 The block diagram of close loop system

4.1 MATLAB/ Simulink Model implementation of close loop

ISSN 2091-2730

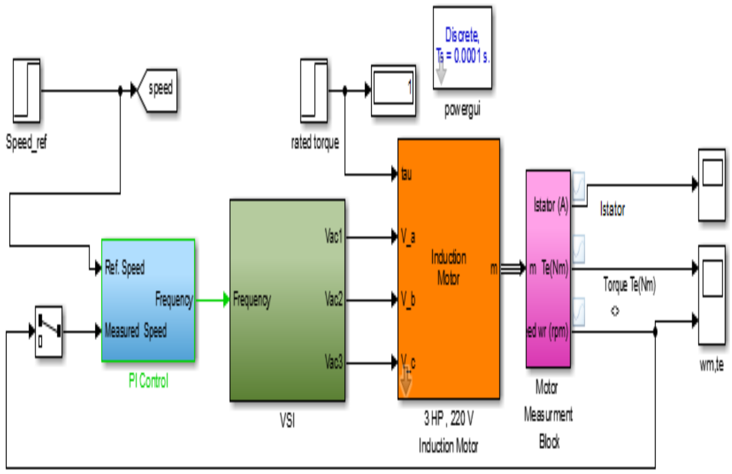

Fig. 4.2 The close loop MATLAB/Simulink model of three phase IM

4.2 Mathematical model of PI controller

The PI controller is one of the most common approaches for speed control in industrial electrical drives in general, because of its simplicity, and the clear relationship existing between its parameters and the system response specifications. It also improves the dynamic response of the system and reduces or eliminates the steady state error and the error sensibility. This is achieved by providing a proportional gain (KP) for the error input term with an integral component correction (Ki)

$$u(t) = Kpe(t) + Ki\int_0^t e(\tau)\partial\tau \qquad (9)$$

Where, u (t) is the output of the PI controller and e (t) is the error signal [10, 11]

4.1.1.1 Simulation Result of close loop speed control of IM at rated load

The simulation results of three phase close loop speed control of induction motor at rated load are shown. By proper designing a close loop PI controller not help to reduce the starting or inrush current of motor but also help to efficiently follow the reference speed at rated load of 1Nm. The maximum magnitude of stator current was observed 4A peak (2.828 A RMS) at t=0.3 sec and then decrease and become constant value of 1.5 A (1.0605 A RMS) at t = 0.45 sec. Moreover the motor measured speed is compared with reference speed at rated load. It has been found that motor measure speed efficiently follow the reference speed of 1600 RPM. As expected, the magnitude of the 60 Hz voltage contained in the chopped wave stays at 311V. At starting t<5 the electromagnetic torque of motor reaches at highest value of 11 Nm and become constant 1 Nm at t = 0.5 sec. the torque speed characteristic of IM also drawn which indicate that at rated torque 1Nm the desired speed of motor is 1600 RPM.

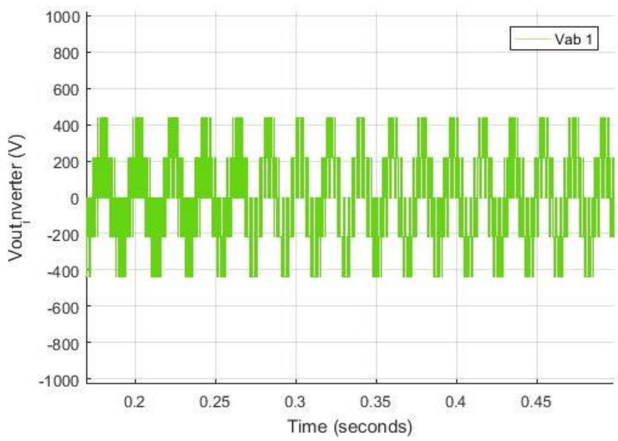

Fig. 4.3 RMS Line voltage at the output of VSI

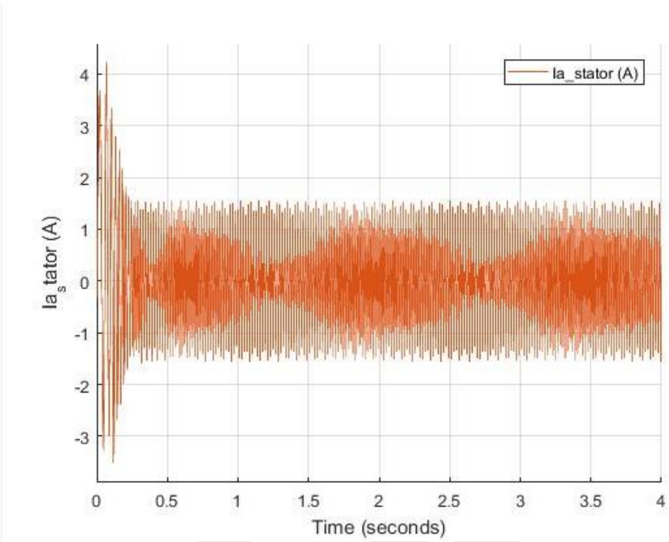

Fig. 4.4 Stator current of IM at rated load

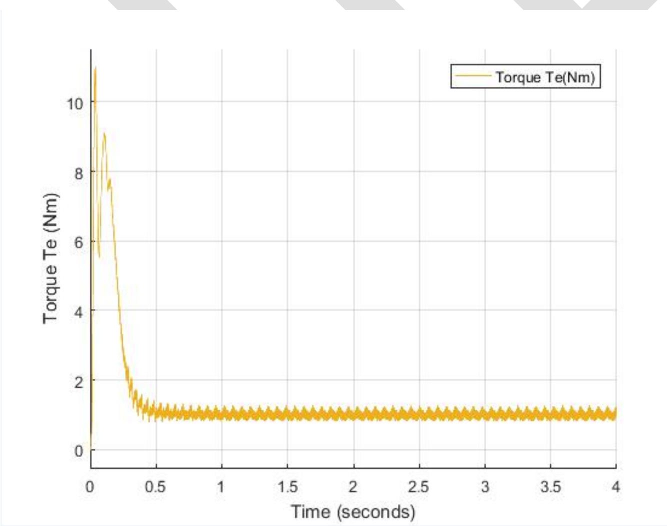

Fig 4.5 Nominal Electromagnetic torque of IM at rated speed

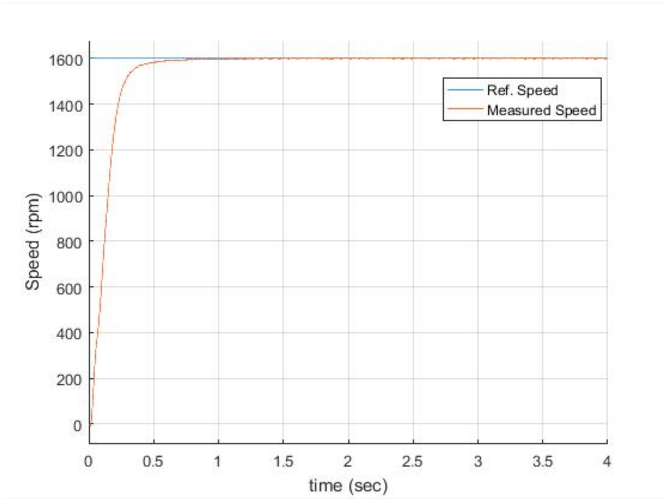

Fig 4.6 Nominal speed of IM at rated load

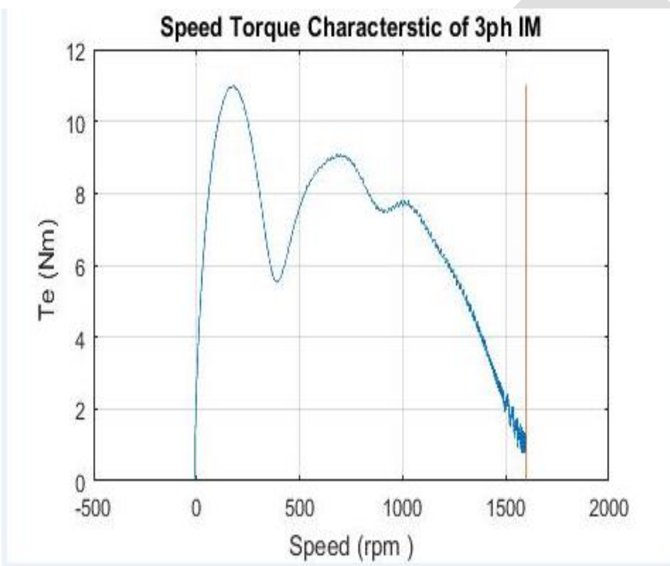

Fig. 4.7 Torque Speed characteristic of IM at rated load of 1Nm

5. Conclusion

The speed control of three phase induction motor has been invested both for open and close loop. It can be concluded that by proper designing a PI speed controller not help to reduce dynamic performance of the system but also help to reduce the steady state error, the error sensibility, high performance and smooth speed response. Both open and close loop method have its own advantage and disadvantage. open loop deals with constant speed applications, many applications in the industry operate with this control technique. However The inrush current is very large for open loop system which cause a lot of voltage drop and voltage sag in a system and also may cause the shorten life of motor. Compared this starting current is very less in case of close loop PI system. The PI control technique control is a low cost method, simple and immunity to errors of feedback signals.

6. Appendix

Table 1. Parameter of IM

Stator inductance (Ls)	0.005974 H
Rotor inductance (Lr)	0.005974 H
Magnetizing (LM)	0.20 37 H
Stator Resistance (Rs)	1.115 ohm
Rotor Resistance (Rr)	1.083 ohm
Moment of inertia (J)	0.02 kg.m^^{2}
No. of pole	4
Speed (Ns)	1800 rpm
Power (P)	3746 W

REFERENCES:

[1] Nitten Goel, P.R Sharma, Suman Bala,''Performance analysis SPWM inverter fed 3phase induction motor drive using Matlab/Simulink", International Journal of Advanced Technology in Engineering and Science, ISSN: 2348-7550 vol.30, no.2, Issue No.6, June 2014.

[2] Priynka Janak, Ranvir Kuar," Speed control and THD for three phase induction motor using Matlab/ Simulink", International Journal of Engineering Science & Research Technology, ISSN:2277-9655, Vol.10, June 2014

[3]J.L. Silva Neto & Hoang Le "Fuzzy Logic Based Controller for induction Motors" IEEE 1996 pp 631-634.

[4]R. Megartsi "Speed Control of an Induction Motor using Fuzzy logic Approach" IEEE 1994 pp 1682-1687

[5]Thomas Brehm and kuldip S Rattan "Hybrid Fuzzy PID Controller" IEEE 1994 pp 1682-1687.

[6] B. K. Bose, Modern Power Electronics and AC Drives, Pearson Education, Inc., (2002).

[7] Se jin Kim, Hao Jae Lee, Sang Koon Kim and young Ahn Kwon, "ASIC design for DTC based speed control of induction motor". IEEE international Symposium on industrial Electronics (ISIE 2001), Pusan,pp 956-961 vol. 1 May 2006.

[8] V. Chitra, and R.S prabhakar,"Induction motor speed control using Fuzzy Logic Controller", International Journal of computer and Electrical Engineering, Vol. 1 May 2006.

[9]Adel Aktai and Daw ghanim, "Dynamic simulation of a3 phase induction motor using matlab simulink", 20th annual new foundation electrical and computer equation conference (NECEC 2011), IEEE

International Journal of Engineering Research and General Science Volume 6, Issue 2, March-April, 2018
ISSN 2091-2730

Discernment of Retinal Anomalies in Fundus Images for Diabetic Retinopathy

Shiny Priyadarshini J[1], Gladis D[2]
Madras Christian College[1], Presidency College[2]
shinymcc02@gmail.com

Abstract— Retinal abnormalities can lead to permanent blindness hence retinal analysis plays a critical role in diagnosis of retinal anomalies. This paper highlights a very simple and straight forward approach to identify the retinal disorders such as diabetic retinopathy. The drusen clearly shows the presence of diabetes and other retinal disorders. The results can be further extended for clinical suites.

Index Terms— Fundus image, Diabetic Retinopathy, drusen, threshold.

I. INTRODUCTION

The human eye is composed of retina being the posterior region of eyeball is a thin layer which is highly responsible for visual recognition. Any damage to retina can cause permanent blindness hence early precautionary steps are necessary. The major important parts of retina are Macula, Optic disc and blood vessels. The typical anatomy of retina is shown is Fig.1.

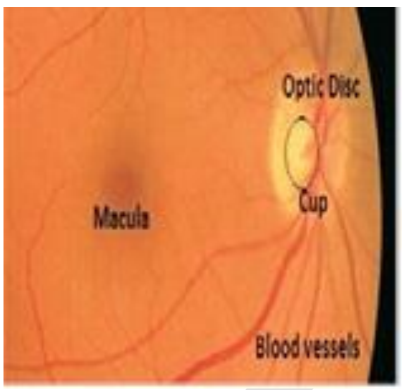

Fig.1Anatomy of retina

Retinal disorders such as Glaucoma, Cataract, Diabetic Retinopathy and AMD are the most commonly found retinal anomalies in a human eye. Such diseases require early diagnosis and immediate medical measures. The studies show that almost 75% of the people have eye correction where 64% use glasses and 11% use contact lenses. Visual impairment due to retinal disorders is a significant cause around the world. Apart from medical measures, awareness and wider knowledge regarding retinal disorders seems to be mandatory. Recent studies show that about a decade ago the risk factor for retinal diseases prevailed more for aged people than the youngsters. But now the younger generation aged 30- 40 is more prone to the retinal disorders due to their sophisticated day today lifestyle. Irreversible blindness is becoming a serious issue around worldwide [15]. A typical diseased retina commonly called as drusen is depicted in Fig.2.

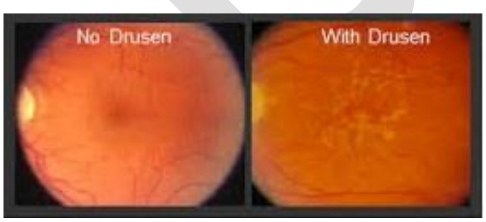

Fig.2. Normal Retina- Diseased Retina (Drusen)

The people with diabetes are at high risk for retinal disorders such as Diabetic Retinopathy (DR). DR is the most commonly found retinal disorders in human beings leading to Age-related Macular Degeneration (AMD) by gradual progression in disease. The diabetic retinopathy can be progressed into various stages such as Micro-aneurysms, hemorrhages, hard exudates and cotton wool spots [13][14]. Due to the presence of these anomalies the Macula can be disrupted for visual representation by leading to AMD or even disappearance of macula. A typical diabetic Retinopathy with degenerated macula is shown in Fig.3. This paper highlights the segmentation of retinal diseases.

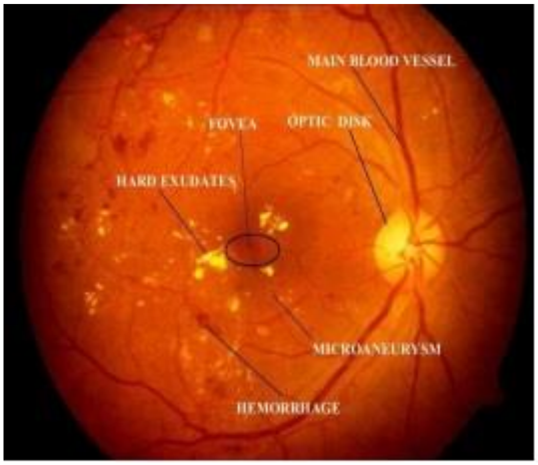

Fig.3. Diabetic Retinopathy

II. Existing Work

Niemeijer, M., et al (2008) presented localization of optic disc and fovea in retinal images. Ziyang et.al (2010) presented the automatic detection of AMD using Grading overlay techniques. Soumitra Samanta., et al (2011) presented a simple and fast algorithm using Mathematical morphology in retinal images. Priya R., et al (2013) presented the diagnosis of DR in retinal images using Wavelett transform and Fuzzy C-means segmentation. Nyni K A, et al (2014) presented Macula detection using morphological operations in retina. Charu sharma., et al (2014) presented segmentation using Fuzzy C-means and Neural Networks and diagnosed the presence of DR. Dhiravidachelvi E., et al (2015) presented the diagnosis of DR in fundus images. Raju Maher., et al (2015) automatic detection of DR using Fuzzy C- means in fundus images. Jadhav A.S., et al (2015) presented calculation of blood vessel area and identified the presence of DR in fundus images using morphological operations. Kanchan Nemade., et al (2015) presented the detection of retinal abnormalities and graded the severity of disease. Dhariti deka., et.al (2015)presented the detection of Macula and fovea using Haar wavelet transformation. Jyh haur., et al presented the history of AMD in India and its surrounding regions.

III. Proposed Methodology

This paper focuses on the segmentation of retinal diseases from a retinal image and to identify the presence of Diabetes and AMD. Although existing work shows many techniques and methodologies [3], [6],[11],[14] this articles focuses on the segmentation of DR with an unpretentious approach.

The retinal image is enhanced in the pre-processing stage by applying binarization techniques. The segmented image clearly shows the various diseases such as Micro-aneurysms, hemorrhages, hard exudates and cotton wool spots. The stages of DR extraction are shown in Fig.4.

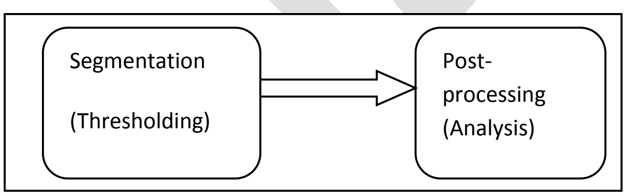

Fig.4. Steps of DR processing

IV. Retina Processing

V. Segmentation

A. Binarization

A Binary image has only two possible values, zero's and one's which are normally displayed as black and white. The retinal image is binarized where the 8 bit gray image is transformed into a 1 bit image. The image is transformed into black and white colour, where the darker regions become black and the rest of the region with white colour. The binarized image is shown in Fig 5(b)[1][2][5].

Binary image

Fig.5(a). Original images 5(b). binarized image

VI. Retina Post-Processing

The fundus image is segmented and analyzed for further studies. The segmented retinal image shows various disorders such as cotton wool spots, Micro-aneurysms, hemorrhages, hard exudates. Fig.6(a). clearly depicts the presence of cotton wool spots and Fig.6(b) shows the segmented cotton wool spots from its original image.

org Image

Fig.6(a). Fundus image with cotton wool spots

ISSN 2091-2730

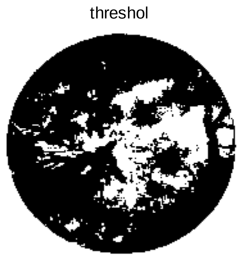

Fig.6(b). Cotton wool spots extracted after thresholding

VII. Simulation Results

Table I represents a sample of five retinal images taken from the DRIVE database, representing the abnormal human retina. About twenty five sample images were tested and the

Table I

results were satisfactory where few examples are shown in Table I.

Table I shows the original image and its binarized image with its corresponding threshold values are also shown in Table II

Image Name	Original Image	Binarized image
Disease6	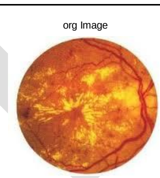	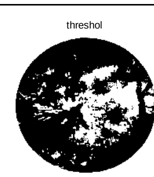
Disease5		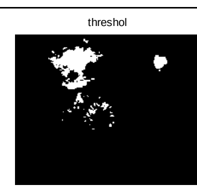

Disease4	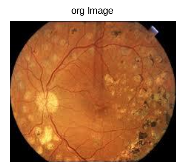	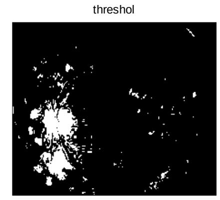
Disease3		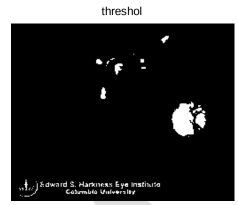
Disease7		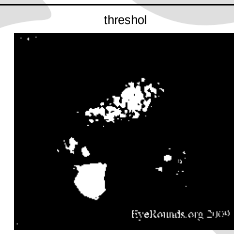

Table II

Image Name	*Threshold value*
Disease6	150
Disease5	150
Disease4	120
Disease3	150
Disease7	150

CONCLUSION

The results clearly show that the severity of DR can be diagnosed using the results obtained from the images. So it's concluded that the various retinal disorders can be identified which can be considered as the initial step. This can be further used for screening processes in eye clinics. The images can be explored further to study various abnormalities caused by DR.

REFERENCES:

[1] Niemeijer, M., Abramoff, M.D. and van Ginneken, B. „Automated localization of the optic disc and the fovea", in 30th Annual International IEEE Engineering in medicine and biology society Conference, Canada, pp. 3538-3541, 2008.
[2] Ziyang Liang et.al " Towards automatic detection of age-related macular degeneration n retinal fundus images" IEEE sep 2010
[3] Soumitra Samanta, S. Kumar Saha and Bhabatosh Chanda „A Simple and Fast Algorithm to Detect the Fovea Region in Fundus Retinal Image", Second International Conference on Emerging Applications of Information Technology, IEEE pp. 206-209, 2011.
[4] SujithKumar SB., Vipula Singh., "Automatic detection of Diabetic Retinopathy in Non-dilated RGB Retinal Fundus Images"., Vol 47, June 2012.
[5] Damon W.K. Wong et.al" Automatic Detection of the Macula in Retinal Fundus Images using Seeded Mode Tracking Approach" IEEE 2012
[6] Priya R., Aruna P., "Diagnosis of Diabetic Retinopathy Using Machine Learning Techniques" Vol 3, ISSN: 2229-6956, July 2013.

[7] Nyni K A, Drisya M K, Neethu Rose Thomas., Detection of Macula in Retinal Images using Morphology", Vol 4, ISSN: 2277 128X, Jan 2014.
[8] Madhura J P., Kakatkar M N., " Review of Methods for Diabetic Retinopathy Detection and Severity Classification" IJRET, Vol 3, ISSN: 2321 7308, March 2014.
[9] Charu sharma, Geeta Kaushik, "Automatic Diagnosis of Diabetic Retinopathy Using Fundus Images, Vol 4, ISSN: 2277 128X, May 2014.
[10] Dhiravidachelvi E., Rajamani V., "A Novel Approach for Diagnosing Diabetic Retinopathy in Fundus Images" Journal of Computer Science 2015.
[11] Raju Maher, S Kayte, Mukta ,"Review of Automated Detection for Diabetes Retinopathy Using Fundus Images, Vol 5, ISSN: 2277 128x, March 2015.
[12] Jadhav A.S, Pushpa B.Patil, "Classification of Diabetes Retina Images using Blood Vessel Area" Vol 4 (IJCI) April 2015.
[13] Kanchan Nemade., Bhagat K.S., "Microaneurysyms Detection from Retinal Image and Diabetic Retinopathy Grading" Vol 4, ISSN:2278-6856, Aug 2015.
[14] Dhariti deka et.al " Detection of Macula and Fovea for disease Analysis in color fundus images" IEEE 2015
[15] Jyh haur" Epidemiology of age related macula degeneration in the indian subcontinent" 2009 .

International Journal of Engineering Research and General Science Volume 6, Issue 2, March-April, 2018
ISSN 2091-2730

A Training Based Approach for Vehicle Plate Recognition (VPR)

Laveena Agarwal[1], Vinish Kumar[2], Dwaipayan Dey [3]

[1]Department of Computer Science & Engineering

, Sanskar College of Engineering &Technology, Ghaziabad, India

[2]Department of Computer Science & Engineering

,Sanskar College of Engineering &Technology, Ghaziabad, India

[3]Department of Electronics & Communication Engineering

Bhagwant Institute of Technology, Ghaziabad, India

E-mail: robin.dey00@gmail.com

Abstract- From last few years, vehicle plate recognition (VPR) has become a vital technology of security and traffic applications. In this paper we present a training based approach for the recognition of vehicle number plate. The whole process has been divided into three stages i.e. capturing the image, plate localization and recognition of digits over the plate. HOG features have been used for the training purpose and Support Vector Machine (SVM) is employed for the classification purpose yielding in more than 99% accuracy while recognition. The algorithm has been tested over more than 100 images.

Keywords: Vehicle Plate Recognition (VPR), Support Vector Machine (SVM), Histogram of Gradient (HOG),Optical Character Recognition (OCR), Licence Plate Recognition (LPR)

I. INTRODUCTION

Now a days Vehicle plate recognition (VPR) has become a vital technology for security and traffic applications that have a wide range from traffic surveillance to parking lot access control to information management for monitoring purposes [1].[9],[10]. We can say, VPR helps to ascertain vehicles and provides a reference for further vehicle tracking and activity analysis [1], [12]-[16].

Automatic vehicle plate recognition (VPR) plays a significant role in huge applications such as parking fee payment, electronic toll payment, restricted area security, traffic surveillance [8]. In the detection of number plates, plate variations & environment variations occur because VPR technology operate under dissimilar environmental conditions such as circumscribed vehicle speed, fixed resolution, prescribed routes, specify range, rigid illumination [1]-[4], [8]. VPR technology discerns a vehicle's number plate number from captured image by camera. It includes object detection, pattern recognition and data image processing.

In order to verify the practicability of the VPR system it implemented over DSP i.e. TMS320C30 using Hough Transform for the detection of vehicle license plates [11][12][18].

Earlier the VPR systems were used as part of the surveillance systems. In [8] system was used as a part of intersection surveillance video camera system for traffic analysis.

Fig2: Character Segmentation

This paper is organized as following: Section I describes the steps involved for the vehicle plate recognition, Section II describes the proposed algorithm for the recognition, and section III contains the experimental results and discussions and finally the section IV sum up the paper with conclusion.

SECTION-I

Number plate recognition basically consists of three concrete steps. These are as follows:

1. Number Plate Extraction.

2. Character Segmentation.

3. Template Matching.

1. Number Plate Extraction

In this stage the input is an image of a vehicle, and a part of the image is output which contains the potential Number plate. The Number plate can lie anywhere in the image. To decrease the processing time, the Number plate can be distinguished by its features rather than processing each pixel in the image and therefore only those features pixels are processes by the system. Plate region is found out by passing a rectangular image over the previous.Fig.1 shows the extraction of plate.

Fig1: Extracted Plate Region

2. Character Segmentation

After number plate extraction character segmentation is occurred. Characters are segmented from the number plate image which is then used for template matching.Fig.2 shows the character segmentation of captured image.

3. Template Matching

Segmented characters are template matched with the templates of each character and the number plate is identified as a string.Fig.3&Fig.4 shows the output of string form and output after template matching respectively.

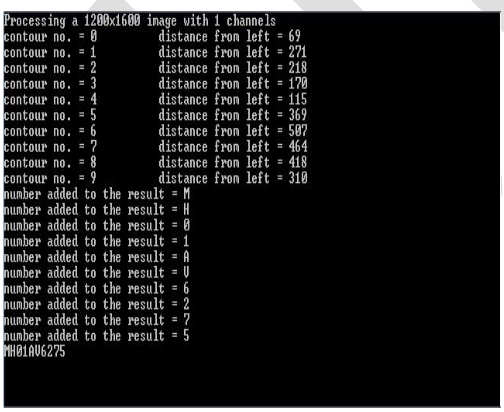

Fig.3: output after string form

Fig.4: output after Template Matching

SECTION-II

A) PROPOSED SYSTEM

i) Image Capture and Resizing

The first phase of the process is to capture the images of the moving vehicles for which number plate is to be recognized [1],[18]-[22]. The captured image is then normalized to a standard size. After that image is converted to grayscale image. Then localize the number plate from the captured image. Further processes are done on the localized number plate.

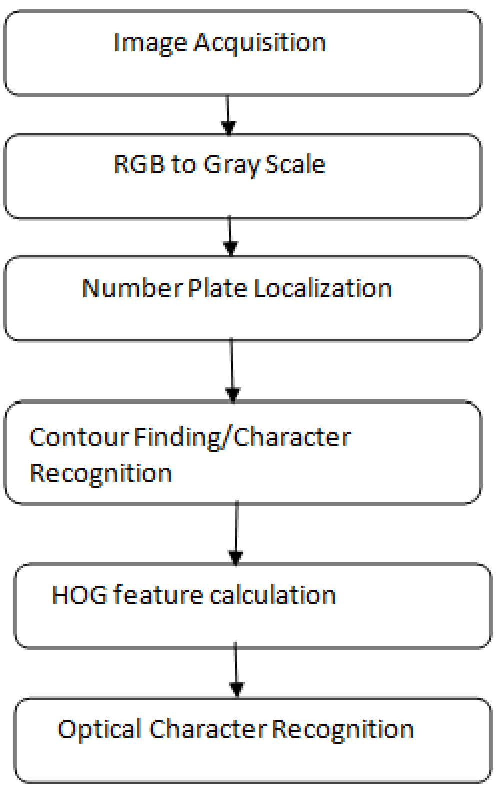

Fig. 5 Block Diagram for the Proposed Algorithm

B) TRAINING

Image sets of 26 alphabets and 10 numbers of different sizes and shapes are created. All these binary images are then used for the training phase. During training, the Histogram of Gradient (HOG) features are calculated for all the images. Every image is also given a unique label which will be useful while classifying the alphanumeric character in the test image. The classification process is done using Support Vector Machine (SVM) classifier.

C) TESTING

Proper image pre-processing techniques like converting to grayscale and adaptivehistogram equalization are done to get a binary version of the test image. Connected component analysis is done on the binary image and filtered using height and width to get the alpha numeric characters in the image. Then HOG features are found for each character and it is classified using the SVM classifier to check if it belongs to the dataset we used while training. Once it passes the check, the image is cropped along the Y axis to get only the region where the number plate is present.

After converting the cropped image to binary, horizontal histogram is calculated. This histogram gives information about the plate location in the cropped image. After locating the plate in the image, again thresholding, histogram equalization is done on this image (which contains only the number plate), and subsequently connected component analysis is done and the characters are filtered using height and width. Then each valid character is then identified using Optical Character Recognition (OCR) and the final vehicle plate characters are shown as the output.

SECTION-III

A) EXPERIMENTAL RESULTS

Fig. 6 shows the captured image from the moving vehicle to perform the experiment upon.

Fig 6. Image Acquisition

Fig7. Pre-Processed Image after Plate Localization

Fig. 7 depicts the pre-processed image of the number plate after its localization i.e. extraction of number plate from the input image.

Fig8. Image filtered using Height and Width

In fig. 8 the localized number plate image has been filtered using height after applying histogram equalization on the binary image.

Fig. 9 Image Cropped along Y axis

The image is cropped along Y-axis in fig. 9 for the enlarged view of the characters.

Fig 10.Cropped Number Plate

The number plate is then cropped from the whole image to get a clear image of the characters from the whole number plate.

Fig.11 Processed Cropped Image

The cropped image is then processed further as shown in fig. 11 i.e. filtered using height and width.

Fig12. OCR Output of the Characters

.

The outputs are shown in fig. 8 after complete process.

To measure the accuracy of the algorithm, it was tested over different images and models of the cars in different lighting conditions. The plate localization accuracy was found to be almost 100%, while the number plate recognition accuracy achieved was 99%.

Table 1: Accuracy Comparison Results

Methods	Plate Localization %	Character Recognition %
Hitesh Rajput [1]	97.6	96.4
M.-L. Wang and colleagues. [5]	99	98
K. Deb and colleagues[6]	92.4	-
Y.C. Chiou. [3]	96.2	-
Proposed Method	99.8	99

Table 1 shows the comparison between the proposed method and some recent approaches to vehicle number plate localization techniques. The results are measured in terms of accuracy.

SECTION-IV

A) CONCLUSION

A training based approach has been discussed in the paper for the vehicle plate recognition. The results of the proposed algorithm signify the superiority of the proposed algorithm over some common vehicle plate recognition approaches. For the extended work this can be taken to blurred and distorted number plates and try to recognize the plates clearly in some real bad weather conditions where input images are skewed.

REFERENCES:

[1]Hitesh Rajput et al., "An Automated Vehicle License Plate Recognition System," 0018- 9 162 / 15/$31 .00 © 2015 I E EE.

[2] G. Liu, Z. Ma, Z. Du, and C. Wen, "The calculation method of road travel time based on number plate recognition technology," in *Proc. Adv.Inform. Tech. Educ. Commun. Comput. Inform. Sci.*, vol. 201. 2011, pp.385–389.

[3]Y.-C. Chiou, L. W. Lan, C.-M. Tseng, and C.-C. Fan, "Optimal locations of number plate recognition to enhance the origin-destination matrix estimation," in *Proc. Eastern Asia Soc. Transp. Stu.*, vol. 8. 2011, pp. 1–14.

[4]S. Kranthi, K. Pranathi, and A. Srisaila, "Automatic number plate recognition," *Int. J. Adv. Tech.*, vol. 2, no. 3, pp. 408–422, 2011

[5] M.-L. Wang et al., "A Vehicle License Plate Recognition System Based on Spatial/Frequency Domain Filtering and Neural Networks," Proc. 2nd Int'l Conf. Computational Collective Intelligence: Technologies and Applications (ICCI 10), LNCS 6423, Springer, 2010, pp. 63–70.

[6] K. Deb, H.-U. Chae, and K.-H. Jo, "Vehicle License Plate Detection Method Based on Sliding Concentric Windows and Histogram," J. Computing, vol. 4, no. 8, 2009, pp. 771–777.

[7] C.N.E. Anagnostopoulos et al., "A License Plate-Recognition Algorithm for Intelligent Transportation System Applications," IEEE Trans. Intelligent Transportation Systems, vol. 7, no. 3, 2006, pp. 377–392.

[8] C.A. Rahman, W. Badawy, and A. Radmanesh, "A Real-Time Vehicle's License Plate Recognition System," Proc. IEEE Conf. Advanced Video andSignal Based Surveillance (IVSS 03), 2003, pp. 163–166.

[9] S. Wang and H. Lee, "Detection and recognition of number plate characters with different appearances," in *Proc. Int. Conf. Intell. Transp.Syst.*, vol. 2. 2003, pp. 979–984.

[10] M. M. I. Chacon and S. A. Zimmerman, "License plate location based on a dynamic PCNN scheme," in *Proc. Int. Joint Conf. Neural Netw.*, vol. 2. 2003, pp. 1195–1200

[11] L. Xiaojing, Research on Automatic Recognition of Car License Plate, Journal of Nanjing University of Aeronautics andAstronautics 30 (5), 573-576, 1998.

[12]Cho. D.U. and Cho. Y. H., "Implementation of preprocessing independent of environment and recognition of car number plate using histogram and template matching". The Journal of the Korean Institute of Communication Sciences, 23(1):94-100, 1998.

[13] Christoph Busch, Ralf Doner, Christian Freytag and Heike Ziegler, "Feature based Recognition of Traffic Video Streams for online Route Tracing", VTC'98. IEEE International Symposium on, 1998, pp.: 1790 –1794.

[14]Cui. Y. and Huang. Q, "Automatic license extraction from moving vehicles". International Conference on Image Processing(ICIP97), 3:126–129, 1997.

[15]Draghici, Sorin. "A neural network based artificial vision system for licence plate recognition",1997.

[16] Draghici. S, "A Neural Network based Artificial Vision System for License Plate Recognition", Int.J.Neural Syst., Vol.8 No.1 Feb.1997, pp.113-126.

[17]H. J. Kang and J. Kim, "Probabilistic framework for combining multiple classifier at abstract level," in *Proc. Int. Conf. DocumentAnal. Recognit.*, vol. 1. 1997, pp. 870–874.

[18] V. Kamat and S. Ganesan, "An Efficient Implementation of the Hough Transform for Detecting Vehicle License Plates Using DSP's, Cellular Neural Networks and Their Applications," Proc. IEEE Int'l Carnahan Conf., 1997, pp. 209–218.

[19] M. N. Granieri, F. Stabile, and P. Comelli, Recognition of Motor Vehicle License Plates in Rear-view Images, In: Jorge L. C. Sanz (Ed.), Image Technology, Advances in ImageProcessing, Multimedia and Machine Vision, Springer-Verlag, Berlin, pp. 231-252, 1996.

[20] V. Kamat and S. Ganesan, "An efficient implementation of the Hough transform for detecting vehicle license plates using DSPs," in Proc Real-Time Tech. Applicat. Symp., 1995, pp. 58–59.

[21]Comelli.P, Ferragina.P, Granieri. M.N., and Stabile. F, "Optical recognition of motor vehicle license plates", IEEE Trans. Veh. Technol., Vol.44, No.4 1995, pp.790-799 .

[22] K. Miyamoto, K. Nagano, M. Tamagawa, I. Fujita, and M. Yamamoto, "Vehicle number-plate recognition by image analysis," in *Proc. Int.Conf. Ind. Electron. Control Instrum.*, vol. 3. 1991, pp. 1734–1738.

Valuation of groundwater protection: A state level analysis in India

Arnab Roy

Ph.D. Scholar, Department of Agricultural Economics, University of Agricultural Sciences, GKVK, Bengaluru

E-mail: royarnab_94@rediffmail.com

Abstract: The benefits of groundwater protection are estimated to assess the non-marketed benefits associated with increased protection of the groundwater resource, as compared to purification of groundwater for drinking water purposes. As of April 2015, the water resource potential or annual water availability of the country in terms of natural runoff (flow) in rivers is about 1,869 Billion Cubic Meter (BCM)/year. However, the usable water resources of the country have been estimated as 1,123 BCM/year. According to some estimates, it accounts for nearly 80 per cent of the rural domestic water needs, and 50 per cent of the urban water needs in India. Therefore, the evaluation of ground water quality and impact of polluted groundwater on environment and health has drawn attention of the researchers. The present paper is also an attempt on such study. The pollution level of ground water in India and its effect on environment and vicinity area have been studied in the present paper.

Key Words: non-marketed, natural runoff, hedonic pricing, contingent valuation,

Introduction

The crucial role groundwater plays as a decentralized source of drinking water for millions rural and urban families cannot be overstated. According to some estimates, it accounts for nearly 80 per cent of the rural domestic water needs, and 50 per cent of the urban water needs in India. Groundwater is generally less susceptible to contamination and pollution when compared to surface water bodies. Increase in overall salinity of the ground water and/or presence of high concentrations of fluoride, nitrate, iron, arsenic, total hardness and few toxic metal ions have been noticed in large areas in several states of India. Ground water contains wide varieties of dissolved inorganic chemical constituents in various concentrations as a result of chemical and biochemical interactions between water and the geological materials through which it flows and to a lesser extent because of contribution from the atmosphere and surface water bodies. Ground water in shallow aquifers is generally suitable for use for different purposes and is mainly of Calcium bicarbonate and mixed type. However, other types of water are also available including Sodium-Chloride water. The quality in deeper aquifers also varies from place to place is generally found suitable for common uses. . The purpose of this paper is to describe problems and possibilities with economic valuation of risk reductions, and to illustrate how different valuation perspectives affect the extent of investigations. An economic decision analysis model is presented for integrating the valuation of health, ecological, and other risks into one assessment. The decision model can be used on the societal level for cost-benefit analysis, but also for evaluating the cost-efficiency of different investigation and remediation alternatives.

Extent and Impacts of Groundwater Contamination and Pollution

The incidence of fluoride above permissible levels of 1.5ppm occur in 14 Indian states, namely, Andhra Pradesh, Bihar, Gujarat, Haryana, Karnataka, Kerala, Madhya Pradesh, Maharashtra, Orissa, Punjab, Rajasthan, Tamil Nadu, Uttar Pradesh and West Bengal affecting a total of 69 districts, according to some estimates.Some other estimates find that 65 per cent of India's villages are exposed to fluoride risk

ISSN 2091-2730

Table 1: State-wise Status of Groundwater Resources (2010)

No	State	Billion Cubic Metres (BCM) Annual Replenishable Groundwater Resource	Net Availability	Net Draft	Stage of GW Development (Net Draft/Net Availability*100)
1	Andhra Pradesh	36.50	32.95	14.90	45
2	Assam	27.23	24.89	5.44	22
3	Bihar	29.19	27.42	10.77	39
4	Chhattisgarh	14.93	13.68	2.80	20
5	Gujarat	15.81	15.02	11.49	76
6	Haryana	9.31	8.63	9.45	109
7	Jammu and Kashmir	2.70	2.43	0.33	14
8	Jharkhand	5.68	5.25	1.09	21
9	Karnataka	15.93	15.30	10.71	70
10	Kerala	6.84	6.23	2.92	47
11	Madhya Pradesh	37.19	35.33	17.12	48
12	Maharashtra	32.96	31.21	15.09	48
13	Orissa	23.09	21.01	3.85	18
14	Punjab	23.78	21.44	31.16	145
15	Rajasthan	11.56	10.38	12.99	125
16	Tamil Nadu	23.07	20.76	17.65	85
17	Uttar Pradesh	76.35	70.18	48.78	70
18	Uttarakhand	2.27	2.10	1.39	66
19	West Bengal	30.36	27.46	11.65	42
20	Other states	7.67	7.03	0.86	12
Total		432.42	398.70	230.44	58

Source: CGWB (2006).

High levels of salinity are reported from all these states except West Bengal and also the NCT of Delhi, and affects 73 districts and three blocks of Delhi. Iron content above permissible level of 0.3 ppm is found in 23 districts from 4 states, namely, Bihar, Rajasthan, Tripura and West Bengal and coastal Orissa and parts of Agartala valley in Tripura. High levels of arsenic above the permissible levels of 50 parts per billion (ppb) are found in the alluvial plains of Ganges covering six districts of West Bengal.

Presence of heavy metals in groundwater is found in 40 districts from 13 states, viz., Andhra Pradesh, Assam, Bihar, Haryana, Himachal Pradesh, Karnataka, Madhya Pradesh, Orissa, Punjab, Rajasthan, Tamil Nadu, Uttar Pradesh, West Bengal, and five blocks of Delhi. Ground water development is a ratio of the annual ground water extraction to the net annual ground water availability. It indicates the quantity of ground water available for use.

Table 2: Comparative status of level of ground water development in India in the past 20 years

Level of ground water development	Explanation	% of districts in 1995	% of districts in 2004	% of districts in 2009	% of districts in 2011
0-70% (Safe)	Areas which have ground water potential for development	92	73	72	71
70-90% (Semi-critical)	Areas where cautious ground water development is recommended	4	9	10	10
90-100% (Critical)	Areas which need intensive monitoring and evaluation for ground water development	1	4	4	4
>100% (Over-exploited)	Areas where future ground water development is linked with water conservation measures	3	14	14	15

Sources: Central Ground Water Board; PRS.

Of all these sources, ground water constitutes the largest share. Wells, including dug wells, shallow tube-wells and deep tube wells provide about 61.6% of water for irrigation, followed by canals with 24.5%. Over the years, there has been a decrease in surface water use and a continuous increase in ground water utilization for irrigation.

Figure : Increase in ground water utilization for irrigation

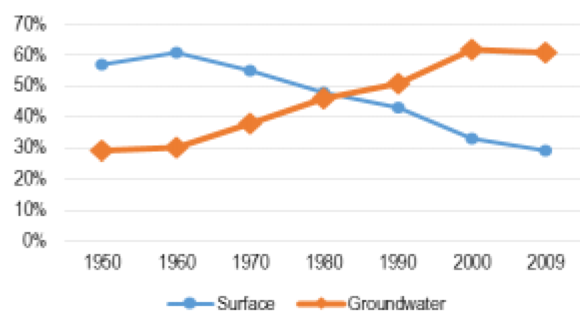

The dependence of irrigation on ground water increased with the onset of the Green Revolution, which depended on intensive use of inputs such as water and fertilizers to boost farm production. Incentives such as credit for irrigation equipment and subsidies for electricity supply have further worsened the situation.

It has been pointed out that nearly 60% of all districts in the country have issues related to either availability of ground water, or quality of ground water, or both.

Table 3: States and districts affected by geogenic contamination in groundwater

Geogenic contaminants	Number of affected states	Number of affected districts
Arsenic	10	68
Fluoride	20	276
Nitrate	21	387
Iron	24	297

Source: Central Ground Water Board; PRS.

Issues in Tackling Groundwater Contamination and Pollution

The first step towards evolving measures to prevent and cure groundwater quality deterioration is generating reliable and accurate information through water quality monitoring (WQM) to understand the actual source/cause, type and level of contamination. However, there are a few observation stations in the country that cover all the essential parameters for water quality and hence the data obtained are not decisive on the water quality status. Secondly, WQM involve expensive and sophisticated equipments that are difficult to operate and maintain and require substantial expertise in collecting, analyzing and managing data. Since water technology is still not advanced in India, it is very likely that the available data is less reliable. The existing methodology for WQM is inadequate to identify the various sources of pollution. Integration of data on water quality with data on water supplies, which is very important from the point of view of assessing water availability for meeting various social, economic and environmental objectives, is hardly done. And finally, in the absence of any stringent norms on water quality testing, results can change across agencies depending on sampling procedure, time of testing, and testing instruments and procedure.

Economic Valuation of Ground Water

Since the 1960s economists have developed a variety of techniques for assessing the value of nonmarket goods and services, not priced and traded in markets. While most applications are to natural resources and environmental assets, the concepts and methods of nonmarket valuation extend to a range ofgoods not usually traded in markets. The ability to assign values to such goods and services has improved the accuracy of benefit-cost analysis. Inclusion of economic values for some important (and previously ignored) classes of environmental services enables benefit-cost assessments to reflect more fully the consequences of natural resource policies and regulations. The first application of techniques developed specifically for valuing nonmarketed commodities involved the travel cost method (TCM), Hotelling proposed in 1946 as a means of valuing visits to national parks. The travel cost method, in its numerous variants, has been used extensively to assess the value of a commodity used directly by the consumer, namely outdoor recreation. Refinements of the travel cost method and the development of new techniques, such as the contingent valuation method (CVM) and hedonic price method (HPM)In the Contingent Valuation (CV) survey, the respondents are provided with this information directly, and they are asked to choose how much they would pay for groundwater protection. In the Choice Experiment (CE) survey the respondents are asked to choose between alternatives where the levels of drinking water quality, surface water quality and price are varied systematically.

In the contingent valuation literature, Ordinary Least Squares (OLS) regressions are commonly used to estimate a WTP model from responses to an open-ended question. However, if the sample is censored it is not appropriate to use OLS. A censored value can be defined as follows. Let y^* be a normally distributed variable with mean μ and variance σ 2 . An observed variable is censored below if:

$$y = c \text{ if } y^* < c \text{ and } y = y^*$$

otherwise.where c is a given constant. This is illustrated in the following figure:

Figure: Normal Variable y* and Censored variable y

International Journal of Engineering Research and General Science Volume 6, Issue 2, March-April, 2018
ISSN 2091-2730

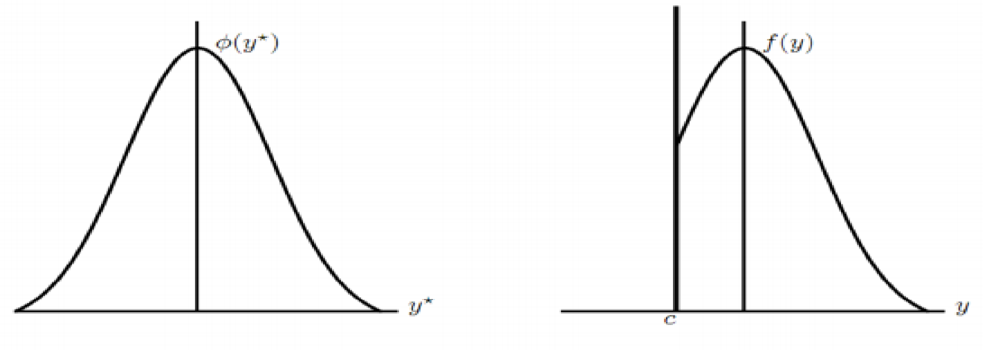

During the fieldwork, various zones in the city reported that tap water services were interrupted for at least two weeks before the interview. Given that a number of WTP observations have a zero value (protests for the unreliable water supply), the sample is censored. Therefore, the proper model for assessing the WTP is a Tobit model.

In the CE survey, the indicator levels are designed so as to approach the descript.

Table 1. WTP-results from CE and CV.

	CE	**CV**
Naturally clean groundwater	1853	698
Very good conditions for plant and animal life	1120	
Total	2973	

Groundwater governance framework

The main findings related to groundwater governance are:

Even though the 1998 National Water Policy (NWP) and the 2002 amended version do not have statutory status, and thus cannot be legally enforced, they are the outcome of intensive political discussions and so state governments could find them useful in developing their own water policies. Agriculture, energy, water supply, and many other sectoral policies influence groundwater use and pollution, but they are difficult to reform. It is clear that groundwater management falls under the jurisdiction of the states and to this effect the central government has circulated since 1970 a model groundwater bill. Regretfully, only a few states have formally adopted it. Nevertheless, the two main legal drawbacks (the resource being assumed to follow the right to land and the absence of groundwater legislation at the central level) have been sorted out by: The Supreme Court and High Court rulings have affirmed the government's right and obligation to protect groundwater under the right to life guaranteed by the Constitution.

Legislative and Policy Framework

This implies that state legislative assemblies can make laws on the subject. In order to provide broad guidelines to state governments to frame their own laws relating to sustainable water usage, the central government has published certain framework laws or model Bills. In 2011, the government published a Model Bill for Ground Water Management based on which states could choose to enact their laws. As recommended in this policy, the government published a National Water Framework Bill in 2013. The Model Bills and National Water Policy address the governance of ground water under the public trust doctrine.

Institutional Framework

Within the central government, the Ministry of Water Resources, River Development and Ganga Rejuvenation is responsible for the conservation and management of water in the country. The Ministry of Rural Development also implements certain programmes related to ground water management. In addition, the Ministry of Environment, Forests and Climate Change is partially responsible for the prevention and control of pollution, including water pollution, and ground water contamination. In addition, there are four major central institutions that address issues related to ground water.

Conclusions

The main conclusions of this study are: Large variation of acceptable risk levels in different sectors of society has been noted. The acceptable risk levels for contaminated sites are low compared to other types of risks, e.g. health risks to workers or residential health risks. The present Indian approach of comparing measured contaminant concentrations to guideline values, rather than quantification of the actual risk level, does not correspond very well to economic valuation of risk reduction. Risk should preferably be defined as a measure of lack of knowledge and its consequence, instead of as a frequency determined in a deterministic way. A comprehensive World Bank study concluded that high-level policy reform in the shape of regulatory measures, economic instruments, or tradable groundwater extraction rights is simply not a credible way forward. Taking quantitative and qualitative aspects together, it would appear that a total of 347 districts (59% of all districts in India) are vulnerable in terms of safe drinking water in India. This is a matter of serious concern, requiring a new approach.

REFERENCES:

1. World Bank .(2010). Deep Wells and Prudence: Towards Pragmatic Action for Addressing Groundwater Overexploitation in India, World Bank.
2. Schultz S D and Lindsay B E, (1990).The willingness to pay for groundwater protection. Water Resources Research, 26 (9), 1869-1875.
3. Freeze, R.A., Bruce, J., Massman, J., Sperling, T. and Smith, L., (1992). Hydrogeological Decision Analysis: 4. The Concept of Data Worth and Its Use in the Development of Site Investigation Strategies. Ground Water, 30(4): 574-588.
4. Massmann, J., Freeze, R. A., Smith, L., Sperling, T. and James, B., (1991). Hydrogeological Decision Analysis: 2.Applications to Ground-Water Contamination. Ground Water. 29(4): 536-548.
5. GoI (2010), Groundwater Scenario of India 2009–10, Central Ground Water Board, Ministry of Water Resources:http://www.cgwb.gov.in/documents/Ground Water Year Book%2 02009-10.pdf.
6. GoNCTD (Government of NCT of Delhi) (2010), State of Environment Report for Delhi 2010, Department of Environment and Forests.
7. Roopal Suhag,.(2016). Overview of Ground Water in India. Prsindia.1:1-11
8. Singh, K. P.; Parwana, H. K. 1998. Groundwater pollution due to industrial wastewater in Punjab state and strategies for its control. Indian Journal of Environmental Protection 19(4): 241-244. Bouwer, H. 2000. Integrated water management: emerging issues and challenges. Agricultural Water Management 45: 217-228.
9. Bradford, A.; Brook, R.; Hunshal, C. S. 2003. Wastewater Irrigation in Hubli-Dharwad, India: Implications for health and livelihoods. Environment and Urbanisation 5(2): 157-170.

Mid-Sagittal Plain Detection and Correction Based Wavelet Transfrom and Principle Component Analysis

Ali M. Hasan
Al-Nahrain University- College of Medicine- Baghdad, Iraq
a.hasan4@edu.salford.ac.uk

Abstract— The Mid-Sagittal Plain (MSP) of Brain is an important initial step in brain image analysis because of providing an initial estimation for the brain, pathology assessment and tumor detection. The human brain is divided into two hemispheres and these hemispheres are approximately bilateral symmetry around the MSP, that's mean that most of structures in one side of the brain have a counterpart on the other side with similar shape and location. This paper presents a technique for detecting and correcting the MSP of brain from magnetic resonance images (MRI) by using Principle component analysis (PCA) method that computes the distinctive principle axes that are orthogonal to each other, and determine the orientation of the patient's head instead of depending on measuring symmetry to identify the MSP of brain.

Keywords-component; Magnetic resonance image (MRI); Principle compnent analysis (PCA); Mid-Sagittal Plain (MSP)

I. Introduction

The advances in medical imaging techniques provide facilities of internal visualization of brain. These medical images are used for diagnosing and visual interpretation by clinicians. The MSP identification is an important initial step in brain image analysis because of providing an initial estimation for the brain, pathology assessment and tumor detection [1, 2]. The human brain is divided into two hemispheres and these hemispheres are approximately bilateral symmetry around the MSP, that's mean that most of structures in one side of the brain have a counterpart on the other side with similar shape and location. The two hemispheres are separated by the longitudinal fissure that represents a membrane between the left and right hemispheres filled with CSF and it can be used to recognize the two hemispheres visually [3]. The two hemispheres separation process in the axial MRI brain scanning images can be done by recognizing the MSP along the longitudinal fissure which can be used as a reference for asymmetry analysis. The MSP of the brain has the same orientation of the patient's head. The symmetry of brain is an important indicator about the normality and abnormality of brain such that most pathology such as tumors, bleeding and stroke in the human brain can be determined by a symmetry based analysis of MRI brain scanning images. However, the growth of tumor cells can destroy the symmetry and curve the MSP of brain [4]. The MSP extraction methods can be divided into two groups [3, 5]; Content-based method is based on seeking a plane that maximizes a symmetry measure between both sides of brain [3, 5-9]. The major obstacle preventing this methods from wide adoption in realistic neuro-application is the difficulty of measuring symmetry and identifying the MSP of the brain for the pathological patients e.g. the air pockets and the presence of lesions should be ignored when computing the axis of symmetry [4]. Shaped-based method uses the geometric landmarks or topological features of the head such as inter-hemispheric fissure to extract and detect the orientation of MSP of the brain which denotes the symmetry plane [5, 10]. All parallel axial slices, the inter-hemispheric fissure lines are parallel with the same orientation of patient's head [11]. In this study, the concentration will be on shape-based method to determine the orientation of the patient's head instead of depending on measuring symmetry to identify the MSP of brain. The proposed method is based essentially on using PCA method to compute the distinctive principle axes that are orthogonal to each other. Those axes are used to characterize the patient's head by representing the spatial distribution of the mass. Such that any plane of symmetry in a body is orthogonal to a principle axis [5, 12].The remainder of the paper is organized as follows, in Section 2, we review some related work and introduce the contribution of this research. In Section 3, material and methods are described. The experimental results are discussed in Section 4. Finally, the conclusions are drawn in section 5.

II. Related Works

The Mid-Sagittal Plane (MSP) of the brain is a plane that separates it into two halves known as the two hemispheres of the brain. Identifying this plane is considered important for many automated systems that measures the similarity between the two hemispheres. Therefore, the detection of MSP is a topic that has been investigated for decades [13]. Liu, et al. [4] , Liu and Collins [14] and Ardekani, et al. [7] proposed an automated algorithm for detecting the MSP based on the symmetry axis that should have the same orientation of the patient's head. Hence, the process is that of searching for the orientation of the reflection line that maximizes the cross-correlation between the original image and the rotated image. Bergo, et al. [10] proposed an automated method for detecting the longitudinal fissure, which is clearly visible in T1-w images. The author assumed that the MSP contains a maximal area of

Cerebrospinal fluid (CSF), which appeared as a low intensity area. Therefore, the proposed method was based on searching of a sagittal plane that minimized the intensity mean. Ruppert, et al. [3] proposed an algorithm for extracting the MSP by searching the plane that maximizes a bilateral symmetry measure. The bilateral symmetry measurement was based on extracting the edge features from the MRI brain image. Then measuring the similarity using the correlation between the left and right hemispheres with respect to a candidate cutting plane. Jayasuriya and Liew [1] proposed an automated algorithm for detecting the MSP of the brain by exploiting the property that the longitudinal fissure in T1-w images appears as a dark area. A set of lines were drawn in multiple angles to analyze the intensity along these lines. The best possible line that fits the inter-hemispheric fissure which represents the angle of the MSP to the vertical axis was chosen. Nabizadeh and Kubat [15], Ray, et al. [16] and Saha, et al. [17] separated the brain into two hemispheres by finding the longest diameter that represents the MSP of the brain. Their algorithm included separating the brain from the background, finding the brain center, finding the brain's borderline, determining the lengths of all possible brain diameters and assign the longest diameter as the MSP of the brain. The previous works have shown different techniques for detecting MSP of the brain as summarized in Table 1. However, the intensity-based analysis methods (symmetry, fissure) might not be the optimal solution to identify the MSP, because they are sensitive to any pathological conditions that could induce asymmetries and displacement of anatomical structures of the brain [4, 13, 14].

In this study, the emphasis is on estimating the orientation of the skull that is identical to the reflection line and passes through the MSP of the brain [11, 14].

III. MATERIAL AND METHODS

The main objective of this research is to investigate the use of orientation of the skull to detect the MSP of brain and correct it. The proposed method includes the following steps; background segmentation, orientation determination, geometrical transformation, and centralize patient's head in the center of MRI slice. The flow chart of the proposed method is shown in Fig. 1.

A. Data Collection

The same dataset of MRI brain scans that was used in [12, 18], is used in this study. The dataset was collected were collected by using a SIEMENS MAGNETOM Avanto 1.5 Tesla scanner and PHILIPS Achieva 1.5 Tesla scanner.

B. Image Denosing

The removal of noise from noisy data to obtain the unknown signal is known as denoising. Magnetic resonance (MR) images are usually corrupted by random noise that makes a small random modification of the intensity in an individual or small groups. These modifications may be lead to erroneous

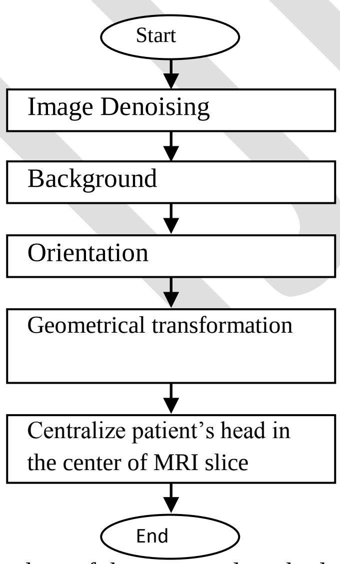

Figure 1: Flow chart of the proposed method.

segmentation and feature extraction. Recently, wavelet transform has been used significantly as a popular method in various applications for data analysis and image processing. Several algorithms based wavelet transform has been proposed for denoising of MRI images [19]. In this study, a wavelet transform based bilateral filter as described in [19] is used to denoise the MRI images. First, the MRI images are decomposed into multi-level to extract the approximation and the detailed sub-bands as shown in Fig. 2. Then, bilateral filter is used to denoise the approximation sub-band to improve the visibility of MRI images with preserving relevant edge features. Finally, inverse wavelet transform is performed to reconstruct the denoised MRI images.

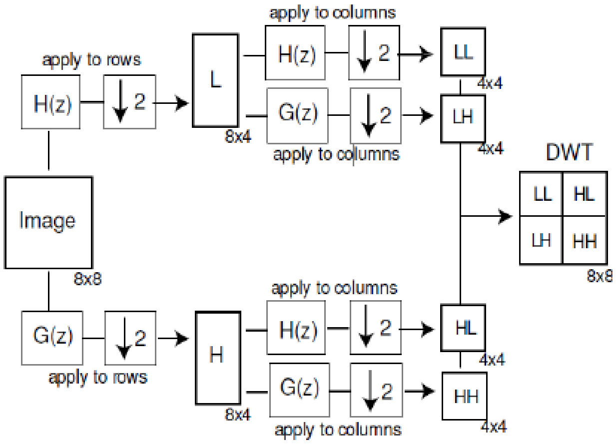

Figure 2: MRI image decomposition by two-dimensional wavelet transform.

Table 1: Summary of existing MSP methods.

Method	Features
Junck, et al. [20]	Symmetry/ Intensity cross correlation
Liu and Collins [14]	Symmetry/ Intensity cross correlation
Ardekani, et al. [7]	Symmetry/ Intensity cross correlation
Liu [5]	Symmetry/ Intensity cross correlation
Bergo, et al. [10]	Symmetry/ Intensity cross correlation
Ruppert et al. (2011)	Symmetry/ Intensity cross correlation
Prima and S. [21]	Symmetry/ Intensity cross correlation
Tuzikov, et al. [22]	Symmetry/ Intensity cross correlation
Jayasuriya and Liew [1]	Fissure/ Minimized the intensity mean
Hu and Nowinski [11]	Fissure/ Local symmetry index
Ray, et al. [16]	Longest diameter
Saha, et al. [17]	Longest diameter
Nabizadeh and Kubat [15]	Longest diameter

C. Background Segmentation

Due to the prior knowledge that the background intensity values of MRI brain slices is always approach to zero. Therefore, it is important to eliminate and exclude this part of MRI image from implementation because it normally has much higher number of pixels without meaningful information than the brain region [23]. In this study, histogram thresholding method is used as a simplest segmentation method to segment the background of MRI brain slice based on thresholding the intensity values by a specific threshold *T* value. Such that, if the intensity value of pixel is greater than *T* then the pixel is considered as brain region, otherwise is considered as background [24]. The *T* can be determined as either manually which is specified by user or automatically by using different approaches [25-28]. In this study, it is noted that the histograms of two different MRI T2-w images' have approximately the same shape of distributions [29] as shown in Fig. 3. Therefore, *T* value is selected experimentally and set to 0.1 after the effect of a range of threshold values 0.05, 0.1, 0.2, and 0.3 had been manually observed. Consequently, if an intensity value of pixel is less than 0.1, it is considered as a background. This histogram thresholding is implemented by using *im2bw* function with specific value of threshold in MATLAB Image Processing Toolkit [30]. Then it is followed by implementing a set of morphological operators in sequence to remove any holes that may be available in the head region. There are many morphological operators but only two operators are essential and can be combined in many ways to produce more complex morphological operators which can solve different problems in image analysis. These two operators are dilation and erosion. The dilation is an operation that is used to increase the size of objects which are located in the foreground or appeared as white pixels in binary images. While, the erosion is an operation that is used to increase the size of background objects and decrease the foreground objects in binary images [25, 31, 32]. Additionally, holes filling morphological operator is used to fill holes that are defined as a background region of a binary image and surrounded by connected borders of foreground regions [27, 33, 34]. In this study, the deficiencies of segmentation process are overcome by dilating the segmented MRI brain scanning image using dilation morphological operator.

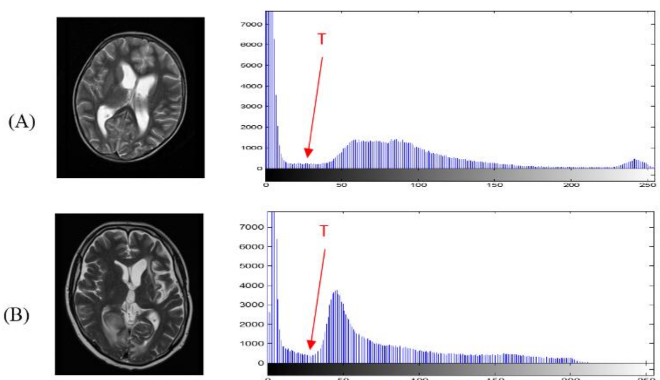

Figure 3: T2-w MR images of two different patients and corresponding histograms.

Then the internal holes are filled using holes filling morphological operator. Consequently, a binary mask with one's denotes the patient's head, and zero's denotes the background. This mask is then multiplied with the original slice image to produce a new slices image without background. Fig. 3 shows an example of how the MRI image is segmented, dilated and holes filled.

The PCA method essentially attempts to transfer the coordinate of original data to a new coordinate system. Such that the maximum variation in the data comes to lie on the first coordinate, it is known the first principal component. The second maximum variation in the data lies on the second coordinate and so on.

The most common steps that are followed by radiologists and clinicians in MRI units and specifically in MRI Unit of Al-Kadhimiya Teaching Hospital, include positioning and aligning the patient's head inside the head coil according to the laser light indicator, and using sponges to support and minimize the head tilt and rotation. This gives better MRI image quality [35]. Due to all brain slices in the same scan have the same symmetry axis orientation [4], it is possible to detect the degree of skewness to the left or right by using single slice in axial viewing instead of using all brain slices in context of reducing computational complexity. In this study, we assume that the patient's head may be skewed only either left or right.

Let D is an original two-dimensional data with two observations that are plotted on X and Y coordinates. The PCA is used to map linearly these coordinates into new X' and Y' coordinates, where X' extends along the direction of the maximum variation of given data and Y' is perpendicular on X' extends along the direction of the minimum variation of given data as shown in Fig. 4 [36]. In this study, D represents the coordinates of pixels in foreground part of the segmented MRI brain image, such that X=[X_1, X_2, …., X_n], and Y=[Y_1, Y_2, ….., Y_n]. These coordinates are normalized by subtracting the mean from each one according to following Eq. 1, and Eq. 2:

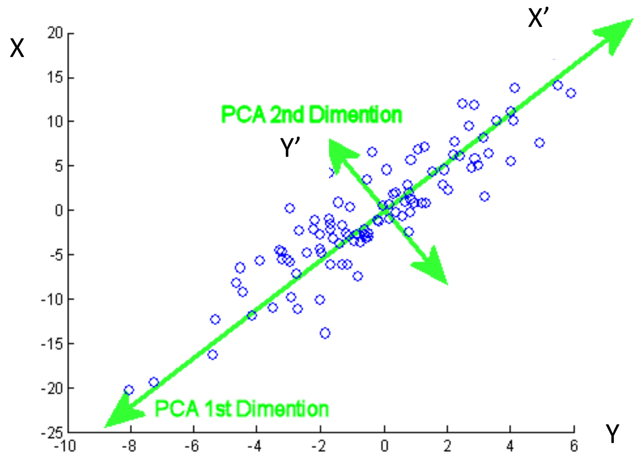

Figure 4: Remapping the axes (X, Y) of original data into new axes (X', Y').

$$\bar{X} = \frac{1}{n}\sum_{i=1}^{n} X_i \qquad (1)$$

$$\bar{Y} = \frac{1}{n}\sum_{i=1}^{n} Y_i \qquad (2)$$

The covariance matrix (cov) that is symmetrical and semi-positive definite matrix, is used to measure to which extent that these coordinates are linearly related as given in Eq. 3.

$$cov(x, y) = \frac{1}{(n-1)}\sum_{i=1}^{n}(X_i - \bar{X})(Y_i - \bar{Y}) \qquad (3)$$

If the given data has *m* dimensions, the covariance matrix is an *m* by *m* matrix [36, 37]. Then the eigenvectors and eigenvalues can be calculated by using the following Eq. 4 and Eq. 5 respectively. Where, the eigenvectors and eigenvalues include useful information about the new coordinates of the given data [38]. Each eigenvector points in the direction of a new coordinate axis. The desirable coordinate that has the highest eigenvalues, represents the axis that includes the most variation in the given data. It is also known the first principle component. This means that the required new coordinate X'-axis passes through the maximum variation of given data and points from the original central point to the first principle component [32, 36]:

$$|cov - \lambda I| = 0 \qquad (4)$$

$$cov.V = \lambda V \qquad (5)$$

Where λ is the eigenvalues of the covariance matrix, *I* is the identity matrix and *V* is the eigenvectors matrix.

Then, the angle θ between the X-axis and X`-axis represents the degree of skewness of patient's head during the MRI test as shown in Fig. 5. It could be calculated by using Eq. 6:

$$\theta = \tan^{-1}\frac{V_2}{V_1} \qquad (6)$$

Where, V_1 and V_2 are the eigenvectors values which are related to the maximum eigenvalues.

The main shortcut of PCA that is not efficient to distinguish between the axis of symmetry and axis of orientation. However, it is still interesting approach because of simplicity and the low processing time [9].

The PCA algorithm is implemented by using *princomp* function in MATLAB Image Processing Toolkit [30].

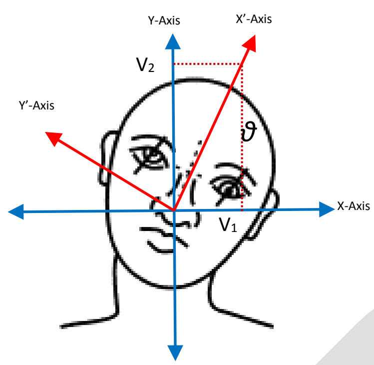

Figure 5: Original and new coordinates of brain.

D. Geometrical Transformation

Geometrical transformation techniques are widely used in computer graphic and image analysis. They help to eliminate the geometric distortion that occurs within image capturing [32]. They can be used to estimate the unknown pixels by interpolation of input pixels and rotate the object around a fixed point known as the center of rotation [39]. A geometric transformation includes two basic steps. First, the pixel coordinates transformation that is used to map the coordinates of the input pixel to the new position in the output image. Second, the brightness interpolation that is used to compute the brightness value in the new image by interpolating the brightness of several input pixels in the neighborhood [32]. There are two types of interpolation techniques; nearest neighbor interpolation and bilinear interpolation [27, 39]. After the angle θ is computed in the previous step, which represents the wobble of patient's head with respect to the horizontal axis of the input image. It becomes easily to correct and rotate the patient's head by using *Geometric Rotator system object* in MATLAB Image Processing Toolkit [30].

E. Centralize Patient's Head in the Centre of MRI slice

The proposed algorithm for extracting texture features in this study is based essentially on measuring symmetry between the two hemispheres of brain. As well as, the MSP of brain is positioned in the middle of the patient's head and the centroid of patient's head is identical with the MSP of brain [4]. Therefore, it becomes easily to make the MSP of brain identical exactly in the middle of MRI brain scanning image by shifting patient's head either left or right using Eq. 7, and Eq. 8:

$$g_x = \frac{1}{N}\sum_{i=1}^{N} x_i \qquad (7)$$

$$g_y = \frac{1}{N}\sum_{i=1}^{N} y_i \qquad (8)$$

Where, N is the number of pixels in the segmented patient's head, and g_x and g_y are the coordinates of centroid. Then the patient's head is shifted by number of pixels that is equal to the difference between g_y and 256 which represent the coordinates of middle line of MRI brain image.

IV. EXPERIMENTAL RESULTS

The proposed algorithm is implemented using MATLAB 2014, and applied on a dataset of MRI brain scans used in [12, 18] and includes T2-weighted images of 165 patients. To evaluate the proposed algorithms used in this study, a set of examples will be implemented using this algorithm.

Since all MRI brain slices have the same MSP orientation [14], the MSP detection and correction algorithm is implemented on a single slice to determine the orientation instead of using all slices to avoid computational complexity. The preferable slice is the bony structures slice which is located in the lower of the brain, and contains the largest number of pixels. It provides more accurate detection rate compared to slices higher in the brain (at the tip of the head) which has ovals or near-circular shape [4].

To compare with an expert clinician delineation, the MSPs of 50 MRI slices from the collected dataset were manually identified by an expert clinician from MRI Unit in Al-Kadhimiya Teaching Hospital. These MRI slices were given to the expert after correcting and aligning the MSPs of these slices. The proper location of the fitted line was drawn with the mouse by the expert. Figure 6, shows mean squared error (MSE) distribution between manual and our algorithm delineation of MSPs. Consequently, 92% of the computed MSPs are matched approximately to clinician's delineation within MSE≤3º.

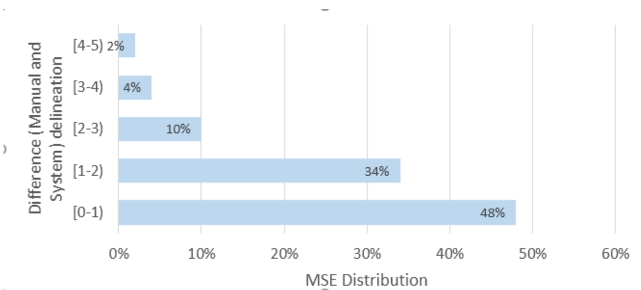

Figure 6: Distribution of MSE between manual and our algorithm.

For further evaluation, the given MRI brain slice in Fig. 7 was resampled and rotated with yaw angles from -10º to 10º in 2.5º intervals using Geometric Rotator system object in MATLAB Image Processing Toolkit [30]. Table 1 demonstrates the result of detecting and computing yaw angles of the given MRI brain slices in Fig. 7 and comparing our results with [14] and [40]. Our algorithm can identify the yaw angle of resampled MRI brain slice with minimum mean squared error (MSE) compared to [14, 40]. Figure 8, shows a comparison of actual and detected yaw angles using our algorithm and the proposed algorithms in [14, 40].

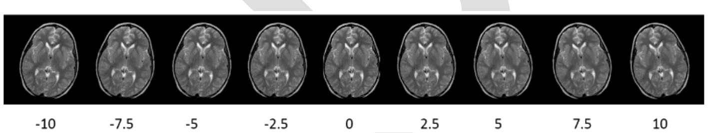

Figure 7: Resampling of one slice from the axial MRI brain scanning image with varied rotate angles.

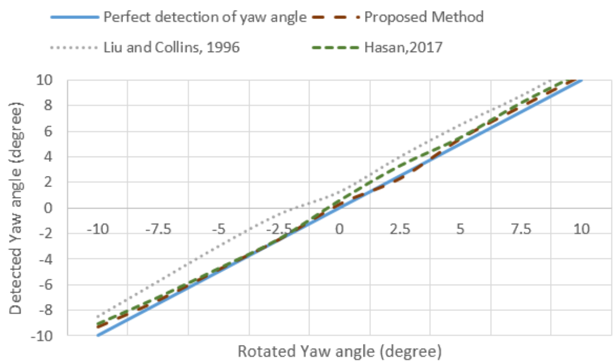

Figure 8: Comparison between actual and detected yaw angles in given MRI brain slice.

V. Conclusion

We have proposed a fast, and accurate method for the MSP estimation in MRI brain scans. This method exploits the orientation of patient's head to locate and identify the MSP. It is based on automatic segmentation of the patient's head and elimination of background. The algorithm works on both normal and pathological brain scans

Table 1: Numerical results of detecting yaw angle.

Yaw Angle	-10°	-7.5°	-5°	-2.5°	0°	2.5°	5°	7.5°	10°	MSE
[40]	-9.08°	-7°	-4.74°	-2.43°	0.58°	3.3°	5.5°	8.21°	10.57°	0.35°
[14]	-8.5°	-5.75°	-3°	-0.5°	1.25°	4°	6.5°	8.75°	11.25°	2.5°
Proposed Method	-9.28°	-7.2°	-4.8°	-2.45°	0.3°	2.3°	5.4°	7.9°	10.3°	0.067°

REFERENCES:

[1] S. Jayasuriya and A. Liew, "Symmetry plane detection in neuroimages based on intensity profile analysis," presented at the International Symposium on Information Technology in Medicine and Education (ITME), Australia, , 2012.

[2] V. Schetinin and A. N. Qureshi, "Computer-aided segmentation and estimation of indices in brain CT scans," 2014.

[3] G. Ruppert, L. Teverovskiy, Y. Chen-Ping, X. Falcao, and L. Yanxi, "A new symmetry-based method for mid-sagittal plane extraction in neuroimages," in *International Symposium on Biomedical Imaging: From Nano to Macro,*, USA, 2011, pp. 285-288.

[4] Y. Liu, R. Collins, and W. Rothfus, "Automatic bilateral symmetry (midsagittal) plane extraction from pathological 3D neuroradiological images," in *Procedings of SPIE 3338, Medical Imaging 1998: Image Processing*, San Diego, USA 1998, pp. 1528-1539.

[5] S. Liu, "Symmetry and asymmetry analysis and its implications to computer-aided diagnosis: A review of the literature," *Journal of Biomedical Informatics,* vol. 42, pp. 1056-1064, 12// 2009.

[6] J. Christensen, G. Hutchins, and C. McDonald, "Computer automated detection of head orientation for prevention of wrong-side treatment errors," *American Medical Informatics Association Annual Symposium Proceedings,*, vol. 2006, p. 136, 2006.

[7] A. Ardekani, J. Kershaw, M. Braun, and I. Kanno, "Automatic detection of the mid-sagittal plane in 3-D brain images," *IEEE Trans Med Imaging,* vol. 16, pp. 947-52, Dec 1997.

[8] H. Khotanlou, O. Colliot, J. Atif, and I. Bloch, "3D brain tumor segmentation in MRI using fuzzy classification, symmetry analysis and spatially constrained deformable models," *Fuzzy Sets and Systems,* vol. 160, pp. 1457-1473, 5/16/ 2009.

ISSN 2091-2730

[9] P. Schmid, "Segmentation and symmetry measure for image analysis: application to digital dermatoscopy," PhD, PRÉSENTÉE AU DÉPARTEMENT D'ÉLECTRICITÉ, ÉCOLE POLYTECHNIQUE FÉDÉRALE DE LAUSANNE, Switzerland, 1999.

[10] F. Bergo, A. Falcão, C. Yasuda, and G. Ruppert, "Fast, Accurate and Precise Mid-Sagittal Plane Location in 3D MR Images of the Brain," presented at the In International Joint Conference on Biomedical Engineering Systems and Technologies, 2008.

[11] Q. Hu and W. L. Nowinski, "A rapid algorithm for robust and automatic extraction of the midsagittal plane of the human cerebrum from neuroimages based on local symmetry and outlier removal," *NeuroImage,* vol. 20, pp. 2153-2165, 12// 2003.

[12] A. Hasan and F. Meziane, "Automated screening of MRI brain scanning using grey level statistics," *Computers & Electrical Engineering,* vol. 53, pp. 276–291, 2016.

[13] H. J. Kuijf, S. J. van Veluw, M. I. Geerlings, M. A. Viergever, G. J. Biessels, and K. L. Vincken, "Automatic Extraction of the Midsagittal Surface from Brain MR Images using the Kullback–Leibler Measure," *Neuroinformatics,* vol. 12, pp. 395-403, 2014.

[14] Y. Liu and R. Collins, "Automatic Extraction of the Central Symmetry (MidSagittal) Plane from Neuroradiology Images," Robotics Institute, Carnegie Mellon University, USA1996.

[15] N. Nabizadeh and M. Kubat, "Brain tumors detection and segmentation in MR images: Gabor wavelet vs. statistical features," *Computers & Electrical Engineering,* vol. 45, pp. 286–301, 2015.

[16] N. Ray, R. Greiner, and A. Murtha, "Using Symmetry to Detect Abnormalies in Brain MRI," *Computer Society of India Communications,* vol. 31, pp. 7-10, 2008.

[17] B. Saha, N. Ray, R. Greiner, A. Murtha, and H. Zhang, "Quick detection of brain tumors and edemas: A bounding box method using symmetry," *Computerized Medical Imaging and Graphics,* vol. 36, pp. 95-107, 2012.

[18] A. Hasan, F. Meziane, and M. Abd Kadhim, "Automated Segmentation of Tumours in MRI Brain Scans," presented at the Proceedings of the 9th International Joint Conference on Biomedical Engineering Systems and Technologies (BIOSTEC 2016), Rome, Italy, 2016.

[19] Y. Wang, X. Che, and S. Ma, "Nonlinear filtering based on 3D wavelet transform for MRI denoising," *EURASIP Journal on Advances in Signal Processing,* vol. 2012, p. 40, 2012.

[20] L. Junck, J. G. Moen, G. D. Hutchins, M. B. Brown, and D. E. Kuhl, "Correlation methods for the centering, rotation, and alignment of functional brain images," *Journal of nuclear medicine: official publication, Society of Nuclear Medicine,* vol. 31, pp. 1220-1226, 1990.

[21] S. Prima and O. S., "Computation of the mid-sagittal plane in 3-D brain images,," *IEEE Transactions on Medical Imaging,,* vol. 21, pp. 122-138, 2002.

[22] A. V. Tuzikov, O. Colliot, and I. Bloch, "Evaluation of the symmetry plane in 3D MR brain images," *Pattern Recognition Letters,* vol. 24, pp. 2219-2233, 10// 2003.

[23] N. Nabizadeh, "Automated Brain Lesion Detection and Segmentation Using Magnetic Resonance Images," PhD, Department of Electrical and Computer Engineering, University of Miami, USA, 2015.

[24] S. Naji, R. Zainuddin, S. Kareem, and H. Jalab, "Detecting Faces in Colored Images Using Multi-skin Color Models and Neural Network with Texture Analysis.," *Malaysian Journal of Computer Science,* vol. 26, 2013.

[25] G. Dougherty, *Digital Image Processing for Medical Applications*. Cambridge University Press., 2009.

[26] T. Morris, "Image Processing with MATLAB," ed. Manchester University.

[27] J. Wilson and G. Ritter, *Handbook of Computer Vision Algorithms in Image Algebra*: CRC Press, Inc., 2000.

[28] I. Bankman, *Handbook of medical imaging*: Academic Press, Inc., 2000.

[29] A. Udomchaiporn, F. Coenen, M. García-Fiñana, and V. Sluming, "3-D MRI Brain Scan Feature Classification Using an Oct-Tree Representation," in *Advanced Data Mining and Applications*, ed: Springer, 2013, pp. 229-240.

[30] Matlab, "The Math Works kit," ed, 2013.

[31] A. Bovik, *The Essential Guide to Image Processing*. Elsevier Inc, 2009.

[32] M. Sonka, V. Hlavac, and R. Boyle, *Image Processing, Analysis, and Machine Vision*: Cengage Learning, 2014.

[33] R. Gonzalez and R. Woods, *Digital Image Processing*, 3re Edition ed.: Prentice-Hall, Inc., 2002.

[34] P. Soille, *Morphological Image Analysis: Principles and Applications*: Springer-Verlag New York, Inc., 2003.

[35] UC Davis Medical Center, "Troubleshooting Guide; Prep, Scan Errors, and Artifacts," USA, University of California, USA2016.

[36] P. Wallisch, M. Lusignan, M. Benayoun, T. Baker, A. Dickey, and N. Hatsopoulos, *Matlab for Neuroscientists*: Elsevier, 2014.

[37] B. Manly, *Multivariate Statistical Methods A primer*. New Zealand: University of Otago, 1988.

[38] L. I. Smith, "A tutorial on Principal Components Analysis," *Cornell University, USA*, vol. 51, p. 52, 2002.

[39] K. William, *Digital Image Processing*, 3 ed. Canada: Wiley-Interscience, 2001.

[40] A. Hasan, "An automated system for the classification and segmentation of brain tumours in MRI images based on the modified grey level co-occurrence matrix," PhD, Computing, Science and Engineering, University of Salford, UK, 2017.

COMPARISON OF APRIORI, FP-TREE GROWTH AND FUZZY FP-TREE GROWTH ALGORITHM FOR GENERATING ASSOCATION RULE MINING OF COGNITIVE SKILL

Dr. M. Mayilvaganan, D. Kalpanadevi
Associate Professor, Research Scholar
Department of Computer Science, PSG College of Arts and Science
kalpanapani@gmail.com

Abstract— **:** In this research, focuses on implication of association rules among the quantitative attributes and categorical attribute of a database employing fuzzy logic and Frequent Pattern Tree growth algorithm. In the first stage, apply fuzzy partition methods and use triangular membership function of quantitative value for each transaction item, for the generation of more realistic association using fuzzy intervals among quantitative attribute. In second stage, implement Frequent Pattern Tree growth for deal with the process of data mining to analyze the frequent pattern item. In addition, in order to understand the impact of Apriori algorithm and FP-Tree growth algorithm on the execution time, accuracy of best rule found from the frequent pattern mining and the number of generated association rules, the experiment can be performed by using different sizes of support count. In third stage, an experiment results shows Fuzzy FP- Tree growth algorithm is more efficient than existing methods of Apriori and FP Tree growth algorithm.

Keywords— Apriori algorithm; FP-Tree growth algorithm; Fuzzy FP- Tree growth; fuzzy partition methods; triangular membership function; support count; confidence

INTRODUCTION

In data mining, the association rules are used to finds for the associations between the different items of the transactions database. The research focuses the cognitive skill analysis from the students in Numerical Ability, Logical Reasoning and Perceptual Speed. In this paper, the scope of the research is the question type is split as simple, moderate and complicated and the scoring result under the different categories of questions in numerical ability and Logical reasoning. Each should be split into three intervals such as Low, Medium and High can be implemented in frequent pattern mining in Fuzzy FP tree growth for generating fuzzy association rule and analyse the cognitive complexity level of student.

MATERIALS AND METHODS

APRIORI ALGORITHM

In Apriori algorithm, an association rule generation process can be represented in two steps [1] [7][10]:

1. In the First, minimum support is applied for find out the satisfied frequent item-sets.
2. In the Second, minimum confidence can be found out from the required frequent item-sets and constraints are used to mine all association rules.

Apriori algorithm works continuously repeated to scan the database. It uses breadth-first search and a tree structure to count candidate item sets efficiently. Let us assume that it generates candidate item sets of length i from item sets of length $i - 1$. Then it prunes the candidates which have an infrequent sub pattern. Finally find out all possible combination of frequent item-sets until it does not generate candidate item. Downward closure property of support give the guarantee of frequent item-set contains all frequent i-length item sets [11].

Apriori does not filter prior candidate item-set, it helps to reduce the amount of candidate item-sets to scan. Therefore it needs more time to complete the scanning a database. By implementing process it is not completely efficient.

The support supp(X) of an item-set X is defined as the proportion of transactions in the data set which contain the item-set which can be calculated by the equation (1) [9][1].

$$\text{Supp (X)} = \frac{\text{(no. of transactions which contain the itemset X)}}{\text{(total no.of transactions)}} \quad (1)$$

The confidence of a rule is defined to interpreted as an estimate of the probability P(Y | X), the probability of finding the right hand side of the rule in transactions under the condition that these transactions also contain the left hand side from the equation 2.

$$\text{Confidence(X=>Y)} = \frac{\text{support}(X \cup Y)}{\text{support}(X)} * 100\% \quad (2)$$

In this research, to construct the fuzzy intervals [8] and explore the Frequent Pattern Mining algorithm, apply to the sample database of students scored data such as marks attained in numerical and logical reasoning which is illustrated in table 5.1. The model parameter of output variable of cognitive skill of required attributes are broken down into 3 fuzzy sets low, medium and high is The fuzzy frequent item sets, represented by linguistic terms are derived from the fuzzy FP-tree. The count of a fuzzy item set obtained by a fuzzy intersection (minimum) operator can be easily achieved without scanning the database.

FP-TREE GROWTH ALGORITHM

FP- Tree Growth is an algortihm [3] that generates frequent itemsets from an FP-Tree [7] [9] by Divide and Conquer Strategy. Insert sorted items by frequency into a pattern tree. It construct conditional frequent pattern tree and insert sorted item by conditional pattern base which satisfy minimum support. To discover the frequent itemset without candidate item generation which is constructed using 2 passes over the dataset, In pass 1 to scan the transaction data form database and find support for each item,then gradually increase the support and discarded the infrequent items, then sort in decreasing order [12]. In pass 2, FP growth read transaction at a time and maps it to a path. To allocate each item node in tree, each item can link with each node based on single linked list. Fixed order is used, so, path may overlap when transactions share the item. Finally, the header table mines the conditional pattern tree which finds out all frequent item-sets in recursive manner. It does not need association length to proceed phases which generate candidate item-sets in Apriori [1].

PROPOSED METHODOLOGY -FUZZY FP-TREE GROWTH ALGORITHM

In this research, implication of association rules among the quantitative attributes and categorical attributes of a database employing fuzzy logic and frequent pattern growth algorithm. Before applying FP tree growth algorithm, to partitioning the attributes is split into three intervals using triangular membership function. In fuzzy set, the membership degree of each element is any value in between 0 and 1, where the membership degree of each fuzzy class is characterized by using triangular membership functions. These fuzzy intervals lead to the generation of more meaningful and right association rules than classical intervals.

DATA BASE COLLECTION OF NUMERICAL ABILITY AND LOGICAL REASONING SCORING BY THE CATEGORY OF QUESTION TYPE

The representation of numerical and logical reasoning can be split into simple, moderate and complicated, and each should be split into three intervals such as Low, Medium and High for generating fuzzy association rule.

In this research, to construct the fuzzy intervals and explore the Frequent Pattern Mining algorithm [4], apply to the sample database of students scored data such as marks attained in numerical and logical reasoning which is illustrated in table 1. The model parameter of output variable of cognitive skill of required attributes are broken down into 3 fuzzy sets low, medium and high is shown in table 2.

Table 1: Training Database for students scored in Numerical Ability and Logical Reasoning

Transaction ID	Transaction Items					
	Numerical Simple	**Numerical Moderate**	**Numerical Complicate**	**Logical Simple**	**Logical Moderate**	**Logical Complicate**
1	5	4	2	4	2	2
2	5	3	2	5	4	3
3	5	5	2	3	0	4
4	5	3	2	3	1	3
5	3	3	2	5	4	3
6	5	4	2	5	5	4
7	4	2	2	5	4	3
8	5	4	3	5	0	3
9	5	4	5	5	3	1
10	5	4	4	5	1	2
11	5	4	3	2	4	4
12	2	2	3	5	4	2
13	5	3	4	5	5	3
14	2	2	4	5	4	1
15	5	2	3	5	5	1
16	5	5	2	4	1	2
17	4	3	2	5	5	3
18	5	4	2	2	5	4
19	5	5	4	5	1	2
20	5	5	5	5	2	2
21	3	3	2	4	5	2
22	5	3	4	5	1	2
23	3	2	2	5	3	2
24	4	4	2	5	5	2

Table 2: Numerical Ability question level Split by Simple, Moderate and Complicated for Associate rule mining of identifying the scoring of students

Ranges	Total Marks	Constructing an Interval of fuzzy Region	Ranges for Numerical Ability	Ranges for Logical Reasoning
Simple	5	0 - 1.6 0.7 - 3.4 2.6 – 6	Low -NS.Low Medium -NS.Medium High -NS.High	Low -LS.Low Medium -LS.Medium High - LS.High
Moderate	5		Low -NM.Low Medium-NM.Medium High -NM.High	Low -LM.Low Medium-LM.Medium High -LM.High
Complicate	5		Low -NC.Low Medium -NC.Medium High -NC.High	Low -LC.Low Medium - LC.Medium High -LC.High

CONSTRUCTING FUZZY INTERVALS

The construction of fuzzy Intervals of quantitative attribute is split into three fuzzy intervals by applying statistical approach. The lower border of first intervals is the minimum value over domain of the quantitative attributes. The higher border is computed by using the mean and standard deviation of the value of quantitative attributes [6].

In this research, triangular membership function is used to construct the membership function [2] specified by three parameters (boundaries): Lower limit value (left vertex), upper limit value (right vertex) and modal value (center vertex). In the fuzzy region, the representation of triangular membership function with highest is 1 at the center of the fuzzy region. Where x can be represents the ranges of input value in numerical type of the attributes. A_i^l denotes lower limit value, A_i^u denotes upper limit value and M_i denotes modal value in fuzzy region. The modal value M_i kept in any region which can be computed as $M_i = \frac{A_i^l + A_i^u}{2}$.

Before constructing fuzzy interval [8], measure the proper vector of interval values in fuzzy region in the universe of discourse [5]. Let X= {1, 2, 3, 4, 5} be the universe of discourse of the attributes simple, Moderate and complicated. The attributes are split into three intervals such as {low, medium and high}.

From this given universe of discourse of attributes X, the minimum value= 1 and maximum value = 5. Based on measuring the increment unit in the axis of simple, Moderate and Complicated can be defined as equation 5.1.

$$IncreC = \left[\frac{A_i^{\max} + A_i^{\min}}{|A_i|} * w \right] \quad (5.1)$$

Where $A_i^{\max}$ the maximum is value of A_i, $A_i^{\min}$ is the minimum value of A_i and $|A_i|$ is the number of distinct value of A_i and w is the positive integer user-defined weight for control the number of regions needs to be created. It helps to define the vector of interval values of fuzzy regions in the universe of discourse. Similarly, increment unit of Moderate and Complicated attributes can be measured.

In this research, suppose an attribute of A contains minimum value = 0 and maximum value =5 and assumes the weight of the increment unit w= 1 and substitute in the equation 5.1 and computed as 5.2, then we get the increment unit of the interval is

$$Incre(simple_i) = \frac{0+6}{6} * 1 = 1$$

$$Incre(Moderate_i) = \frac{0+6}{6} * 1 = 1$$

$$Incre(Complicate_i) = \frac{0+6}{6} * 1 = 1 \quad (5.2)$$

So, the vector unit of each Attribute - Simple, Moderate and Complicated is {0, 1, 2, 3, 4, 5, 6}. Here the last unit of 6 with k= 1 satisfies the condition 4< $A_i^{\max}$ =5 $\leq$ 6.

Constructing the fuzzy region, to shape the membership functions of an input attribute is affected by the result of overlap measure by the equation of 5.3.

$$Overlap(A_l, A_S) = \frac{\left|F^i_{com}(A_l, A_S)\right|}{\left|F^i_{all}(A_l, A_S)\right|} \quad (5.3)$$

Where $\left|F^i_{com}(A_l, A_S)\right|$ represents the value of {a_{ij}, $a_{ik, ..}$ a_{in}} and in the same region belong to the required set of classes in A_l and the value of {{a_{ip}, $a_{iq, ..}a_{iu}$}} and in the same region belong to the required set of classes in A_S. $\left|F^i_{all}(A_l, A_S)\right|$ represent all values of classes in A_l and A_s. The proposed measure for computing the degree of overlap between the adjacent fuzzy regions A_l, A_S is computed.

Initial parameters of attribute Simple, Moderate and Complicates fuzzy region created as A_1, A_2 and A_3.

Let us assign an initial value of intervals and fuzzy region of A_1 (Low) is created with parameter A_1= {0,1} and M_1 =0.5 i.e., ((0+1)/2), A_2 (Medium) is created with the parameter={1,2,3} and its modal value M_2 = 2 i.e., ((1+3)/2)) and A_3 (High) is created with the parameter={3,4,5} and its modal value M_3 =4 i.e., ((3+5)/2) .

The degree of overlap between adjacent functions of new output attribute is assumed as 50%. Let to find out the lower limit and upper limit of each interval, by measuring the degree of overlap of adjacent fuzzy region referred as £, where 0<£ <1, i.e., $£_1$= overlap (A_1, A_2) and $£_2$= overlap (A_2, A_3) then the upper border value of fuzzy region A_1 will be change by the equation 5.5, due to the percentage amount of overlap between the regions A_1^U is shift inside the region of A_2; Further the lower border value of fuzzy region A_2 is calculated by equation 5.6, here the percentage amount of is shift inside of A_1 region. The value of A_2^l will change from the assigning value and updated by overlapping. Similarly, to find the upper and lower border of A_2^U, A_3^l, A_3^U, where A_3^U = Max (quantitative_ attribute) by the equation of 5.7 to 5.9. In all cases the modal value M_1, M_2 and M_3 cannot change.

To find the first intervals, £= overlap (A_1, A_2) = 0.3, here M_1=1.

$$A_1^l = \min(quantitative\_attributes) \quad (5.4)$$

$= 0$

$$A_1^U = \left(A_2^U - A_2^l\right) * £_1 + A_1^U \quad (5.5)$$

A_1^U = (3-1)*0.3+1 = 0.6+1= 1.6

Then we get, the fuzzy region of first interval A_1 = {0, 1, 1.6}

To find the second interval, $£_1$= overlap (A_1, A_2) = 0.3; $£_2$= overlap (A_2, A_3) = 0.2, here M_2=2.

$$A_2^l = A_1^U - (A_1^U - A_1^l) * £_1 \quad (5.6)$$

A_2^l = 1-(1-0)*0.3 =1-0.3 = 0.7

$$A_2^U = \left(A_3^U - A_3^l\right) * £_2 + A_3^l \quad (5.7)$$

International Journal of Engineering Research and General Science Volume 6, Issue 2, March-April, 2018
ISSN 2091-2730

$$A_2^U = (5-3) * 0.2 + 3 = 3.4$$

The fuzzy region of second interval A_2= {0.7, 2, 3.4}

To find the third interval, $£_2$= overlap (A_2, A_3) = 0.2; here M_3=4.

$$A_3^l = A_2^U - (A_2^U - A_2^l) * £_2 \qquad (5.8)$$

$$A_3^l = 3-(3-1)*0.2= 2.6$$

$$A_3^U = \max(\text{Quantitative \_ attribute}) \qquad (5.9)$$

$$= 6$$

The fuzzy region of third interval A_3= {2.6, 4, 6}

Finally to generating the fuzzy region A_1, A_2 and A_3 for attribute of Numerical Simple, Numerical Moderate and Numerical Complicated and Logical Simple, Logical Moderate and Logical Complicated with overlapping the regions successfully as shown in Figure 1.

After finding the intervals, the membership degree of input which represents 'x', by following triangular membership function to computing the degree of each numeric input of attribute which belong to the region A_i function.

This interval has been characterized using the triangular membership function shown in equation 5.10,

$$\mu(x, A_i^l, M_i, A_i^u) = \max\left(0, \min\left(\frac{x - A_i^l}{M_i - A_i^l}, \frac{A_i^u - x}{A_i^u - M_i}\right)\right) \qquad (5.10)$$

The model parameter of output variable of cognitive skill of required attributes are broken down into 3 fuzzy sets low, medium and high.

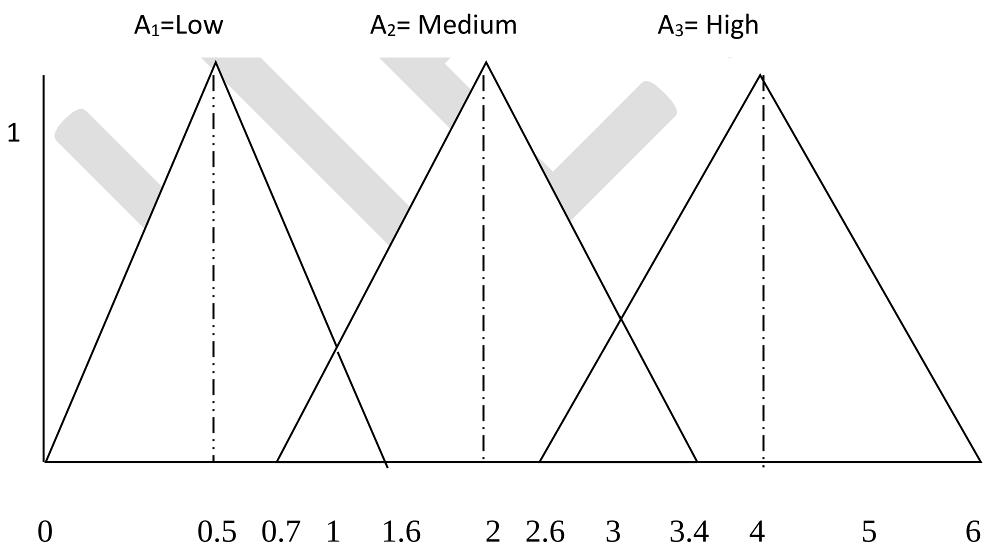

Figure 1 Generating fuzzy regions A_1, A_2 and A_3 attributes of Simple Moderate and Complicated of Numerical and Logical Reasoning with overlapping

Here an linguistic variable of scoring values of simple, moderate and Complicated of Numerical and Logical Reasoning can be split into μ, which can be used to determine the degree to which this input belongs to fuzzy set as below,

$$A_1 = \mu_{Low}(x) = \begin{cases} 0, x < 0 \\ \dfrac{(x-0)}{0.5}, 0 < x \le 0.5 \\ \dfrac{(1.6-x)}{1.1}, 0.5 < x < 1.6 \end{cases} \quad (5.11)$$

$$A_2 = \mu_{Medium}(x) = \begin{cases} \dfrac{(x-0.7)}{1.3}, 0.7 \le x \le 2 \\ \dfrac{(3.4-x)}{1.4}, 2 < x < 3.4 \end{cases} \quad (5.12)$$

$$A_3 = \mu_{High}(x) = \begin{cases} \dfrac{(x-2.6)}{1.4}, 2.6 < x \le 4 \\ \dfrac{(6-x)}{2}, 4 < x < 6 \end{cases} \quad (5.13)$$

Preprocessing the Domain Values for Associating the Related Data for Research

As the data collected and stored, rules of value can be found through association rules, which can be applied to skill of Numerical Ability and Logical Reasoning question. The question level can Split by Simple, Moderate and Complicated for Associate rule mining as shown in table 1 to identify the scoring of students.

For instance, when x= 1, the membership degree can be computed, the value of mark in any simple, moderate and Complicated attribute which belong to fuzzy regions A_1 and A_2 with different degree. Such as μ(1, A_1)= μ(1, 0, 0.5, 1.6) = 1.2 and μ(1, A_2) = μ(1, 0.7, 2, 3.4) = 0.23. Similarly, when X=3, the membership degree can be computed, the value of mark in any simple, moderate and Complicated attribute which belong to fuzzy regions A_2 and A_3 with different degree. Such as μ(3, A_2)= μ(3, 0.7, 2, 3.4) = 0.285 and μ(3, A_3) = μ(3, 2.6, 4, 6) = 0.285.

An overall mapping table from quantitative attribute of table 3, the membership degree of each datum of each domain in fuzzy data base of degree in between 0 and 1. From the below table 3, illustrates the sample training data of 100 tuples scoring simple, moderate and complicated type of numerical ability and logical reasoning.

For instance, to take first 30 tuple from the dataset, it produces 120 fuzzy transaction tuples by fuzzy partitioning as shown in table 4 with membership degree.

The frequency of all items can be measured and represent in table 5. The support of each item is determined by membership degrees of that item in every transaction or tuple from table 4. Here, the minimum membership value of each tuples assigned as an overall membership degree of that tuple. Thus the database contains non-zero membership degree of that every tuple.

The support count can be measured by the summing of all membership degree of that required item in every transaction. For example, the support of NS.High is 28.145; i.e., the membership degree of NS.High is 0.5+0.285+0.285+0.285+0.285+0.285+0.23+0.285+0.285+...+0.285+0.285=28.145 which can be summed in the fuzzy set of each tuple. Similarly, the remaining support of all items can be found in the table 4 respectively. In this research, assumed support is 23% for 120 transactions as given in the table 3, then the required frequent items in table 6 considered as a header table. Remaining infrequent items are discarded from the transaction. According to the selection of support count, NS.Medium, LS.Medium, LS.Low, and LC.Low are infrequent items and frequent items can be representing in table 6. Finally, an each transaction of can sort in descending order with respect to frequent item as shown in table 7 respectively. Here transaction data of ‘0’ consider as not attended the corresponding type of question during the test.

Table 3 Fuzzy Set transformed after partition the quantitative data from the data transaction

T.Id	Numerical Simple	Numerical Moderate	Numerical Complicate	Logical Simple	Logical Moderate	Logical Complicate
1	0.5/NS.High	1/NM.High	1/NC.Medium	1/LS.High	1/LM.Medium	1/ LC.Medium
2	0.5/NS.High	0.285/NM.Medium and 0.285/NM.High	1/NC.Medium	0.5/LS.High	1/LM.High	0.285/ LC.Medium and 0.285/LC.High
3	0.5/NS.High	0.5/NM.High	1/NC.Medium	0.285/LS.Medium and 0.285/LS.High	1.2/LM.Low and 0.23/LM.Medium	1/LC.High
4	0.5/NS.High	0.285/NM.Medium and 0.285/NM.High	1/NC.Medium	0.285/LS.Medium and 0.285/LS.High	1.2/LM.Low and 0.23/LM.Medium	0.285/ LC.Medium and 0.285/LC.High
5	0.285/NS. Medium and 0.285/High	0.285/NM.Medium and 0.285/NM.High	1/NC.Medium	1.2/LS.Low and 0.23/LS. Medium	1/LM.High	0.285/ LC.Medium and 0.285/LC.High
6	0.5/NS.High	1/NM.High	1/NC.Medium	1/LS.Medium	0.5/LM.High	1/LC.High
7	1/NS.High	1/Medium	1/NC.Medium	0.5/LS.High	1/LM.High	0.285/ LC.Medium and 0.285/LC.High
8	0.5/NS.High	1/NM.High	0.285/NC.Medium and 0.285/NC.High	0.5/LS.High	1.2/LM.Low and 0.23/LM.Medium	1.2/ LC.Low and 0.23/ LC.Medium
9	0.5/NS.High	1/NM.High	0.5/NC.High	1.2/LS.Low and 0.23/ LS.Medium	0.285/LM.Medium and 0.285/LM.High	1.2/ LC.Low and 0.23/ LC.Medium
10	1/NS.High	1/NM.High	1/NC.High	0.5/LS.High	1.2/LM.Low and 0.23/LM.Medium	1/ LC.Medium
11	0.5/NS.High	1/NM.High	0.285/NC.Medium and 0.285/NC.High	1/LS.Medium	1/LM.High	1/LC.High
12	1/NS.Medium	1/NM.Medium	0.285/NC.Medium and 0.285/NC.High	0.5/LS.High	1/LM.High	1/ LC.Medium
13	0.5/NS.High	0.285/NM.Medium and 0.285/NM.High	1/NC.High	0.5/LS.High	1.2/LM.Low and 0.23/LM.Medium	0.285/ LC.Medium and 0.285/LC.High
14	1/NS.Medium	1/NM.Medium	1/NC.High	0.5/LS.High	1.2/LM.Low and 0.23/LM.Medium	1.2/ LC.Low and 0.23/ LC.Medium
15	0.5/NS.High	1/NM.Medium	0.285/NC.Medium and 0.285/NC.High	0.5/LS.High	0.5/LM.High	1.2/ LC.Low and 0.23/ LC.Medium
16	0.5/NS.High	0.5/NM.High	1/NC.Medium	1/LS.High	1.2/LM.Low and 0.23/LM.Medium	1/ LC.Medium

T.Id	**Numerical Simple**	**Numerical Moderate**	**Numerical Complicate**	**Logical Simple**	**Logical Moderate**	**Logical Complicate**
17	1/NS.High	0.285/NM.Medium and 0.285/NM.High	1/NC.Medium	0.5/LS.High	0.5/LM.High	0.285/ LC.Medium and 0.285/LC.High
18	0.5/NS.High	1/NM.High	1/NC.Medium	1/LS.Mediu m	0.5/LM.High	1/LC.High
19	0.5/NS.High	0.5/NM.High	1/NC.High	0.5/LS.High	1.2/LM.Low and 0.23/LM.Medium	1/ LC.Medium
20	0.5/NS.High	0.5/NM.High	0.5/NC.High	0.5/LS.High	1/LM.Medium	1/ LC.Medium
21	0.285/NS.Medi um and 0.285/High	0.285/NM.Medium and 0.285/NM.High	1/NC.Medium	1.2/LS.Low and 0.23/LS.Med ium	1.2/LM.Low and 0.23/LM.Medium	1/ LC.Medium
22	0.5/NS.High	0.285/NM.Medium and 0.285/NM.High	1/NC.High	0.5/LS.High	1.2/LM.Low and 0.23/LM.Medium	1/ LC.Medium
23	0.285/NS. Medium and 0.285/High	1/Medium	1/NC.Medium	0.5/LS.High	0.285/LM.Medium and 0.285/LM.High	1/ LC.Medium
24	1/NS.High	1/NM.High	1/NC.Medium	0.5/LS.High	0.5/LM.High	1/ LC.Medium
25	0.5/NS.High	0.5/NM.High	1/NC.Medium	1/LS. Medium	0.5/LM.High	1/ LC.Medium
26	0.5/NS.High	1/NM.High	1/NC.Medium	1/LS.High	1/LM.Medium	1/ LC.Medium
27	0.5/NS.High	1/NM.High	1.2/NC.Low and 0.23/NC.Medium	0.5/LS.High	0.285/LM.Medium and 0.285/LM.High	0.285/ LC.Medium and 0.285/LC.High
28	0.285/NS.Medi um and 0.285/High	1/NM.High	1/NC.Medium	0.5/LS.High	1/LM.High	0.285/ LC.Medium and 0.285/LC.High
29	0.5/NS.High	1/NM.High	0.285/NC.Medium and 0.285/NC.High	0.5/LS.High	0	0.285/ LC.Medium and 0.285/LC.High
30	0.5/NS.High	0.5/NM.High	1/NC.High	1/LS. Medium	1/LM.Medium	0.285/ LC.Medium and 0.285/LC.High

Table 4 Fuzzy Database

T. ID	FUZZY SET NS	NM	NC	LS	LM	LC	MEM. DG
1	0.5/NS.High	1/NM.High	1/NC.Medium	1/LS.High	1/LM.Medium	1/ LC.Medium	0.5
2	0.5/NS.High	0.285/NM.Medium	1/NC.Medium	0.5/LS.High	1/LM.High	0.285/ LC.Medium	0.285
3	0.5/NS.High	0.285/NM.Medium	1/NC.Medium	0.5/LS.High	1/LM.High	0.285/LC.High	0.285
4	0.5/NS.High	0.285/NM.High	1/NC.Medium	0.5/LS.High	1/LM.High	0.285/ LC.Medium	0.285
5	0.5/NS.High	0.285/NM.High	1/NC.Medium	0.5/LS.High	1/LM.High	0.285/LC.High	0.285
6	0.5/NS.High	0.5/NM.High	1/NC.Medium	0.285/LS.Medium	1.2/LM.Low	1/LC.High	0.285
7	0.5/NS.High	0.5/NM.High	1/NC.Medium	0.285/LS.Medium	0.23/LM.Medium	1/LC.High	0.23
8	0.5/NS.High	0.5/NM.High	1/NC.Medium	0.285/LS.High	1.2/LM.Low	1/LC.High	0.285
9	0.5/NS.High	0.5/NM.High	1/NC.Medium	0.285/LS.High	0.23/LM.Medium	1/LC.High	0.285
10	0.5/NS.High	0.285/NM.Medium	1/NC.Medium	0.285/LS.Medium	1.2/LM.Low	0.285/ LC.Medium	0.285
11	0.5/NS.High	0.285/NM.Medium	1/NC.Medium	0.285/LS.High	1.2/LM.Medium	0.285/LC.High	0.285
12	0.5/NS.High	0.285/NM.High	1/NC.Medium	0.285/LS.Medium	1.2/LM.Low	0.285/ LC.Medium	0.285
13	0.5/NS.High	0.285/NM.High	1/NC.Medium	0.285/LS.High	1.2/LM.Medium	0.285/LC.High	0.285
14	0.5/NS.High	0.285/NM.Medium	1/NC.Medium	0.285/LS.High	1.2/LM.Low	0.285/ LC.Medium	0.285
15	0.5/NS.High	0.285/NM.Medium	1/NC.Medium	0.285/LS.High	1.2/LM.Low	0.285/ LC.Medium	0.285
16	0.5/NS.High	0.285/NM.Medium	1/NC.Medium	0.285/LS.Medium	1.2/LM.Low	0.285/LC.High	0.285
17	0.5/NS.High	0.285/NM.Medium	1/NC.Medium	0.285/LS.High	1.2/LM.Medium	0.285/ LC.Medium	0.285
18	0.5/NS.High	0.285/NM.Medium	1/NC.Medium	0.285/LS.Medium	1.2/LM.Medium	0.285/ LC.Medium	0.285
19	0.285/NS.Medium	0.285/NM.Medium	1/NC.Medium	1.2/LS.Low	1/LM.High	0.285/ LC.Medium	0.285
20	0.285/NS.Medium	0.285/NM.High	1/NC.Medium	1.2/LS.Low	1/LM.High	0.285/ LC.Medium	0.285
:	:	:	:	:	:	:	:
:	:	:	:	:	:	:	:
114	0.285/NS.Medium	1/NM.High	1/NC.Medium	0.5/LS.High	1/LM.High	0.285/LC.High	0.285
115	0.285/High	1/NM.High	1/NC.Medium	0.5/LS.High	1/LM.High	0.285/ LC.Medium	0.285
116	0.285/High	1/NM.High	1/NC.Medium	0.5/LS.High	1/LM.High	0.285/LC.High	0.285
117	0.5/NS.High	1/NM.High	0.285/NC.Medium	0.5/LS.High	0	0.285/ LC.Medium	0.285
118	0.5/NS.High	1/NM.High	0.285/NC.Medium	0.5/LS.High	0	0.285/LC.High	0.285
119	0.5/NS.High	1/NM.High	0.285/NC.High	0.5/LS.High	0	0.285/ LC.Medium	0.285
120	0.5/NS.High	1/NM.High	0.285/NC.High	0.5/LS.High	0	0.285/LC.High	0.285

International Journal of Engineering Research and General Science Volume 6, Issue 2, March-April, 2018
ISSN 2091-2730

Table 5 Counting of the Frequency Item

SI.No	Items	Frequency Count
1	NS.High	28.145
2	NS.Medium	6.44
3	NM.High	21.59
4	NM.Medium	12.655
5	NC.Medium	23.385
6	NC.High	10.2
7	LS.High	21.525
8	LS.Medium	7.48
9	LS.Low	5.02
10	LM.Low	8.89
11	LM.Medium	10.56
12	LM.High	13.92
13	LC.Low	3.115
14	LC.Medium	21.32
15	LC.High	9.65

Table 6 Header Table

SI. No	Items	Possible Value	Count
1	NS.High	NSH	28.145
2	NC.Medium	NCM	23.385
3	NM.High	NMH	21.59
4	LS.High	LSH	21.525
5	LC.Medium	LCM	21.32
6	LM.High	LMH	13.92
7	NM.Medium	NMM	12.655
8	LM.Medium	LMM	10.56
9	NC.High	NCH	10.2
10	LC.High	LCH	9.65
11	LM.Low	LML	8.89

Table 7 Pre-processed Fuzzy Database

TID	Frequent Item (Ordered)	Mem DG
1	NSH, NCM, NMH, LSH, LCM, LMM	0.5
2	NSH, NCM, LSH, LCM, LMH, NMM	0.285
3	NSH, NCM, LSH, LMH, NMM, LCH	0.285
4	NSH, NCM, NMH, LSH, LMH, LCH	0.285
5	NSH, NCM, NMH, LSH, LMH, LCH	0.285
6	NSH, NCM, NMH, LCH, LML	0.285

7	NSH, NCM, NMH, LMM, LCH	0.23
8	NSH, NCM, NMH, LSH, LCH, LML	0.285
9	NSH, NCM, NMH, LSH, LMM, LCH	0.285
10	NSH, NCM, LCM, NMM, LML	0.285
11	NSH, NCM, LSH, NMM, LMM, LCH	0.285
12	NSH, NCM, NMH, LCH, LML	0.285
13	NSH, NCM, NMH, LSH, LMM, LCH	0.285
14	NSH, NCM, LSH, LCM, NMM, LML	0.285
15	NSH, NCM, LSH, LCM, NMM, LML	0.285
16	NSH, NCM, NMM, LCH, LML	0.285
17	NSH, NCM, LSH, LCM, NMM, LMM	0.285
18	NSH, NCM, LCM, NMM, LMM	0.285
19	NCM, LCM, LMH, NMM	0.285
20	NCM, NMH, LCM, LMH	0.285
21	NCM, LCM, LMH, NMM	0.285
22	NCM, LMH, NMM, LCH	0.285
23	NCM, NMH, LMH, LCH	0.285
24	NCM, NMH, LMH, LCH	0.285
25	NSH, NCM, LCM, LMH, NMM	0.285
26	NSH, NCM, NMH, LCM, LMH	0.285
27	NSH, NCM, LCM, LMH, NMM	0.285
28	NSH, NCM, LMH, NMM, LML	0.285
29	NSH, NCM, NMH, LMH, LCH	0.285
30	NSH, NCM, NMH, LCM, LCH	0.285
:	:	:
:	:	:
117	NSH, NCM, NMH, LSH, LCM	0.285
118	NSH, NCM, NMH, LSH, LCH	0.285
119	NSH, NMH, LSH, LCM, NCH	0.285
120	NSH, NMH, LSH, NCH, LCH	0.285

Let us assume the item in transaction NS.High as NSH, NS.Medium as NSM and other items are termed as in table 6.

An FP-tree is basically a prefix tree in which each path represents a set of transactions that share the same prefix. Then the procedure root= node (), i.e., null which is applied on ordered frequent items from the header table 5.6 to build up FP-tree, which is shown in Figure 2. The header file is build during the construction of FP tree because each item point's first occurrence is in tree via node link. Nodes with same name are linked in sequence via such node links as shown in Figure 1.

ISSN 2091-2730

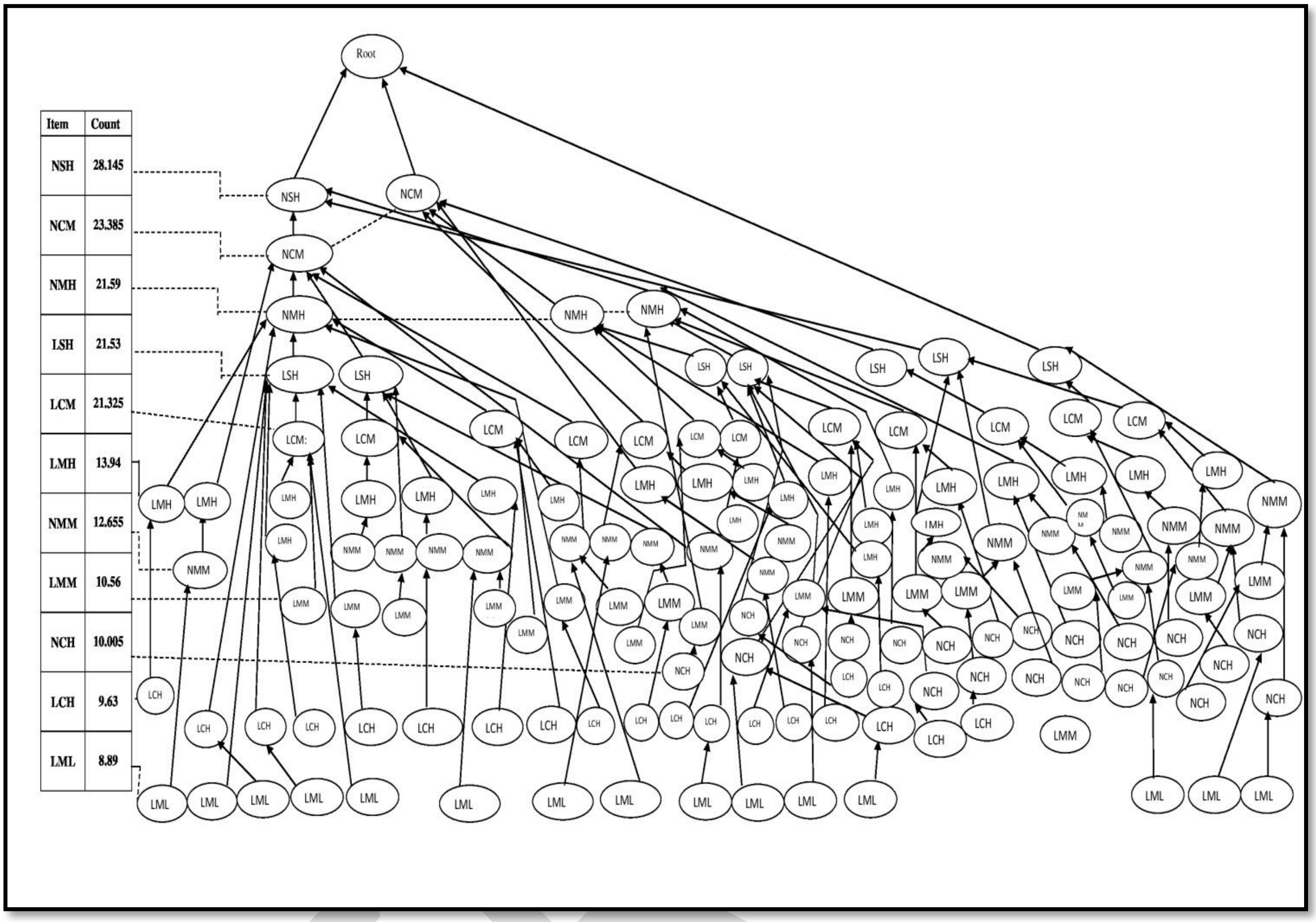

Figure 1 Building Fuzzy FP Tree

According to the procedure, after crating a root termed "null", the first branch is constructed for transaction < NSH, NCM, NMH LSH, LCM, LMM: 0.5>, where six new nodes are created for items NCM, NMH, LCM, LSH, LMM. And the node NSH is linked as the child of root. The root node termed as null. NCM is linked as the child of NSH, NMH is linked as the child of node NCM, LSH is linked as the child of node NMH, LCM is linked as the child of node of LSH and finally LMM is linked as the child of node of LCM. As the next transaction < NSH, NCM, LSH, LCM, LMH, NMM: 0.285> does share common prefix with previous transaction up to NCM. At NCM, a new child node is created and link to LSH and LCM is linked as the child of node LSH, LMH is linked as the child of node LCM and NMM is linked as the child of node LMH. In case, the membership degree of NSH, NCM is added with previous degree in each transaction. Similarly, the remaining transactions are mapped and the tree structure is built. The nineteenth transaction has common prefix < NCM, LCM, LMH, NMM: 0.285>, there is no common nodes in previous transaction, so the second branch is constructed from the root. In this way all transactions are embedded into FP-tree and continue until all transactions are mapped to a path in the FP-tree.

GENERATING FUZZY FREQUENT ITEM-SETS

After completing the FP-tree construction, the conditional pattern base can establish a condition FP-tree, the frequent fuzzy item-sets containing more than one fuzzy region can be found in a way to similar to the FP growth Mining algorithm.

The process of this algorithm, the conditional pattern base from the child node LML and finishes at the root node "Null". Hence the node of LML contains fifteen prefix paths as shown in Figure 2. These are called conditional pattern base of "LML". Similarly, the conditional base of all LCH, NCH, LMM, NMM, LMH, LCM, LSH, NMH, NCM and NSH patterns base can be analyzed from the prefix based on bottom up process in one by one. Finally all conditional pattern bases can be found as shown in table 8.

Table 8 Generating Frequent Item Sets

Item	**Conditional Pattern Base**	**Conditional Frequent item set**
LML	{<NMM, LMH, NCM, NSH: 0.57> <LSH, NMH, NCM, NSH:0.695> <LCM, LSH, NMH, NCM, NSH: 1.53> <LCH, NMH, NCM, NSH: 0.8> <NMM, LCM, LSH, NCM, NSH:0.57> <NMM, LCM, NCM, NSH: 0.57> <LCH, NMM, NCM, NSH: 0.285> <NCH, NMM, LCM, LSH, NSH:0.57> <LCH, NCH, LMM, LSH, NMH,,NSH: 1.025> <NCH, LSH, NMH, NSH: 0.515> <NCH, NMH, LSH, NSH:0.515> <NCH, LCM, LSH, NMH, NSH:1.245>}	<NSH LML: 8.89>
LCH	{<LMH, NMH, NCM, NSH: 0.285> <LMH, NCM, NSH: 0.57> <LMH, LSH, NMH, NCM, NSH: 0.57> <NMH, NCM, NSH : 3.4> <NMM, LMH, LSH, NCM, NSH : 0.57> <LCM, NMH, NCM, NSH: 0.285> <LMM, LSH, NMM, NCM, NSH: 0.715> <LMM, NMM, LSH, NCM, NSH: 0.57> <NMM, NCM, NSH: 0.285> <NMM, LMH, NCM: 0.285> <LMH, NMH, NCM: 0.57> <LMH, NMH, NCM, NSH: 0.8> <NCH, NMM, LSH, NSH: 0.23> <NCH, LMM, NMM, LSH, NSH: 0.515>}	Ø
NCH	{<LMM, NMM, LCM, LSH, NSH :0.8> <NMM, LMH, LCM, LSH :0.855> <LMM, NMM, LCM, LSH, NSH:0.8> <NMM, LMH, NMH, NSH: 0.57> <LMH, NMH, NSH: 0.8> <LMM, NMM, LSH, NSH: 0.515> <NMM, LSH, NSH: 0.515> <LMM, LSH, NMH, NSH :0.46> <LCM, LSH, NMH, NSH: 1.475> <LMM, LCM, LSH, NMH, NSH:0.69> <LCH, LCM, NMH, NSH: 1.03> <LMM, NMH, NSH : 1.03> <LMM, LCM, LSH, NMH, NSH: 0.69 >}	<NSH NCH : 3.115>
Item	**Conditional Pattern Base**	**Conditional Frequent item set**
LMM	{<LCM, LSH, NMH, NCM, NSH: 1.76> <NMM, LCM, LSH, NCM, NSH:0.855> <LSH, NMH, NCM, NSH: 2.11> <NMM, LSH, NCM, NSH: 0.57> <NMM, LCM, LSH, NSH: 1.315> <NMM, LSH, NSH: 0.515>	< NSH LMM: 10.56 >

	<LSH, NMH, NSH: 1.19> <LCM, LSH, NMH, NSH:1.19> <NMH, NSH: 1.055>}	
NMM	{<LMH, NCM, NSH: 0.57> <LMH, LCM, LSH, NCM, NSH: 1.14> <LCM, LSH, NCM, NSH:1.86> <LMH, LSH, NCM, NSH: 0.8> <LSH, NCM, NSH: 0.7> <LCM, NCM, NSH: 1.060> <LMH, LCM, LSH, NCM: 7.345> <LMH, LCM, NCM, NSH:0.57> <LMH, LCM, NCM: 0.57> <NCM, NSH: 0.285> <LMH, NCM: 0.285> <LMH, LCM, LSH: 0.57> <LCM, LSH, NSH: 1.03> <LMH, NMH, NSH:0.855> <LSH, NSH: 1.015>}	Ø
LMH	{<NMH, NCM, NSH: 0.285 > <NCM, NSH: 0.57> <LSH, NMH, NCM, NSH: 0.57> <LCM, LSH, NCM, NSH: 0.855> <LSH, NCM, NSH: 0.57> <LCM, NMH, NCM, NSH: 0.285> <LCM, LSH, NCM: 1.085> <LCM, NCM, NSH: 1.14> <LCM, NCM: 0.855> <LCM, NMH, NCM: 0.285> <NCM: 0.285> <NMH, NCM: 1.425> <LCM, LSH: 0.8> <NMH, NCM, NSH: 2.335> <NMH, NSH: 1.655> <LCM, NMH, NSH: 0.92>}	<NSH NCM LMH: 0.855>
LCM	{<LSH, NMM, NCM, NSH: 6.272> <LSH, NCM, NSH: 5.418> <NMH, NCM, NSH: 0.57> <NCM, NSH: 1.995> <LSH, NCM: 0.57> <LSH, NMH, NSH: 2.845> <NMH, NSH: 0.855> <NCM:0.57> <NMH, NCM: 0.285> <LSH: 0.57> <LSH, NSH: 1.37>}	Ø
Item	**Conditional Pattern Base**	**Conditional Frequent item set**
LSH	{<NMH, NCM, NSH: 14.05> <NCM, NSH: 2.120> <NCM: 0.57> <LSH:0.57> <NSH: 1.37> <NMH, NSH: 2.845>}	<NMH NCM NSH: 14.05>

NMH	{<NCM, NSH:15.21> <NCM: 0.855> <NSH: 5.525>}	<NCM NSH NMH: 15.21>
NCM	{<NSH: 21.105>	<NSH NCM: 21.105>
NSH	{Ø}	Ø

Finally, the frequent fuzzy item set can be generated by the recursive approach of FP Tree growth. Here intersection operation can be performed for finding the minimum item-set from the conditional base pattern tree as shown in table 8.

GENERATING FUZZY ASSOCIATION RULE

Generate the Association rule from frequent item-set with the support and confidence. From the 30 instances of transaction data of student skill analysis, the frequent item can be produced as in table 5.8. For rule generation, one of the rules of the frequent item-set is placed as a consequent and the rest of the items are placed as antecedent in association rule. Then the confidence value is determined by the equation 5.3.

$$Sup(A \to B) = \sum_{x,y \in N} \min(A(x)B(y))$$

$$conf\,(A \to B) = \frac{\sum_{x,y \in N} \min(A(x)B(y))}{\sum_{x \in N} A(x)} \qquad (5.3)$$

Let us consider, the frequent item-set <NSH NCM LMH: 0.855> where the support of this association is 3.115. The candidate rules are NSH NCM ➔LMH, NSH LMH→NCM and LMH NCM→NSH. The confidence of NSH NCM → LMH is

$$\frac{\sup port(NSH \cup NCM \cup LMH)}{\sup port(NSHNCM)} *100\% = \frac{0.855}{6.61} = 0.13 = 13\%$$

and similarly, to find confident of all frequent item-set as shown in table 9.

Table 9 Experiment Result

SI.No.	Generate Fuzzy Association Rules		Confidence %
	A(x)	B(y)	
1	NSH, LSH	NMH	51.3
2	NSH	LSH	56.5
3	LCM	LSH	57.1
4	LCH	NSH	57.7
5	NSH	LSH	58.5
6	LCM	NSH	60.7
7	LCH	NCM	61.5
SI.No.	**Generate Fuzzy Association Rules**		**Confidence %**
	A(x)	**B(y)**	
8	LCM	NCM	64.3
9	LCH	LSH	65.4
10	LSH	NSH	62.9
11	LSH	NSH	74.1

12	NMH	LSH	65.9
13	LSL	NCM	77.8
14	LCM	NCM	78.8
15	NMH	NSH	82.9
16	NMH	NCM	83.3
17	LMH	NCM	84.6
18	NMM	NCM	100
19	NSM	NCM	100
20	NCH	LSH	100

From this experiment, the result of rule generation of the given transaction of 1120 tuples produced fuzzy association rule from frequent item-set in table 9, illustrates the rule generation of frequent item set and its confident level is measured by the support of association of items evolved in the pattern. From this analysis, by assuming the confident level is 0.5, 20 association rule can be generated with respect of the support count 0.23. The table 5.9, the rule generation of NMH→ NSH shows high confident value of 82.9%. The count of a fuzzy item set obtained by a fuzzy intersection (minimum) operator can be easily achieved without scanning of the database and analyzing the rule generation from the example transaction by given the support count, the frequent pattern item-set can be found efficiently with the confident value of 50% to100%.

The rule of NSH→NMH indicates that if the student attained high in simple question of Numerical ability, male or female poses high in moderate question of Numerical and the possibility is 82.9%. The rule of NMH→NSH indicates that if the student attained high in numerical moderate question, the student of male or female poses high in numerical simple question and again the confident value is 82.9%.

Table 10 Rule generation using different size of support count of 1000 transactions

Support Count	**Apriori**	**FP Tree**	**Fuzzy FP Tree**
0.1	502	148	356
0.2	145	38	176
0.3	67	20	55
0.4	34	7	39
0.5	22	4	26

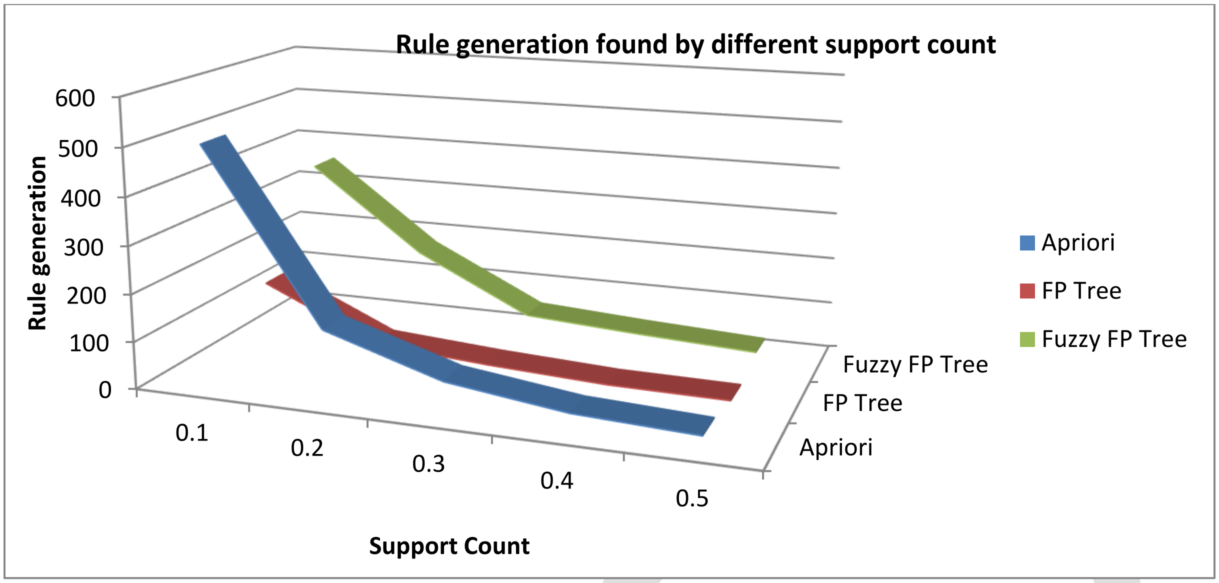

Figure 5.2 Rule generation found by different support count

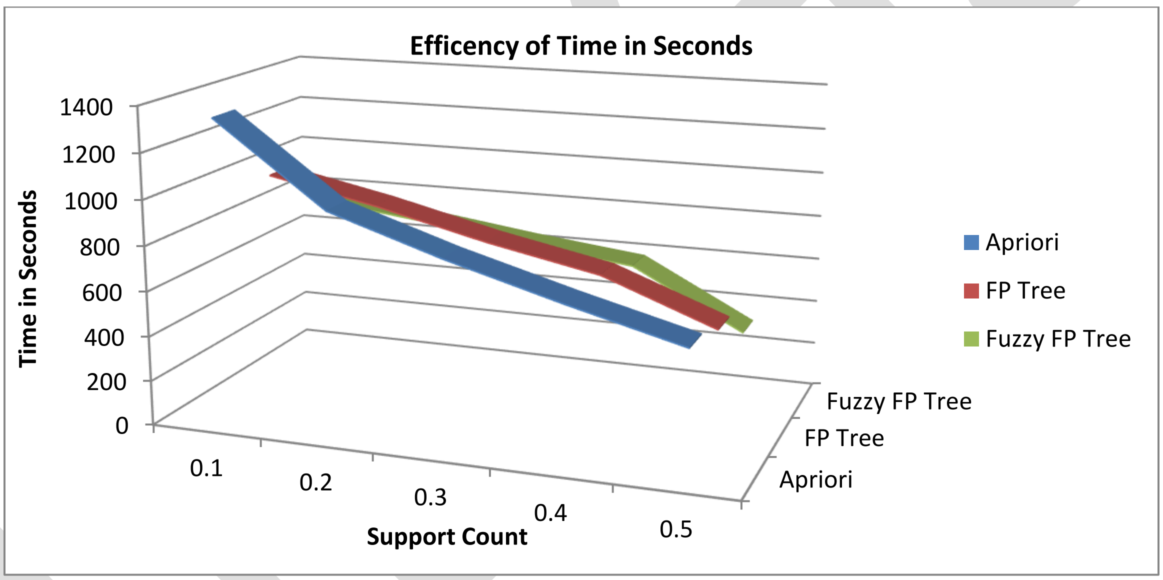

Figure 3 Execution time of rule generation by comparing three algorithms by different support count

Similarly, table 10 represents the rule generation of behavior of student's skill level of simple, moderate and complicated question in numerical and logical reasoning of 1000 training data for analyzing by this association. The number of rules generated in association with frequent pattern mining; the experiment can be performed by using different sizes of support count and analyzed an efficiency of three algorithms. From this analysis, time efficiency and accuracy of rule generation can be experimented. By comparison of (Apriori, FP-Tree and Fuzzy FP Tree growth algorithm) Fuzzy FP-Tree algorithm proved the time efficiency and rule generation is highly more efficient than Apriori, FP-Tree algorithm as shown in Figure 2 and 3.

CONCLUSION

In this paper, it can be concluded that by the comparison of three algorithms (Apriori, FP Tree and Fuzzy FP tree algorithm) obtained the rule generation by given the support of 23% and confident is 50%. A priori produced rule bases by the occurrences of candidate generation and produced more rules. FP tree maintained a classical data base of Boolean format and Fuzzy set theory which handles the quantitative value between the intervals 0 to 1, therefore fuzzy FP Tree growth can combined with fuzzy set theory and FP Growth which deals with quantitative values for each attributes measured in training tuples which helps to speed up the learning phase.

The count of a fuzzy item set obtained by a fuzzy intersection (minimum) operator can be easily achieved without scanning of the database and analyze the rule generation by given different size of support count from 0.1 to 0.5 by the confident level of 0.5.

Finally, Fuzzy FP-Tree algorithm proved the time efficiency and rule generation is highly more efficient than Apriori, FP-Tree algorithm. The frequent pattern mining can be obtained with respect to given numeric quantitative data of 1000 training data as shown in table 10.

REFERENCES:

[1] Jiwei Han, Jian Pei, Yiwen Yen and Runying Mao: "Mining Frequent Patterns without Candidate Generation: A Frequent-Pattern Tree Approach, Data Mining and Knowledge Discovery, 8, 53–87, 2004, 2004 Kluwer Academic Publishers

[2] Takagi T. and M. Sugeno, "Fuzzy identification of system and its applications to modeling And control", Proc. IEEE Trans. on System Man and Cybernetics, Vol. SMC-15, No. 1, pp. 116-132, 1985.

[3] Rakesh Agrawal; Tomasz Imielinski and Arun N. Swami, "Mining Association Rules Between Sets of Items in Large Databases", Proceedings of the 1993 ACM SIGMOD International Conference on Management of Data, pp. 207-216, Washington, D.C., May 1993.

[4] A.H.M. Sajedul Hoque, Rashed Mustafa, Sujit Kumar Mondal and Md. Al-Amin Bhuiyan," A Fuzzy Frequent Pattern-Growth Algorithm For Association Rule Mining" International Journal of Data Mining & Knowledge Management Process (IJDKP) Vol.5, No.5, September 20

[5] H. M. Sajedul Hoque, Sujit Kumar Mondol, Tassnim Manami Zaman, Dr. Paresh Chandra Barman, Dr. Md. Al-Amin Bhuiyan, "Implication of Association Rules Employing FP-Growth Algorithm for Knowledge Discovery", 14th International Conference on Computer and Information Technology 2011 (ICCIT 2011), 22-24 December, Dhaka, Bangladesh.

[6] George J. Klir and Bo Yuan: Fuzzy Sets and Fuzzy Application: Theory and Applications, Prentice Hall of India Private Limited, 2005.

[7] Jiawei Han and Micheline Kamber, Data Mining: Concepts and Techniques, 2nd Ed., Morgan Kaufmann Publishers, 2006.

[8] Hu Y. C,. "Mining association rules at a concept hierarchy using fuzzy partition," Journal of Information Management, Vol. 13, no.3, pp.63-80, 2006.

[9] Pang-Ning Tan, Michael Steinbach, Vipin Kumar, "Introduction to Data Mining", Pearson Education Inc., Fourth Edition, 2009.

[10] Heikki, Mannila, "Data mining: machine learning, statistics, and databases", IEEE, 1996.

[11] Arun K Pujari, "Data mining techniques", University Press (India) Private Limited.

[12] Usama Fayyad, "Data Mining and Knowledge Discovery in Databases: Implications for Scientific Databases" Proceedings of the Ninth International Conference on Scientific and Statistical Database Management IEEE Computer Society Washington, DC, USA, 1997.

MANIFOLD EMBEDDING AND SEMANTIC SEGMENTATION FOR BRAIN TUMOR DETECTION USING HYPERSPECTRAL IMAGING

Sachithra S.S [1], Shiji A.S [2]

PG Student (ME Applied Electronics) [1], Assistant Professor [2]

Department of Electronics and Communication Engineering, Narayanaguru College of Engineering, Manjalumoodu, Tamil Nadu

Abstract—Brain tumor is an abnormal growth of cells, reproducing themselves in an uncontrolled manner. Hyperspectral imaging is an emerging technology that can assist surgeons to classify tumors from healthy tissue in real time. Recent advances in hyperspectral imaging have made it a promising solution for intra operative tissue characterization, with the advantage of being non-contact, non-ionizing and non-invasive. Proposed framework mainly consist of two step namely manifold embedding and semantic segmentation. Manifold embedding is performed by using principal component analysis (PCA), which helps to reduce dimensionality of image. Then semantic segmentation is applied to embedded result by using discrete cosine transform based semantic texton forest (DCT-STF) algorithm. This algorithm has good accuracy for real time application than classical semantic texton forest algorithm.

Keywords— Hyperspectral imaging, Manifold embedding, Semantic segmentation, Brain tumor detection

INTRODUCTION

Brain tumor is generally diagnosed by a specialist called a neurologist. Imaging tests performed on magnetic resonance imaging (MRI) and/or computer tomography (CT) scan utilize computer technique to engender detailed picture of brain. But MRI is still not accessible for real time intra-operative use. Currently patients with brain cancer continue to have very poor survival rates. Surgery is one of the mainstays of treatment, together with radiotherapy and chemotherapy [7]. Since brain tumors diffusely infiltrate into surrounding normal brain tissue, it is extremely difficult for surgeon to accurately differentiate between tumor and normal brain tissue with the nacked eye. In some cases, unintentionally leaving behind tumor tissue after the resection is unavoidable, and in other cases, too much brain tissue is resected in an effort to ensure complete excision. Over segmentation can produce permanent neurological deficits that affect patient quality of life [15]. Therefore surgeons require a real-time method for the localization and assessment of tumor margin during surgery.

Hyperspectral imaging (HSI) is an emerging technology that can assist surgeons to classify tumor from healthy tissue in real time. Hyperspectral imaging is also called image spectroscopy. HSI is spectral imaging collects and process information from across electromagnetic spectrum. Hyperspectral imaging is a non-contact, non-ionizing and minimally invasive sensing technique [9]. Unlike standard red, green and blue (RGB) or spectral images (which have a few more bands than RGB image), hyperspectral images cover a wide range of electromagnetic spectrum and are able to capture a large number of contiguous and narrow spectral bands. This high amount of information conforms the spectral signature which offers the possibility of distinguishing between each type of material or substance presented in the captured scene. Hyperspectral imaging is an emerging modality and promising result have shown with respect to cancer detection. Hyperspectral imaging acquires a three-dimensional dataset called hypercube, with two spatial dimensions and one spectral dimension.

The HSI has a unique feature that it includes numerous bands associated with a single image, so that its resolution will be so high that in accumulate many unique features of the subject. It includes both the spatial and spectral information, since it is a two dimensional spatial images spread out in hundreds of bands of large spectral resolution. Its band not only include just the visible spectrum, but also it includes the ultra violet (UV) and near-infrared (IR) bands. Thus it can be a perfect imaging tool and can well examine all the internal properties of a tissue like emissivity, reflectivity, absorptivity etc which is not possible in conventional imaging techniques. The major advantage of the HSI is that it is fast, cost effective, no radiation effects and no requirement of the contrast agent or it is a completely non-invasive procedure. It is actually an optical spectroscopy technique. It can be applicable for the surgical assistance, especially image guided surgery. Fig 1 shows comparison between hypercube and RGB image.

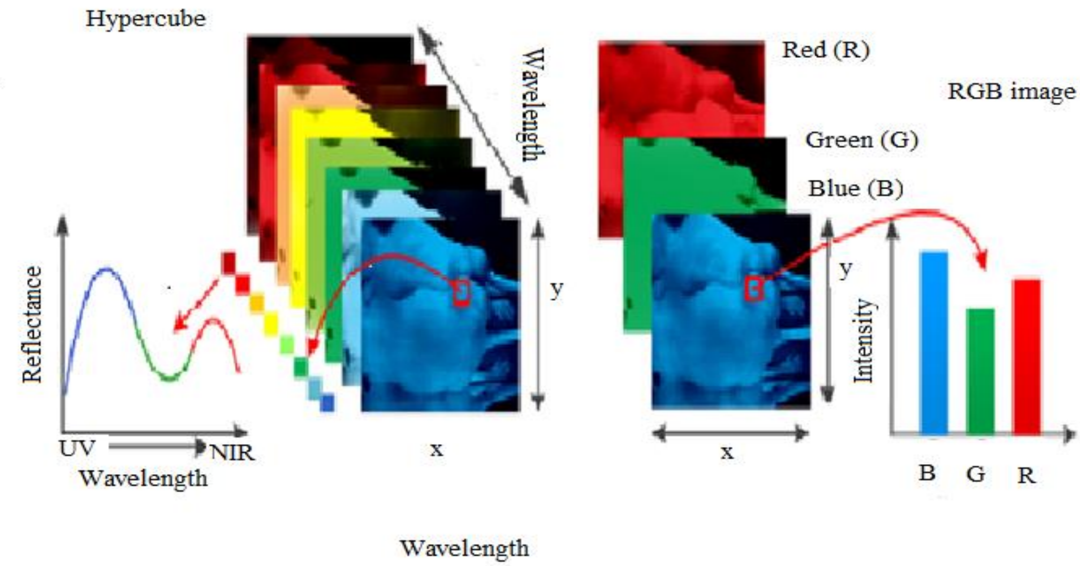

Fig1: Comparison between hypercube and RGB image

In order to obtain the hyperspectral images of in-vivo human brain surface during neurosurgical operations, Hyperspec VNIR A-series and Hyperspec NIR X-series cameras are using. The VNIR (visible and near infrared) camera ranges between 400nm to 1000nm. The near infrared (NIR) camera ranges between 900nm to 1700 nm. Table 1 shows Camera Specifications.

Table 1: Camera Specifications

Camera Specification	Hyperspec VNIR	Hyperspec NIR
Spectral range (nm)	400-1000	900-1700
Spectral resolution (nm)	2-3	5
Slit(µm)	25	25
Spatial bands	1004	320
Spectral bands	826	172
Frame Height (FOV) (nm)	129.21	153.6
Pixel Dimensions (IFOV)	0.1287	0.4800
Max Pixels per Frame	1004	320
Max Frames per pixel (nm)	1825	489
Dispersion per pixel (nm)	0.74	4.8
Detector array	Silicon CCD	InGaAs
Frame rate (fps)	90	100

RELATED WORKS

Existing approaches to brain tumor visualization are commonly based on CT or MRI. The main steps of medical image processing is segmentation, Feature Extraction and Classification. Usha B.L et al. [16] presents K means algorithm for segmentation and gray level statistical analysis (GLCM) for feature extraction. The linear discriminate analysis (LDA) based classification is used for classifying brain tumor of type benign with that of malignant. Anam Mustaqeem et al. [1] presents threshold and watershed segmentation algorithm for brain tumor detection. K.Sathiyasekar et al. [13] presents near infrared imaging technology (IIR) to detect brain tumor of size below 3mm. Fuzzy least mean squares algorithm is used for segmentation purpose. Dina Aboul Dahab et al. [4] presence Probabilistic Neural Network (PNN) classifier for brain tumor detection. Nilesh Bhakarrow Bahadure et al. [10] propose Berkeley Wavelet transform (BWT) and Support Vector machine based (SVM) based classifier for brain tumor detection. Asra Aslam et al. [2] proposes improved edge detection for brain tumor detection. Rajeshwar Nalbalwar et al. [11] proposes Artificial Neural Network (ANN) for finding brain tumor. Hamed Akbari et al. [6] proposes cancer detection using infrared hyperspectral imaging. B. Fei et al.

[5] claimed that hyperspectral imaging is an emerging modality for medical application. David T. Dicker et al. [3] explained the differentiation of normal skin and melanoma using high resolution hyperspectral imaging. Here they experimented the use of high resolution hyperspectral imaging microscopy to detect abnormalities in skin tissue using hematoxylin eosin stained preparations of normal and abnormal skin, benign nevi and melanoma.

PROPOSED WORK

MRI or CT scan is performed on patient before surgical procedure. During each surgical procedure two sterilized fiducial markers are placed in brain. One in area that belongs to a tumor and other in healthy brain tissue. Evaluation of brain tissue is performed by surgeon based on visual appearance. Pointer defines position of fiducial marker with respect to pre-operative MRI or CT data. Afterward hyperspectral image is captured by using hyperspectral camera. After hyperspectal image have been captured, system is moved out of surgical zone and neurosurgeons continues with tumor resection until a new image can be captured depending on nature of surgical procedure

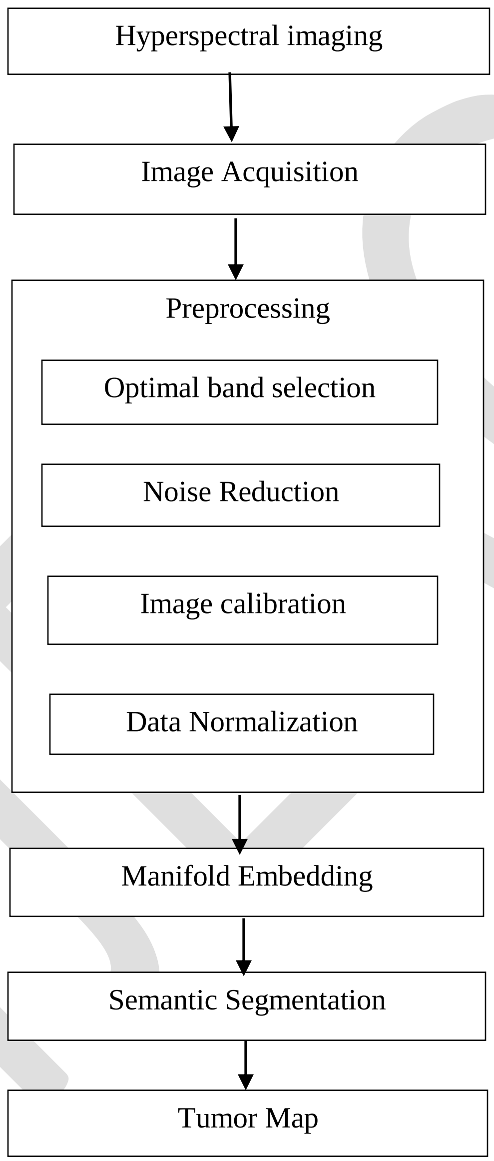

Fig 2: Flow Diagram of Proposed System

The pipeline of the proposed approach is summarized in fig 2. It consist of a hyperspectral image acquisition block followed by a pre-processing step, then manifold embedding and semantic segmentation classifier is performed to generate the tumor map.

IMAGE ACQUISITION

To capture the hyperspectral images, Headwall's VNIR A-Series and Headwall's Hyperspec NIR-X Series cameras have been used. The VNIR camera captures 826 spectral bands and NIR camera captures 172 spectral bands. The spectral range of VNIR camera is 400-1000 nm and for NIR camera is 900-1700 nm. Spectral resolution of VNIR camera is 2-3 nm and for NIR camera is 5 nm. The light source used in this system is a wide spectrum light that provides a uniform illumination on the subject. The distance between the lens and subject is kept constant at 40 cm and manual image focus is used.

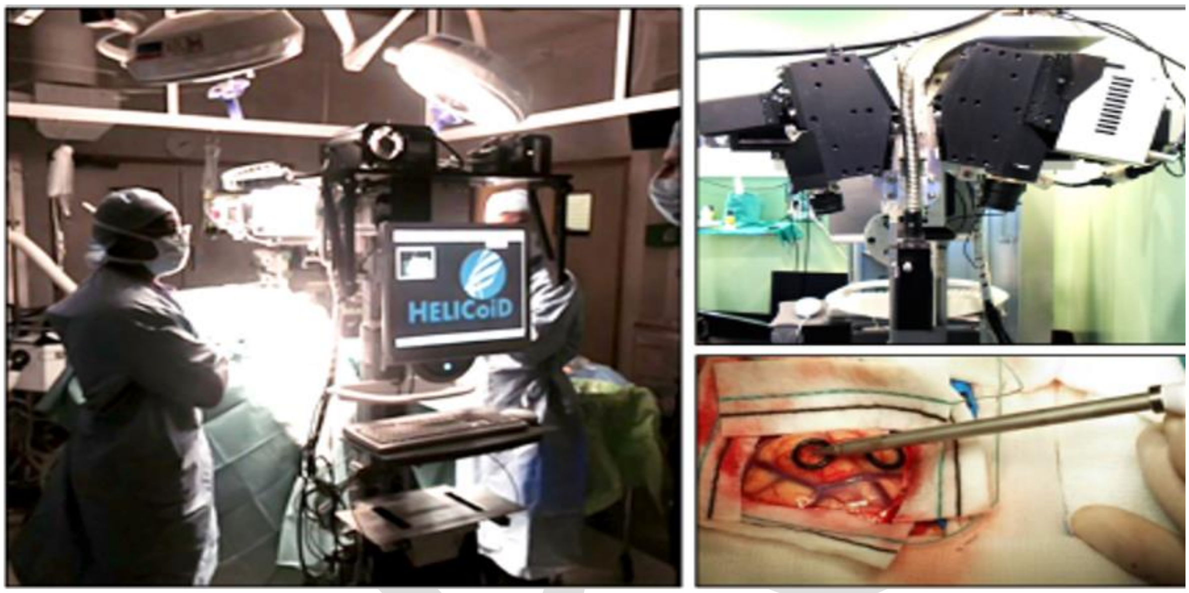

Fig 3: Image acquisition platform

PRE-PROCESSING

During the acquisition of a hyperspectral image the proposed method used a wide spectrum light that provides a uniform illumination. But the light uniformity along all areas of the brain can not always be guaranteed due to the three dimensional cortical folding of the brain that can introduce occlusions and shadows. Other external factors such as inconsistent environment light can lead to variation in spectral domain. These effects can be reduced by using a pre-processing pipeline that normalizes the reflectance of the hyperspectral image. The proposed pipeline is divided into four steps:

1. Optimal band selection
2. Noise Reduction
3. Image Calibration
4. Data Normalization

Optimal band selection

The optimal band selection is one of the important step in hyperspectral imaging processing. Here from the numerous bands available in hyperspectal image only those bands containing the necessary features alone may be considered. This step is used to discard all the distorted bands in the extreme sides. Before the 450 nm and after 950 nm for the visible and near infrared camera and before 950 nm and after 1650 nm for near infrared camera is discarded.

Noise Reduction

The main aim of this step is to remove the noise. Mainly the noise generated by common imperfections of the charge coupled devices (CCD) cells of the hyperspectral camera sensor is removed during this step. The noise removal is obtained by using the Hyperspectral Signal Identification by Minimum Error (HySIME) algorithm by assuming that the reflectance at a given band is well modelled by linear regression.

Image Calibration

During this step variation caused by non uniform illumination over surface of captured scene are adjusted. The hyperspectral image is calibrated using white and dark reference images. These reference images are acquired separately inside the operating theatre before the procedure. The white reference image is obtained from a standard white tile; the dark reference image is obtained by keeping camera shutter closed. The calibration is performed pixel wise.

Data Normalization

Due to scanning procedure of hyperspectral camera and non uniformity of brain surface, some areas of image can be captured with a different illumination. Inorder to avoid this issue, a unit magnitude normalization of brightness is performed for each pixel.

MANIFOLD EMBEDDING

Hyperspectral images have high dimensionality. It make real time processing difficult. High dimensionality is due to large number of wavelength bands that create the hypercube. For example an image that has 400×400 pixels captured at 200 wavelengths will be represented by 160000 vectors lying in the space. In order to handle a hyperspectral image adequately for real-time applications, its dimensionality needs to be reduced through the projection of the hyperspectral cube to a space with only a few dimensions. Dimensionality reduction transforms high dimensional data into a reduced dimensional representation that is still capable of describing the initial data. Principal component analysis (PCA) method [8] is used in this proposed method to reduce dimensionality. The fig 4(a) represents the hyperspectral brain image captured by using VNIR camera. The rings in the image are sterilized fiducial markers placed by doctors during surgical procedure. The fig 4(b) represents manifold embedded hyperspectral brain image. It represents one band representation of fig 4(a).

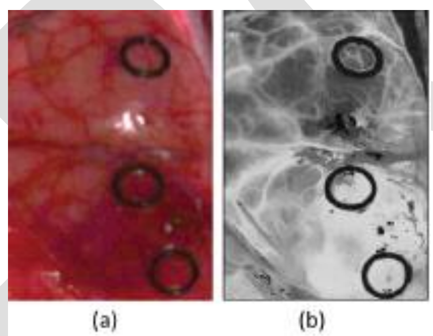

Fig 4: (a) Hyperspectral brain image (b) Embedded image

SEMANTIC SEGMENTATION

To obtain tumor classification map, a semantic segmentation approach is performed on the obtained embedded result. Color based segmentation is known as semantic segmentation. Semantic segmentation describes the task of partitioning an image into regions that delineate meaningful objects and labeling those regions with an object category label. One of the popular approach for this task is based on random forest and is called semantic texton forest (STF) [14] .This algorithm tries to exploit spatial arrangement of low level features to increase object discrimination. The proposed frame work uses discreate cosine transform based semantic texton forest algorithm (DCT-STF). This algorithm combine color and texture information for semantic segmentation purpose. DCT-STF [12] has better performance and less complexity than classical STF.

EXPERIMENTS AND RESULTS

The proposed system was implemented by using Matrix Laboratory (MATLAB) software. MATLAB is high level technical computing language. MATLAB is the interactive environment for algorithm development, data visualization, data analysis and numerical computation.
Hyperspectral brain image captured during surgery of brain tumor is used as input image. The image captured by using VNIR camera is shown in fig 5.

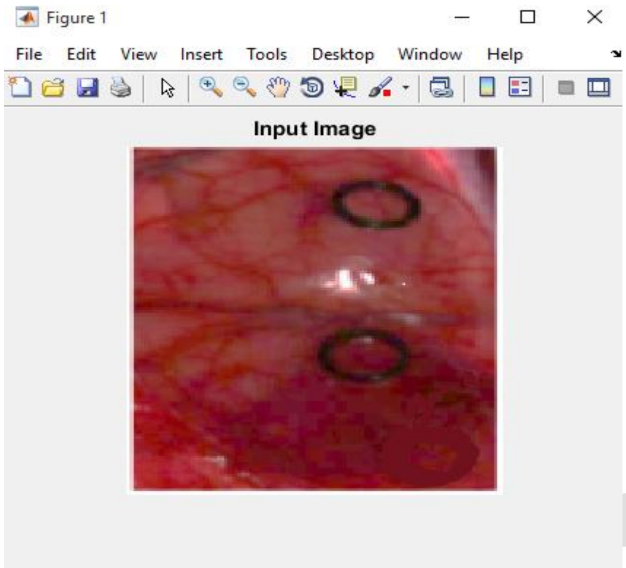

Fig 5: Input Image

After image acquisition and pre-processing, the dimensionality of image is reduced by using manifold embedding. Principal component analysis technique is used to reduce dimensionality of image. Fig 6 shows the embedded output

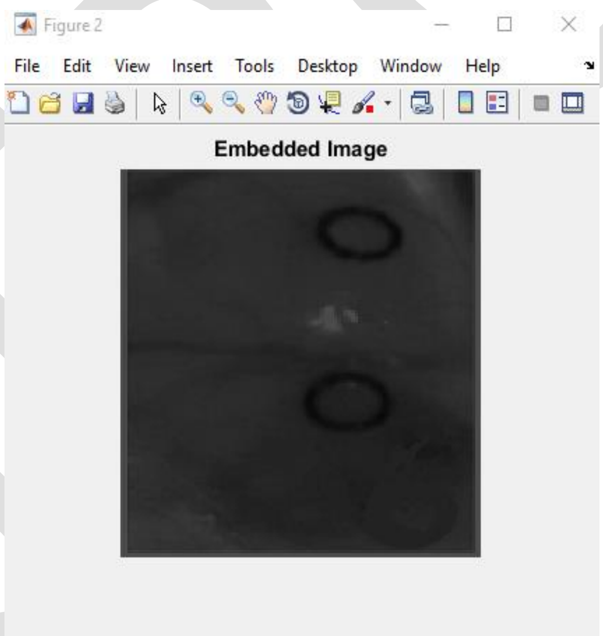

Fig 6: Embedded Output

Semantic segmentation is performed on the embedded result to obtain the tumor map. Color based segmentation is known as semantic segmentation. The discrete cosine transform based semantic texton forest algorithm is used for segmentation.

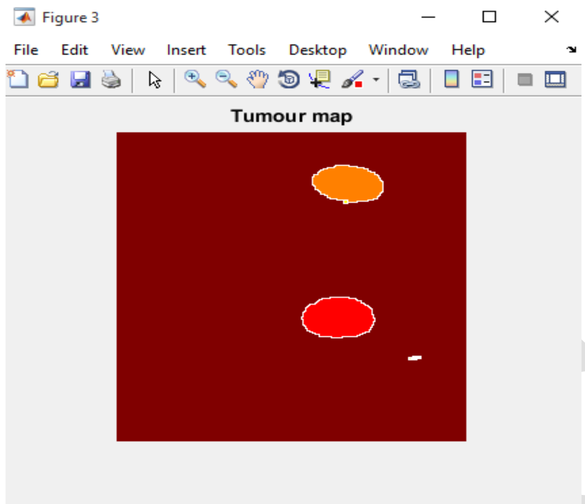

Fig 7: Tumor Map

The fig 7 shows tumor map. In this fig tumor cells are appeared in red color, normal cells are appeared in orange color and brown color indicate background.

Table 2: Computational time of proposed system for VNIR and NIR camera images

Camera Type	VNIR	NIR
Processing time	22 s	5 s
Manifold embedding time	2 s	2 s
Semantic segmentation time	16 s	5 s
Total processing time	40 s	12 s

The table2 shows time needed to process VNIR and NIR camera images. The brain image captured by NIR camera needs less processing time than VNIR camera image.

Mean class accuracy is obtained by averaging the accuracies achieved in each of the classes. Mean class accuracy is more reliable measure than overall accuracy. The mean class accuracy of discrete cosine transform based semantic texton forest algorithm is 80%.

CONCLUSION

The proposed frame work helps for real time cancer detection. The high dimensionality of hyperspectral image is reduced by using Principal component analysis (PCA) method. Then semantic segmentation is performed by using discrete cosine transform based semantic texton forest (DCT-STF) algorithm. The proposed method helps to determine the boundaries of tumors. The proposed method helps to allowing a complete resection of malignant cells at the time of brain tumor operation. The main weakness of the traditional approach are two fold. Firstly it is invasive with many potential side effects and complications and secondly diagnostic information is not available in real time and requires off-line histopathology sample analysis. The proposed system can overcome these problems and tumor resection can be greatly improved during surgical procedures, thus reducing the risk of disease recurrence. The real time nature of techniques improves surgical accuracy. Moreover proposed system helps in understanding cancer progression. Strength of proposed framework is in terms of processing speed and accuracy.

REFERENCES:

[1] Anam Mustaqeem, Ali Javed, Tehseen Fatima "An efficient brain tumor detection algorithm using watershed and Threshold based segmentation",
J.J Image Graphics and signal processing pp 34-39, 2012

[2] Arsa Aslam, Ekram Khan, M.M Sufyan Beg "Improved edge detection algorithm for brain tumor segmentation" Science Direct, Procedia Computer Science pp: 430-437, 2015

[3] D T Dicker, Lerner J, Van Belle P, Barth S F, Guerry D, Herlyn . M, Elder D E, EI-Deiry W S "Differentiation of normal skin and melanoma Using high resolution hyperspectral imaging cancer Biol. Therapy Vol5, no8 pp 1033-1038, 2006

[4] Dina Abool Dahab, Samy SA Ghoniemy, Gamel M Selim, "Automated Brain Tumor detection and identification using image processing and Probabilistic neural network techniques" International journal of image processing and visual communication, 2012

[5] B.Fei, G Lu, R Pike, D Wang, G Chen "WE-D-9A-05: Medical hyperspectral imaging for the detection of head and neck cancer in animal Models" Med, Phys; Vol 41, no6, pp: 500-501, 2014

[6] Hamid Akbari, Luma V Halig, David M Schuster Baoweri Fei, "Hyperspectral imaging and quantitative analysis for prostate cancer detection" J.Biomed opt vol 17 no 7, July 2012

[7] "Improving outcomes for people with brain and other CNS tumors" National collaborating centre for cancer

[8] I. Jolliffe, "Principal Component analysis" wiley online library, 2002

[9] G Lu and B.Fei, "Medical hyperspectral imaging: a review" Journal of biomedical optics, vol 19, no: 1, pp 010901-010901, 2014

[10] Nilesh Bhaskarro Bahadure, Arun kumar Ray and Har pal Thethi "Image analysis for MRI based brain tumor detection and feature extraction Using biologically inspired BWT&SVM" International journal of Biomedical imaging, 2017

[11] Rajeshwar Nalbalwar, Umakant Majhi, Raj patil, Prof. Sudhavshu George " Detection of brain tumor by using ANN" International journal of Research in advent technology vol no 4, pp: 279- 282, 2014

[12] D.Ravi , M.Bober, G.Farinella, M.Guarnera and S.Battiato "Semantic segmentation of image exploiting DCT based features and random forest"
Pattern Recognition, Vol. 52 pp 260-273, 2016

[13] K. Sathiyasekar, N.Rajavinu, A.Prabha and C Jayalakshmi "Analysis of brain tumor detection using intelligent techniques", IJCTA, 9(5), pp:311-
320, 2016

[14] J Shotton, M Johnson and R.Cipolla "Semantic texton forest for image categorization and segmentation" in computer vision and pattern Recognition, CVPR ,IEEE conference, pp: 1-8, 2008

[15] Stummer W, John J.C, Medhron, Nestler U, Franz K, Goetzc, Bink A, Pichlmeier U "Counter balancing risks and gains from extended resections
In malignant giloma surgery: A supplemental: A supplemental analysis from the randomized 5-aminolevulinic acid giloma resection study: Clinical Article J Neurosurgy 114, pp: 613-623, 2011

[16] Usha B.L, Supreeth H.S.G "Brain tumor detection and identification in brain MRI using supervised learning: A LDA based classification method"
IRJET, volume 4, Issue 06, pp 292-294, 2017

A 3D RECONSTRUCTION AND MONITORING TECHNIQUE FOR COMPUTERIZED DERMOSCOPIC SKIN LESION CLASSIFICATION

Anuja C.G[1], Anand J Dhas[2]

[1]PG Student-M.E.Applied Electronics, [2]Assistant Professor

Department of Electronics and Communication Engineering, Narayanaguru College of Engineering Manjalumoodu, TamilNadu

Abstract— This paper highlights a non-invasive 3D reconstruction and monitoring technique for early detection of melanoma. Melanoma is life threating when it grows beyond the dermis of skin. Hence, depth is an important factor to diagnose melanoma. The computer aided monitoring system empowers and motivates the user to actively manage their skin health status by collecting, processing and store information of skin lesion through classifications. In this paper introduces a 3D segmentation method, which is an energy minimization based method designed to segment individual objects in 3D satisfying certain size and shape properties. Different feature set combination is considered and performance is evaluated. Experimental results prove that the proposed computerized dermoscopic system is efficient and can be used to diagnose varied skin lesions.

Keywords— 3D lesion reconstruction, 3D features and tumor depth estimation, 3D segmentation, skin lesions, melanoma, Bag of Features, Adaboost algorithm, Support Vector Machine.

INTRODUCTION

The world health organization reports a rapid increase of skin cancer cases [20]. Skin cancer can be broadly classified as melanoma and non-melanoma type. About two to three million cases of non-melanoma cancer and 132,000 melanoma cancers are reported annually worldwide [5]. The computer aided diagnostic systems are also referred to as ``Computerized dermoscopy". Computerized dermoscopy systems primarily constituted of five components A) Dermoscopy image acquisition of skin lesions, B) Region of interest identification or segmentation of skin lesion, C) Feature Extraction D) Feature selection and E) Decision making mechanisms achieved through machine learning techniques. Numerous studies published lay emphasis on the segmentation or region of interest identification.Digital image processing plays a vital role in the area of research and has opened a wide range of new research prospects. Image processing is a profound key that can modify the outlook of many designs and proposals. Digital image processing refers to the automatic processing of digital image by means of digital computer. The basic steps involved in image processing are image acquisition, pre-processing, segmentation, enhancement of image, image compression, and restoration. In this, image segmentation has become a very significant task in today's scenario [14]. Segmentation is usually the primary step in any computer aided analysis of images. The segmentation process converts an image into more easy and meaningful way to analyze. It is typically used to extract boundaries and curves in the images. Application areas of segmentation includes content based image retrieval, locating, biometric recognition, detection of tumors, tissues in medical field.

Melanoma is typically a type of skin cancer. Of all types of skin cancer known, melanoma is the deadliest type and the highest mortality rates are reported from patients suffering from melanoma. Melanoma cancer occurrences are predominantly reported in the skin but occurrences in the eyes, nasal passages, throat, brain etc. are also known. In the research presented here melanoma cancer of the skin is considered. To diagnose melanoma of the skin a physical examination by a dermatologist and a biopsy is generally carried out. Post confirmation, the doctors proceed to identify the stage of the melanoma skin cancer to initiate the relevant treatment.Stages of melanoma are described through various scales like Clarke scale, Breslow scale, Tumor Node and Metastases (*TNM*) scales. The Clarke and Breslow scale basically define the measure of the depth of the tumor i.e. how deep the tumor has gone into the skin. A normal skin anatomy is shown in Fig.1 (a). The T stages of melanoma defined by Cancer Research UK [7] to measure type and size of tumor.

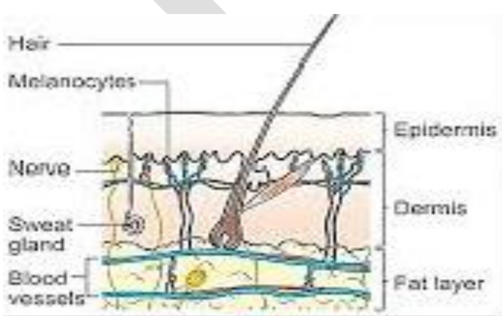

Fig 1(a)

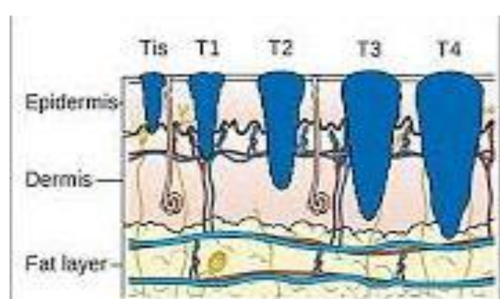

Fig1(b)

FIGURE 1. Anatomy of the skin (a) and T Stages of melanoma (b). Based on the depth of the primary tumor the stage of melanoma is identified. (Note: Depth and dimension of tumor may vary from case to case. Figure only intends to highlight the significance of tumor depth in melanoma diagnosis) (Source: Cancer Research UK).

"Tis" represents an initial stage of melanoma and the tumor is on the epidermis (i.e. top layer of the skin).The primary tumor T1 is of depth is less than 1 mm and is still in the epidermis. Primary tumor T2 has grown into the dermis of the skin and its depth ranges from 1mm to 2mm. Size of the tumor is T3 if its measured depth is 2mm to 4 mm thick and is still localized to the dermis. When the growth depth of a primary tumor is greater than 4mm and is beyond the dermis then it is said to be of T4 size. Based on how far the cancer is spread and the size of the tumor melanoma cancer is classified into five stages[7].

***Stage 0**:* It is the initial stage referred as in-situ melanoma. Occurrences of abnormal melanocytes are observed in the top layer of the skin. Melanoma detected in this stage is 100% curable.

***Stage 1**:* The tumor in this stage has spread into the skin but limited to the epidermis layer. No spread into the lymph or other parts of the body are detected. The tumor growth depth is between 1mm to 2mm and can exhibit ulceration (i.e. breakage of the skin). At this stage through surgical procedures the patients can be cured.

Stage 2: Melanoma tumor is 2mm to 4mm in size and can exhibit ulceration. No spread to lymph nodes or other parts of the body. Cure is possible through surgical procedures.

Stage 3: Tumor is more than 4mm deep and can exhibit ulceration. Cancer is spread to the lymph nodes but is still localized. Advance surgery and post-surgical care required. Survival rate is less.

Stage 4: The tumor is more than 4mm deep and has spread to other organs and lymph nodes. Treatment at this stage is expensive and life threatening as the cancer has spread from its primary tumor site. Low survival rates amongst patients.

Based on the above discussion it is clear that the depth of the tumor is a critical parameter for diagnosis and identification of the cancer stage. Early detection of melanoma (Stage 0 and Stage 1) is the solution to reduce mortality rates amongst patients suffering from melanoma skin cancer. This computerized dermoscopy system to aid early detection of melanoma is presented considering the 3D reconstruction of the lesion. The 3D reconstruction enables to estimate the relative depth of the primary tumor.

A non-invasive computerized dermoscopy system to aid diagnosis of skin lesions is proposed method. A 3D segmentation of the 2D dermoscopic skin lesion images. To reconstruct the 3D skin lesion initially a depth map is derived from the 2D dermoscopic image. The depth map data is fit to the 2D surface to achieve 3D skin lesion reconstruction. The 3D skin lesion is represented as structure tensors. Using the 2D skin lesion data colour, texture and 2D shape features are extracted. The 3D reconstructed skin lesion data issued to obtain the 3D shape features. The 3D shape features encompass the relative depth features estimated. To highlight and study the significance of the features, feature selection methods are considered. For decision making, three different multiclass classifiers have been considered and their performance is compared and studied. The proposed computerized dermoscopy system relies on bag-of-features (BoF), AdaBoost and Support Vector Machine (SVM) for decision making[18]. The patient monitoring is done by sending the output dermoscopic images to the doctor's mail and thereby real time monitoring of patient can be done accurately and can prevent form death of the patient.

RELATED WORKS

A Multi Parameter Extraction and Classification System(MPECS) is proposed to detect early melanoma[12].A six phase approach is[11]adopted to extract the colour,texture and shape features. Classification of three skin lesion types, namely "Advanced Melanoma","Non-Melanoma,"Early Melanoma" is achieved and not explained about the accurate depth of the tumor.into benign or malignant types. The use of classical clinical algorithms such as ABCD (Asymmetry, Border, Color and Diameter) [8], ABCDE(Asymmetry, Border, Color, Diameter and Evolution) [9],Menzies method [10] and the seven-point checklist [11] is adopted by for the diagnosis of melanoma skin lesions. An improvement of 5_30% is achieved by using dermoscopy and classical clinical algorithms when compared to the examination carried out by the naked human eye [12]. The skill of the dermatologists is also critical to achieve accurate diagnostic performance considering dermoscopy images [13], [14].Considering the varied type of melanoma, non-melanoma skin lesions and dependency on the skill level of dermatologist, accurate diagnosis of melanoma is still a problem.

A. Saéz et al. [19] consider that each dermoscopic image represents a Markov model. The parameters estimatedfrom the model are considered as the features of the skin lesion. Classification is performed to identify the globular,reticular and homogeneous patterns in the pigmented cell. Saéz et al. [19] have obtained the dermoscopic images from Interactive Atlas of Dermoscopy [4].Based on high-level intuitive features (*HLIF*) and *SVM* classifiers the diagnosis of melanomas and non-melanoma skin lesions is presented in [4]. In addition to the *HILF* features, low-level features and their combinations are also considered. In [2] a novel equation to compute the exposure time forskin to burn is introduced A threshold based segmentation,hair detection and removal techniques is considered as the pre-processing steps in the image analysis module. Shape, color and texture features are extracted to define the skin lesion images. A two level *SVM* classifier is used to identify the benign, atypical and melanoma moles from the *PH*2 dataset [18]. The importance of considering global and local features in computer aided diagnosis methods is discussed in [7]. Use of color and texture features (global and local) to identify melanoma and non-melanoma images from the *PH*2 dataset is presented. The use of, *SVM*, AdaBoost and BoF classifiers adopted for decision making. Based on the related works reviewed it is observed that limited work is carried out considering 3D reconstruction, depth estimation and 3D shape features of skin lesions which is critical to diagnose melanoma skin cancer. The state of art works carried out so far predominantly consider only binary decision making mechanisms. In thispaper, considers a 3D reconstruction of skin lesion images to estimate depth of the tumour and adopt multiclass decision making mechanisms.

PROPOSED WORK

The proposed computerized dermoscopy system is to aid early detection of melanoma, additionally, the proposed system can also be adopted to diagnose different skin lesions types and the monitoring of patient done by sending the dermoscopic image to the doctor for verification thereby the patient take treatments early as possible. The dermoscopic image dataset is considered to consist of training and testing data. Segmentation is performed obtain the region of interest or skin lesion to be diagnosed. A depth map is extracted from the 2D dermoscopic image. Depth map is used in constructing a 3D model corresponding to the dermoscopic image. The 3D model is represented as a structure tensor. A comprehensive feature set considering the 2D shape, 3D shape, color and texture are extracted per image. A feature selection method to understand the significance of features extracted on decision making is incorporated. For decision making, most of the related works consider binary classification mechanisms. The proposed system considers a multiclass classification mechanisms for decision making, enabling its applicability to diagnose a wide variety of skin lesion images.The computer-aided monitoring system that empowers and motivates the users to actively manage their own skin health status by collecting, processing and store information of skin lesions through its automatic classification. This solution is not intended to perform a skin cancer diagnosis, but rather alert the users to the presence of risk signs and take them earlier to the doctor.Dermoscopic images used for evaluation are obtained from CDROM of Dermoscopy and PH2 dataset.

PROBLEM FORMULATION

Let $I=\{I_0,I_1\ldots.I_n\}$ represent a set of n dermoscopic images. Let $C=\{C_0,C_1\ldots C_m\}$represent a set of classes of the dermoscopic The set I consists of images used for training and testing. Each image I_n is represented by a feature set F_n. The training data is represented as $R=\{(F_1,C_2),(F_2,C_2)\ldots(F_r,C_r)\}$

Similarly the testing data vector can be as $T=\{(F_1,C_1),(F_2,C_2)\ldots.(F_t,C_t)\}$Ct represent the unknown classes and F_t represent a set of features extracted from the images whose class is to be identified. Let D represents the decision making mechanism such that $D(F_r)=C_r$. The goal of proposed system is $D(F_t)=C_t$ i.e. features of image can be need to diagnosed.

3D SEGMENTATION

Image segmentation is a fundamental problem in computer vision and most of the statistical analysis in several applications. For example identification of cells in microscopy images is one of the major challenges in computational biology. Single-cell analysis of brain cells, bacteria or tumors leads to a better understanding of fundamental biological processes and to a more precise treatment of diseases. A variety of methods were proposed to segment cells in tissue sections and cell cultures and several software packages utilize these results for further statistical analysis. Recent studies in biotechnology show that cells cultured in a 3-dimensional microenvironment mimic disease physiology more precisely than those cultured in 2-dimension[2]. To study cell-cell interactions and create predictive models, different cell types are often mixed and 3-dimensional co-cultures and organoids are grown. The segmentation of such mixed 3D cell populations at the single-cell level is a great challenge, especially when their morphology shows high diversity. Although recent advances in light microscopy and assay preparation where made possible to successfully use these models for drug development and clinical applications, there is a great need for advanced segmentation methods to most precisely and cost effectivelyanalyze these large-scale (often 10-100 TB) image data sets.

3D LESION SURFACE RECONSTRUCTION

3D reconstruction is essential to estimate depth of the skinlesions. Techniques like stereo vision, structure from motion, depth from focus, depth from defocus etc. are used to estimate depth considering multiple images. Using constrained image acquisition techniques like active illumination and coded aperture method's, depth can be estimated using single images. The varying or unknown dermoscopic data acquisition parameters/settings used and the non-availability of multiple images render these mechanisms ineffective. In [20] a novel technique to estimate depth, considering a single image obtained from unconstrained image data acquisition techniques is described. The proposed computerized dermoscopy system adopts this technique to estimate the depth in dermoscopic images. Depth map obtained is fit to the underling 2D surface to enable 3D surface reconstruction. The 3D surface constructed is represented as structure tensors. The 3D surface reconstruction results considering two melanoma and one blue nevus skin lesion images is shown in Fig.2

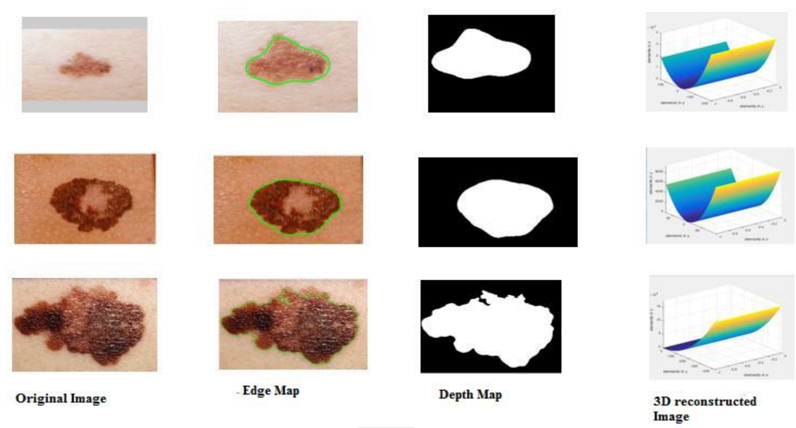

Figure 2: The 3D lesion surface reconstruction technique. The original image is shown in column 1. The edge map used to compute the defocus is shown in column 2. Sparse and the resultant depth map is shown in column 3-4. The structure tensor T representing the 3D lesion surface is shown in the last column.

FEATURE EXTRACTION

Characteristics of the skin lesion images are represented as features. In this paper color, texture, 2D shape and 3D shape features are considered. Accurate and robust feature representation is essential as they directly affect the performance of the skin lesion classification.

COLOR FEATURE EXTRACTION

Color characteristics are often used by dermatologists to classify skin lesions.[7] According to dermatologists,skin lesions are characterized by variegated coloring[10]. The variegated coloring induces high variance in the red, green and blue color space. Red, green and blue component data of the pixels in the segmented skin lesion is stored as vectors. The mean μ and variance σ of each channel is computed. Mean, variance are represented as μ_R,μ_G,μ_B and $\sigma_R,\sigma_G,\sigma_B$ To capture complex non-uniform color distributions within the skin lesion, mean ratios of the mean values is computed.

TEXTURE FEATURE EXTRACTION

To extract the texture features the segmented skin lesion image is converted to grey scale. Haralick-features [20]are adopted to obtain the texture characteristics of the skin lesion. Considering applicability of the proposed computerized dermoscopy system to classify even low quality skin lesion images, Haralick texture features are considered. Texture features are computed using gray-tone spatial-dependence matrices.i.e. $G_s^{[\Theta]}(x,y)$ .The energy feature is computed by using

$$E^{[\Theta]} = \sum_{x,y}^{0} Gs(x,y)^2$$

CLASSIFICATION

Skin lesion classification is the final step of proposed computerized dermoscopy system. In this work presented here, three different classes of classifiers i.e. SVM [8,9], AdaBoost[20]and the recently developed Bag-of-features (BoF)[13,17] classifiers are adopted. The classifiers adopted are also referred to as decision making mechanisms D. Classification broadly involves two phases namely training and testing. In the training phase the classifiers learn from the training set R. Feature properties with respect to the classes are derived in the training phase. In the testing phase we wish to classify test data T. Based on the feature properties observed in training, the decision making mechanisms D classifies a test image represented by feature set Ft as the resultant class Ct . Skin lesion data is complex in nature and cannot be considered as a global model. In the BoF decision making mechanism, skin lesion data is considered as a combination of individual feature models rather than the complete feature set. The BoF classifier exhibits promising results when adopted for complex image analysis. Therefore, the BoF classifier was deemed applicable to solve our skin lesion classification problem. The capability to train a strong classifier from a combination of weak classifiers and appropriate feature selection capabilities exhibited by the AdaBoostalgorithm.SVM classifiers are robust,[9] simple to implement and provide high degree of classification accuracy.Recent works for skin lesion classification[14],[2],[4],[7] prove the ability of SVM classifier for decision making. A Gaussian radial basis function (RBF) kernel is considered in the proposed computerized dermoscopy system. The RBF kernel assists in deriving complex relations between the skin lesion classes and complex nonlinear skin lesion data represented as a feature vector space. A linear kernel is a special case of the RBF kernel, hence SVM classifier is choosen in the proposed method.

EXPERIMENTS AND RESULTS

In this section experimental studies conducted to evaluate the performance of the proposed computerized dermoscopy system [7]. The proposed system was implemented on MATLAB. The dermoscopy data used in the experiments where considering the performance of the three classifiers proposed, comparisons with existing systems and the experiments based on the 3D reconstruction algorithm proposed for depth estimation.

ASSESSMENT OF BoF, AdaBOOST AND SVM CLASSIFIER

The BoF classifier considers a block size of 50 and the number of histogram bins is set to 25. The k-means clustering algorithm is adopted to obtain visual words the KNN employed, considers Euclidean distance and the number of neighbors is set to 10. Inclusion of shape features to color and texture improve performance considering the BoF classifier. Results considering ATLAS dataset show that color and texture information alone considered in D2EX2 is insufficient to classify skin lesions. Considering shape feature improves performance of the BoF classifier observed in D2EX1, D2EX3 and D2EX4.The AdaBoost classifier considered is built using 10 weak classifiers[6]. Number of bins is set to 50. This configuration is established based on a number of iterations to obtain best performance.Results obtained prove that the SVM classifier exhibits better generalization performance on increasing the feature vector when compared to the other classifiers. Observe results of D1EX1, D1EX4 against D1EX2 and D1EX3. A marked performance improvement considering the proposed 3D shape feature inclusion is reported on PH2 dataset. Similar performance improvement is reported considering ATLAS dataset.Sensitivity, specificity and accuracy are described in terms of TP, TN, FN and FP.

True positive (TP) = the number of cases correctly identified as patient

False positive (FP) = the number of cases incorrectly identified as patient

True negative (TN) = the number of cases correctly identified as healthy

False negative (FN) = the number of cases incorrectly identified as healthy

Sensitivity: The sensitivity of a test is its ability to determine the patient cases correctly. To estimate it, we should calculate the proportion of true positive in patient cases. Mathematically, this can be stated as:

Sensitivity = TP/ (TP + FN) = (Number of true positive assessment)/ (Number of all positive assessment)

Specificity: The specificity of a test is its ability to determine the healthy cases correctly. To estimate it, we should calculate the proportion of true negative in healthy cases. Mathematically, this can be stated as:

Specificity = TN/ (TN + FP) = (Number of true negative assessment)/ (Number of all negative assessment)

Accuracy: The accuracy of a test is its ability to differentiate the patient and healthy cases correctly. To estimate the accuracy of a test, we should calculate the proportion of true positive and true negative in all evaluated cases. Mathematically, this can be stated as

Accuracy = (TN + TP)/ (TN+TP+FN+FP) = (Number of correct assessments)/Number of all assessment)

The tradeoff between specificity(SP) and sensitivity(SE) have introduces a cost function C for evaluating the performance.The cost function C is defined as

$$C=\frac{K_{FN}(1-SE)+K_{FP}(1-SP)}{K_{FN}+K_{FP}}$$

Where K_{FN} and K_{FP} are constants and K_{FN} =1.5 x K_{FP}. K_{FN} and K_{FP} represents false negative (FN) and false positive (FP).In the experimental results K_{FN} = 1.5 and K_{FP} =1.0 is considered

Table 1: Experimental result from Adaboost

Exp	SE	SP	C
D1EX1	94%	97%	0.049
D1EX2	96%	98%	0.029
D1EX3	96%	98%	0.028
D1EX4	94%	97%	0.049

Table 2: Experimental result from SVM

Exp	SE	SP	C
D1EX1	80%	97%	0.136
D1EX2	96%	91%	0.448
D1EX3	97%	94%	0.271
D1EX4	98%	99%	0.013

ASSESSMENT OF 3D SKIN LESION RECONSTRUCTION TECHNIQUE

A major goal of the proposed computerized dermoscopy system is to aid early detection of melanoma i.e. in-situ melanoma. Diagnosis can be efficiently achieved using the 3D reconstruction technique proposed. The 3D data / tensor provides useful insight to analyze relative depth of melanoma cancer skin lesions. The International Skin Imaging Collaboration (ISIC):Melanoma Project introduced in recent times, is an academia-industry partnership providing dermoscopic data for melanoma diagnosis [16]. A large number of societies have collaborated together in the ISIC: Melanoma Project.Data provided is by far the most comprehensive set of publicly available melanoma skin lesion images [13]. A total Clinical/ diagnosis data corresponding to each skin lesion image is also available. Though actual depth (currently obtained using invasive biopsy) cannot be computed, accurate estimates can be obtained by using the proposed technique. The relative estimated depth is a critical feature for identification of in-situ melanoma. In addition, 3D features extracted using the 3D reconstructed skin lesion improve overall system classification performance as reported in the previous section.

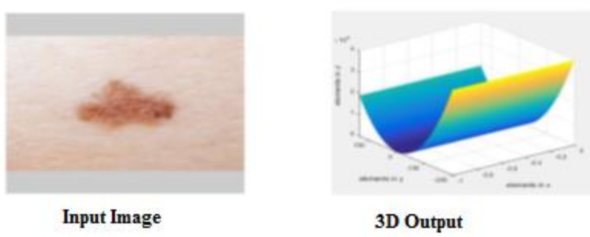

Figure 3: Melanoma follow up image and its estimate depth

From figure 3 the relative depth of the tumor is 0.02mm and the melanoma at this stage is 100% curable. Only occurrence of abnormal melanocytes are observed in the top skin layer. The tumor in this stage has spread into the skin but limited to the epidermis layer. No spread into the lymph or other parts of the body are detected. Dermoscopic images is consider to further assess performance of the proposed 3D reconstruction technique. An in-situ melanoma image and the corresponding relative estimated depth is shown in the figure

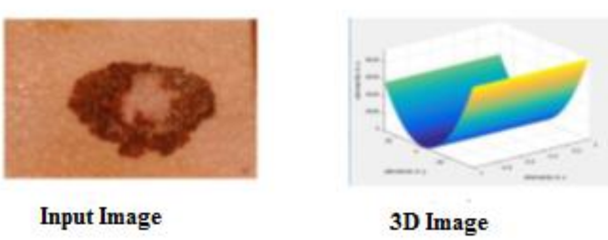

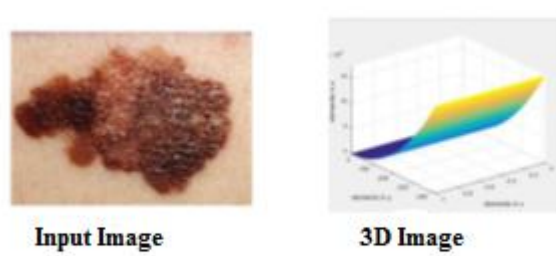

Figure 4: Input melanoma and its 3D reconstructed depth projection

Figure5: Severe melanoma and its 3d projection

At this stage the relative depth of the tumor is in between 0.6mm and can exhibit ulceration and will not spread through any part of the lymph. From figure 5, at this stage the tumour is cure only through surgical measures. The tumour depth is of about 1.5mm in growth and has spread to other organs and lymph nodes, treatment at this stage is expensive and can be removed only through surgical measures hence from the above discussions it is clear that depth is an important parameter for diagnosing and identification of cancer. The input image is send to the doctor then he can continually monitor the patient and can detect the melanoma at its early stage and thereby life threating will not be occurred.

CONCLUSION

Amongst all the skin cancers known, melanoma accounts for the majority of deaths reported. Melanoma is curable if diagnosed early. Use of noninvasive computerized dermoscopy techniques to diagnose skin lesions is commonly adopted. Identifying depth of the melanoma tumor into the skin is essential to ascertain the stage of cancer. Existing computerized dermoscopy techniques lay marginal or no emphasis on depth for diagnosis. Here introduce a computerized dermoscopy system in this method that incorporates depth estimation. A 3D skin lesion reconstruction technique using 2D dermoscopic images is proposed. Segmentation is achieved using the adaptive snake technique. The 3D reconstruction is achieved by fitting the depth map estimated to the underling 2D surface. Color, texture and 2D shape features are extracted. Based on the 3D tensor structure constructed, depth and 3D shape features are extracted. Feature selection to study the effects of features and their combinations on decision making is proposed. For decision making BoF, AdaBoost and SVM classifiers is applied. Experimental study is conducted using the PH2 and ATLAS datasets. Results considering different feature combinations and BoF, AdaBoost, SVM classifiers is presented in this paper. The SVM achieves best classification scores of SE = 96% and SP = 97% on PH2 dataset.The SVM classification score of SE = 98% and SP = 99% on Atlas datasheet. In view of the results, it is concluded that inclusion of 3D shape features proposed (that include the estimated depth features) enhance performance aiding accurate diagnosis of varied skin lesion types. The computer-aided monitoring system that empowers and motivates the users to actively manage their own skin health status by collecting, processing and store information of skin lesions through its automatic classification.The analyzed skin lesion can be submitted on the database as a new checkup of a previously analyzed mole.This way the user is able to compare the results with previous examinations and check if significant changes appeared.

REFERENCES:

[1] American Cancer Society, Cancer Facts&Figures 2015, American Cancer Society, 2015.

[2] O. Abuzaghleh, B. D. Barkana, and M. Faezipour, “Non-invasive real-time automated skin lesion analysis system for melanoma early detection and prevention.” IEEE J.Transl.Eng.Health Med., vol.3, 2015, Art.no.4300212.

[3] J. F. Alcon *et al.*, “Automatic imaging system with decision support for inspection of pigmented skin lesions and melanoma Diagnosis”IEEE J. Sel. Topics Signal Process., vol. 3, no. 1, pp. 14_25, Feb. 2009.

[4] R. Amelard, J. Glaister, A. Wong, and D. A. Clausi, ``High-level intuitive features (HLIFs) for intuitive skin lesion description," IEEE;Trans. Biomed. Eng., vol. 62, no. 3, pp. 820_831, Mar. 2015

[5] L. Baldwin and J. Dunn, ``Global controversies and advances in skin cancer Asian_Pacific J. Cancer Prevention, vol. 14, no. 4, pp.,. 2155_2157, 2013.

[6] C. Barata, M. Ruela, M. Francisco, T. Mendonça, and J. S. Marques, ``Two systems for the detection of melanomas in dermoscopy Images”using texture and color features," *IEEE Syst. J.*, vol. 8, no. 3, pp. 965_979, Sep. 2014.

[7] Cancer Research UK. [Online]. Available: http://www.cancerresearchuk.org/about-cancer/type/melanoma/treatment/stagesof-Melanoma#bres

[8] N. Christianini and J. Shawe-Taylor, An Introduction to Support Vector Machines. Cambridge, U.K.Cambridge Univ. Press 2000

[9] C. W. Cortes and V. Vapnik, ``Support-vector networks," *Mach. Learn.*,vol. 20, no. 3, pp. 273_297, 2000.

[10] F. Ercal, A. Chawla, W. V. Stoecker, H.-C. Lee, and R. H. Moss, “Neural network diagnosis of malignant melanoma from colour Images.”IEEETrans. Biomed. Eng., vol. 41, no. 9, pp. 837_845, Sep. 2010.

[11] R. Fatima, M. Z. A. Khan, A. Govardhan, and K. D. Dhruve,Computer aided multi-parameter extraction system to aid early detection of skin cancer melanoma,Int. J. Comput. Sci. Netw. Secur., vol. 12, no. 10, pp. 74_86, Oct. 2012

[12] R. Fathima, M. Z. A. Khan, A. Govardhan, and K. Dhruve, ``Detecting insitu melanoma using multi parameter extraction and Neural classification mechanisms," Int. J. Comput. Eng. Technol., vol. 4, no. 1, pp. 16_33, 2013.

[13] R. Fergus, P. Perona, and A. Zisserman, ``Object class recognition by unsupervised scale-invariant learning," in Proc. IEEE Int. Confg.Comput.Vis. Pattern Recog., vol. 2. Jun. 2003, pp. II-264_II-271.

[14] R. Garnavi, R. Aldeen, M. J. Bailey, ``Computer-aided diagnosis of melanoma using border- and wavelet-based texture analysis," IEEE Trans.Inf. Technol. Biomed., vol. 16, no. 6, pp. 1239_1252, Nov. 2012.

[15] R. M. Haralick, K. Shanmugam, and I. H. Dinstein, Textural features for image classification,IEEE Trans. Syst., Man, Cyber. syst., vol. 3, no. 6,pp. 610_621, Nov. 2014.

[16] The International Skin Imaging Collaboration: Melanoma Project. ISIC Archive. [Online]. Available: https://isic-archive.com/
[17] T. Leung and J. Malik, ``Representing and recognizing the visual appearance of materials using three-dimensional textons,'' Int.J Comput. Vis.,vol. 43, no. 1, pp. 29_44, Jun. 2001.
[18] T. Mendonça, P. M. Ferreira, J. S. Marques, A. R. S. Marcal, and J. Rozeira, ``PH2-A dermoscopic image database for research and benchmarking,'' in Proc. IEEE Eng. Med. Biol. Soc. 35th Annu. Int. Conf. (EMBC), Jul. 2013, pp. 5437_5440.
[19] A. Saéz, C. Serrano, and B. Acha, ``Model-based classi_cation methods of global patterns in dermoscopic images,'' IEEE Trans. Med .Imag., vol. 33,no. 5, pp. 1137_1147, May 2014.
[20] WHO Intersun, accessed on Jul. 21, 2015. [Online]. Available: http://www.who.int/uv/faq/skincancer/en/index1.html

AUTOMATIC DETECTION OF GLAUCOMA BASED ON CUP - DISK RATIO WITH POLAR SEGMENTATION

Sujithra B S[1], Anand J Dhas [2]

[1]PG Student-M.E Applied Electronics, [2]Assistant Professor

Department of Electronics and Communication Engineering, Narayanaguru College of Engineering, Manjalumoodu, TamilNadu

ABSTRACT —This paper proposes a new method for the detection of glaucoma using fundus image. Glaucoma is a disease related with human eyes. Now-a-days detection of glaucoma is the most important research topic in medical field. It is the second leading cause of blindness in the world and it has no cure. Glaucoma has different types, they are normal tension, open angle, close angle etc. Normal tension affects the vision field and damage the optic nerve as well. The term angle means distance between iris and cornea. If the distance is large then it is referred as open angle glaucoma. Similarly if the distance between iris and cornea is short, that is referred as close angle glaucoma. Close angle glaucoma is very painful and it reduces the vision field of eye very quickly. Currently there are treatments are available to prevent vision loss but the disease must be detected in the early stage. One of the main advantage of this method is its fast processing time and accuracy. The main objective of this project is to develop an automatic detection method of glaucoma in retinal images based on Cup-Disk ratio identification and the methodologies used in this project are optic disc and optic cup localization and segmentation using Circular Hough Transform and Polar Transform.

Keywords— Glaucoma, Retinal image analysis, Optic Disk detection, Hough Transform and ROI calculation, segmentation, CDR (Cup to Disk Ratio) identification, polar transform.

INTRODUCTION

Nobody can imagine that how the world will world if we are losing our eyesight to a silent disease called Glaucoma. It has been nicknamed the "sneak thief of sight" because it often goes undetected and causes irreversible damage to the eye. Glaucoma is the term for a diverse group of eye diseases. Glaucoma is a serious ocular, chronic, irreversible neurodegenerative disease. It is one of the common causes of blindness with about 79 million in the world likely to be afflicted with glaucoma by the year 2020.It is a significant cause of blindness in the world. The incidence of glaucoma increases with age but the disease is more prevalent among individuals with a family history of glaucoma. It can occur at any age and can lead to permanent vision loss and blindness.

Glaucoma produces gradual and progressive visual field loss that results from a progressive loss of optic nerve fibers at the back of the eye. This causes damage to the eye tissues and the optic nerve, which contains more than a million nerve fibers. Optic nerve connects the eye to the brain. This important nerve is responsible for carrying images to the brain. The optic nerve fibers make up a part of the retina that gives us sight. This nerve fiber layer can be damaged when the pressure of the eye (intraocular pressure) becomes too high.

Over time, high pressure causes the nerve fibers to die, resulting in decreased vision. Vision loss and blindness will likely result if glaucoma is left untreated. Glaucoma produces gradual and progressive visual field loss that results from a progressive loss of optic nerve fibers. . If not detected in the early stage, glaucoma can result in partial or total blindness.

Clinically, the disease initially results in peripheral and subsequently central vision loss. There are usually no symptoms in the early stages of the disease. As the disease progresses, vision seems to fluctuate and peripheral vision fails. If left untreated, vision can be reduced to tunnel vision and eventually, total blindness. It is characterized by the progressive degeneration of optic nerve fibers and leads to structural changes of the optic nerve head, which is also referred as optic disk, the nerve fiber layer and a simultaneous functional failure of the visual field. Since, glaucoma is asymptomatic in the early stages and the associated vision loss cannot be restored, its early detection and subsequent treatment is essential to prevent visual damage.

The optic disk (OD) is the location where ganglion cell axons exit the eye to form the optic nerve. There have been efforts to automatically detect glaucoma from 3-D images. However, due to their high cost they are generally unavailable at primary care centers and hence a solution built around these imaging equipment is not appropriate for a large-scale screening program. Glaucoma treatments include medicines, laser trabeculoplasty (draining of fluid), conventional surgery, or a combination of any of these. Although these treatments may help to save remaining vision, they do not improve sight already lost from glaucoma.

Laser trabeculoplasty and conventional surgery also reduce intraocular pressure by draining fluid from the eye. Unfortunately early diagnosis of glaucoma with high specificity and sensitivity using standard clinical diagnostic instrumentation remains problematic. In this project the ratio between optic cup to disk is estimated by using polar segmentation which make use of early diagnosis in glaucoma detection with fast processing time.

II RELATED WORK

Glaucoma is a corporate terminus for a composite radical of circumstances that have reformist ocular pathology ensuing sight loss. Retinal nerve fiber layer defect (NFLD) is one of the most important findings for the diagnosis of glaucoma reported by ophthalmologists. However, such changes could be overlooked, especially in mass screenings, because ophthalmologists have limited time to search for a number of different changes for the diagnosis of various diseases such as diabetes, hypertension and glaucoma [1]. The texture analysis of the retinal nerve fiber layer (RNFL) in color fundus images is a promising tool for early glaucoma diagnosis. The method utilizes Gaussian Markov random fields (GMRF) and the least square error (LSE) estimate for the local RNFL texture modelling [2].

Glaucoma is a disease characterized by elevated intraocular pressure (IOP). This increased IOP leads to damage of optic nerve axons at the back of the eye, with eventual deterioration of vision. CDR is a key indicator for the detection of glaucoma. The ratio of the size of the optic cup to the optic disc, also known as the cup to-disc ratio (CDR), is one of the important clinical indicators of glaucoma, and is currently determined manually by trained ophthalmologists, limiting its potential in mass screening for early detection [3]. An automatic detection method of Glaucoma in retinal images were also developed [4]. The ratio of the optic cup to disc (CDR) in retinal fundus images is one of the primary physiological parameter for the diagnosis of glaucoma. The K-means clustering technique is recursively applied to extract the optic disc and optic cup region and an elliptical fitting technique is applied to find the CDR values. The blood vessels in the optic disc region are detected by using local entropy thresholding approach. The ratio of area of blood vessels in the inferior superior side to area of blood vessels in the nasal-temporal side (ISNT) is combined with the CDR for the classification of fundus image as normal or glaucoma by using K-Nearest neighbour, Support Vector Machine and Bayes classifier [5].

A novel method is proposed for the early detection of glaucoma using a combination of magnitude and phase features from the digital fundus images [6]. The pressure inside the normal eye is below 21mm of Hg. When the pressure inside the eye(s) increases more than 21mm of Hg, the optic nerve is damaged. By measuring the colour pixels in the affected area the observation shows that the person is suffering from Glaucoma or not [7]. Detection of the ratio of optic cup to disk radius is a significant diagnostic task, a major role is being handled by the computer assistance. The optic disk has been found by using red color space image as the optic disk is brighter considering to the other macula region and the contours are identified by means of morphological reconstruction techniques [8].

The major challenge in Retina image analysis is to obtain the boundary and the area mask of cup and disk. Automated detection of cup and disk area demands sophisticated morphological and image processing applications to make the boundary more prominent and hence detectable with higher accuracy [9]. Manual grading and analysis of the RetCam image is subjective and time consuming. A system for intelligent analysis of iridocorneal angle images, which can differentiate closed angle glaucoma from open angle glaucoma automatically [10].

III . PROPOSED METHOD

Early detection of Glaucoma through automated retinal image analysis helps in preventing vision loss. Optic disk (OD) and optic cup (OC) segmentation from retinal images is the preliminary step in developing the diagnostic tool for early Glaucoma detection. The proposed methodology is aimed at contributing to the development of computer assisted system for Glaucoma screening. There are other published methods of OD and OC (Optic Cup) segmentation available in literature but this methodology is computationally fast, produces higher accuracy, robustness and tolerant to vast variety of images which make it suitable for integration with Glaucoma detection system.

Fig 3.1 Retinal fundus image

3.1 PROPOSED METHODOLOGY

This work presents an automated Optic Disc and Optic Cup localization and segmentation technique. For the segmentation of OD boundary, the first step is to approximate the OD center. Optic Disc appears as the brightest spot in the retinal fundus images but the presence of artifacts can create multiple bright spots. Pathologies in fundus images can take shape of OD while actual OD could lose its brightness. The shape of the OD varies from circular to elliptical. This information about the shape of the OD can be used for the detection of OD. The proposed methodology preprocesses the image to remove vessels and enhance the OD boundary using morphological operations. CHT is used for both OC and OD localization. Spatial to polar transform is applied to convert circular region of interest. This polar segmentation uses a novel segmentation algorithm to segment both optic disk and optic cup. Finally ratio between these two are calculated. If the ratio between Optic Cup and Optic Disk is less than 0.3 then the image is not glaucomatous. Otherwise if the ratio between OC to OD is greater than 0.3 then the image is noted as glaucomatous.

3.2 PREPOCESSING

Varying conditions during image capture, noise, uneven illumination and contrast variations are the added challenges of automated optic disc detection and segmentation. In order to handle these images autonomously, preprocessing has to be applied.

3.2.1 Histogram Matching

Histogram matching is the first step in preprocessing stage**.** Histogram matching or histogram specification is the transformation of an image so that its histogram matches a specified histogram. The well-known histogram equalization method is a special case in which the specified histogram is uniformly distributed.

Histogram Matching has been applied to for normalizing the image variations. The histogram of properly illuminated image is taken as reference and the other image's histograms are matched with it which resulted in normalized illumination and color tone. Red channel was chosen as it

3.2.2 Background Normalization

Background normalization is then performed by subtracting the image with the estimate of background. The estimate of background Ibg is calculated by filtering the image with a large arithmetic mean kernel such that the filtered image doesn't contain any visible structures. Original image is also morphologically opened using a 'disk' shaped structuring element with a size 1/100th the size of the original image to obtain I-open. Background normalized image I-normalized is the difference of opened image and the background estimate.

$$I_{normalized} = I_{open} - I_{bg} \qquad (1)$$

3.3 OPTIC DISK LOCALIZATION

OD localization from preprocessed images is done by applying CHT (Circular Hough Transform). This step requires a radius search range of min radius and a max radius. Max and min radius are approximated to be 1/30th to 1/10th of the image width. The output of the transform contains all the circles that are present in the given range. The circle with the highest score is kept.

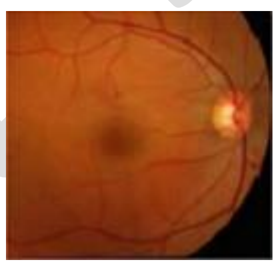

Fig 3.2 OD localization using CHT

3.4 OPTIC DISK AND OPTIC CUP SEGMENTATION

For the precise segmentation of the Optic Disc, a region of interest (ROI) is extracted from the original image ''I_orig''. The size of ''I_roi'' from ''I_orig'' is calculated as described by following equation

$$roisize = r + buff \qquad (2)$$

Where, r is the radius of the circle approximated by the CHT and buff is the number of extra pixels that are not part of the OD. ROI is centered on the circle center approximated by the CHT. ROI contains Optic Disc pixels surrounded by non-OD pixels. The next task is to find precise boundary between OD pixels and non-OD pixels. Direct thresholding techniques does not yield good results as the gray level distribution of the OD and non-OD regions is not uniform and applying a global threshold fails. Applying a local threshold on a neighborhood of pixels also does not return good results because of the circular nature of the OD. To overcome these issues, a novel OD segmentation technique is proposed that makes use of Polar Transform.

Polar transform can be defined as a 2D coordinate system where every point is calculated using distance from a reference point and an angle from a reference direction. Polar transform has been used a lot in automated segmentation of iris from image as is done.

For OD segmentation, the ROI image is calculated and ROI's pixel coordinates are converted from Cartesian to Polar coordinates. The origin point is the center of the ROI image. Due to this transformation, the OD is now straightened. Next this straightened OD is divided in to sub-tiles. Morphological erosion by reconstruction is applied on each tile followed by morphological dilation by reconstruction. At this step, since precise boundary of the Optic Disc is needed, morphological opening and closing is avoided to remove the structures in the retina that are to be used as the end boundary points to distinguish between Optic Disc pixels and the rest of the image. Opening by reconstruction preserves the shape of the components.

After application of opening by reconstruction, each tile is then thresholded using adaptive thresholding. If the output tile is successfully thresholded in to two regions, it is forwarded to the next step as is. If not, then a blank tile (all black) is forwarded. The tiles are then combined and Polar to Cartesian transformation is applied. Similarly, for Optic cup segmentation the same procedure is followed. Ellipse fitting is then performed using ellipse equation in which the boundary obtained via thresholding is used to draw an ellipse over it. This gives the precise OD boundary and the Optic Cup.

3.5 ELLIPSE FITTING

Finally, ellipse fitting is performed by using ellipse equation in which the boundary obtained via thresholding is used to draw an ellipse over it. This gives the precise OD boundary and the Optic Cup of fundus image.

3.6 CLASSIFICATION OF OPTIC DISK PIXELS

	Algorithm predicted pixel $\in$ OD	Algorithm predicted pixel $\notin$ OD
Actual pixel $\in$ OD	True Positive (TP)	False Positive (FP)
Actual pixel $\notin$ OD	False Negative (FN)	True Negative (TN)

IV. EXPERIMENTS AND RESULTS

The methodology is evaluated on publically available datasets of fundus of eye. Among which one input is taken for detecting glaucoma. The following figures gives the description regarding outputs obtained at each stage.

4.1 HISTOGRAM MATCHING

Initially, a reference image is taken for histogram matching. Histogram of input image and the reference image is matched to obtain accurate output.

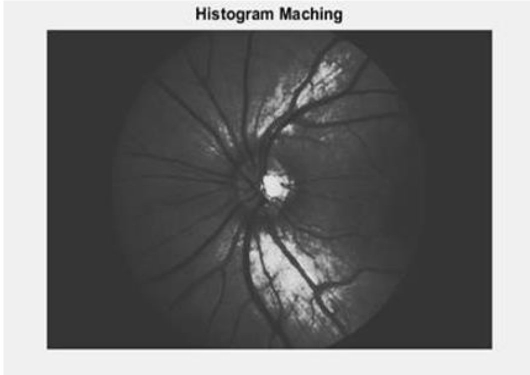

Fig 4.1 Histogram matched output

4.2 BACKGROUND NORMALIZATION

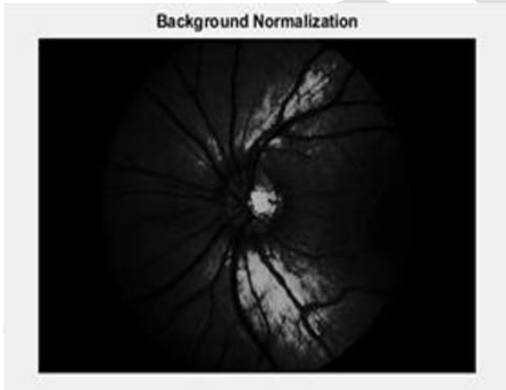

Fig 4.2 Background normalized image

Fig.4.2 gives the background normalized image. By completing this preprocessing stage an output of Background normalization is then performed by subtracting the image with the estimate of background. The estimate of background Ibg is calculated by filtering the image with a large arithmetic mean kernel such that the filtered image doesn't contain any visible structures.

4.3 OUTPUT

The final output of glaucoma detection is shown in figure 4.3. This image provides accurate Optic Disk and Optic Cup and the ratio between these two outputs are taken by using mathematical approach.

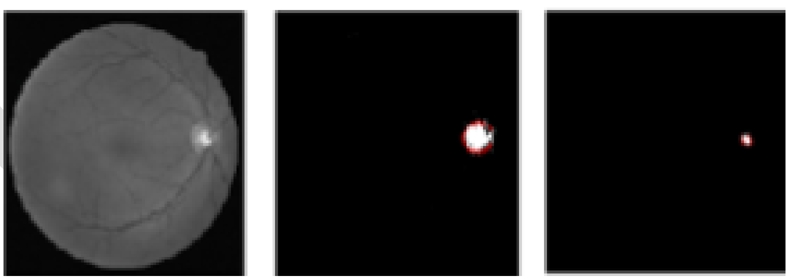

(a) (b) (c)

Fig a) input image b) Optic Cup c) Optic disk

4.4 COMPARISON CHART

The given table 1.1 gives the detailed results of corresponding authors for their experiment with the detection of glaucoma by using various methods. By seeing the table we can understand that the proposed work perfoms in a better way by means of sensitivity , specificity , time and accuracy.

Table 1.1 Comparison with existing methods

Author Name	Sensitivity	Specificity	Accuracy	Time(Sec)
A. Basit and M. M Franz 2015 [1] (Morphological Operations)	0.891	0.991	This parameter is not Considered	This parameter is not Considered
Sopharak and Uyanonvara 2008 [2] (Mathematical Morphology Method)	0.213	0.938	This parameter is not Considered	14.92
M. Abdullah ana M Fraz 2016[21] (Circular Hough Transform and grow – cut Algorithm)	0.812	0.991	0.961	52.2
Karthekeyan Sakthivel and Ragurajan narayanan 2015[10] (Local Binary Pattern and Dugman's Alogorithm)	0.952	0.951	This parameter is not Considered	2.4
Archana Nandibewoor S B Kulkarni 2013 [3] (MATLAB Software tool)	0.962	0.961	0.952	This parameter is not Considered
Niladri Halder1and Diby4endu Roy 2015 [15] (RGB color conversion method)	This parameter is not Considered	This parameter is not Considered	0.901	This parameter is not Considered
Shruti P Y and Sharangouda.N 2015 [16] (Morphological Operations and Hough Transform)	This parameter is not Considered	This parameter is not Considered	0.961	This parameter is not Considered
Proposed Methodology **(Circular Hough Transform and Polar Transform)**	**0.833**	**0.998**	**0.993**	**1.6**

V.CONCLUSION

An advanced technique that identifies the optic cup and optic disk is presented in this paper. It determins the radius by segmenting out the optic cup and optic disk and then calculating the ratio between them in fundus of the macula. The main feature which has been considered here for identifying the vision impaired disease glaucoma is the Cup- to- Disk Ratio (CDR), which specifies the change in the cup area. Increase in the intra ocular pressure (IOP) results in increase in the area of the cup and this results in dramatic visual loss. In this paper increase in cup area is analyzed by examining the CDR value. The CDR was calculated by taking the ratio between the area of optic cup and disc. If the CDR > 0.3 indicates the suspection of glaucoma and if the CDR ≤ 0.3, is considered as normal image. A novel segmentation technique which makes us of polar transform is used for segmentation of optic cup and optic disk. The proposed methodology out performs all the previous methods in terms of its time, efficiency and requires less computational resources. This will greatly enhance the development of detection systems of different ophthalmic diseases like glaucoma and now these systems can be deployed on mobile devices thus greatly increasing its usability. This proposed method can be used as an adjunct tool by the physicians to cross check their diagnosis and hence can be an efficient tool for early detection of Glaucoma.

REFERENCES:

[1] A. Basit and M. M. Fraz, ‘‘Optic disc detection and boundary extraction in retinal images,’’ Appl. Opt., vol. 54, no. 11, pp. 3440–3447, 2015.

[2] A. Sopharak, ‘‘Automatic detection of diabetic retinopathy exudates from non-dilated retinal images using mathematical morphology methods,’’ Comput. Med. Imag. Graph. vol. 32, no. 8, pp. 720–727, 2008.

[3] Archana Nandibewoor S B Kulkarni Sridevi Byahatti Ravindra Hegadi, Proceedings of the World Congress on Engineering 2013 Vol III, WCE 2013, July , 2013

[4] E. Trucco, A. Ruggeri, T. Karnowski, L. Giancardo, E. Chasum, J. P. Hubschman, B. al Diri, C. Y. Cheung, D. Wong, M. Abramoff et al., "Validating retinal fundus image analysis algorithms: Issues and a proposalvalidating retinal fundus image analysis algorithms," Investigative ophthalmology & visual science, vol. 54, no. 5, pp. 3546–3559, 2013

[5] G.D. Joshi, J. Sivaswamy, and S.R.Krishnadas, ‘‘Optic disk and cup segmentation from monocular color retinal images for glaucoma assessment,’’ IEEE Trans. Med. Imag., vol. 30, no. 6, pp. 1192–1205, Jun. 2011.

[6] Jan Odstrčilík, Radim Kolář, Vratislav Harabiš, Jiří Gazárek and Jiří Jan, Conference on signal processing August 2010.

[7] Jiag Liu, Tin Aung, Mani Baskaran, Conference paper of IEEE transcation, July, 2015.

[8] J. Sivaswamy, S. Krishnadas, G. Datt Joshi, M. Jain, S. Tabish, and A. Ujjwaft, "Drishtigs: Retinal image dataset for optic nerve head (onh) segmentation," in National Conference On Advanced Communication And Electronic Systems (NCACES 18) IEEE International Symposium on Biomedical Imaging (ISBI), 11th, 2014, pp. 53–56.

[9] J. J. Kanski and B. Bowling, Clinical Ophthalmology: A Systematic Approach. 8th ed. London, U.K.: Elsevier, 2015.

[10] Karthikeyan Sakthivel, Ragurajan Narayanan, International conference paper, July 2015

[11] K.Narasimhan, Dr.K.Vijayarekha, Theoretical Journal 15th November 2011. Vol. 33 No.1

[12] Maı'la Claro, Leonardo Santos, Wallinson Silva Fl´avio Araujo, Nayara Moura CLEI Electronic Journal, Volume 19, Number 2, Paper 4, August 2016

[13] M.D.Abramoff, M.K.Garvin, and M.Sonka, ‘‘Retinal imaging and image analysis,’’ IEEE Rev. Biomed. Eng., vol. 3, pp. 169–208, 2010.

[14] M. R. K. Mookiah, U. R. Acharya, C. M. Lim, A. Petznick, J. S. Suri, "Data mining technique for automated diagnosis of glaucoma using higher order spectra and wavelet energy features".(2012). 15. Niladri Halder, Dibyendu Roy, Arnab Chattaraj, Tanumoy Chowdhury. Vol. 3, Issue 3, March 2015 16.

[15] Shruti P Y, Sharangouda.N,International Journal of Advanced Research Vol. 4, Issue 6, June 2015 17. S.Leeand M. Brady, ‘‘Optic disk boundary detection, ’’in Proc. Brit. Mach. Vision Conf. (BMVC), 1991, pp. 359–362.

[16] Sobia Naz, Sheela N Rao, The International Journal Of Engineering And Science (IJES) || Volume-3 || Issue || 6 || Pages || 51-58 || 2014.

[17] Toshiaki Nakagawaa, Yuji Hatanakac, Akira Aoyamaa, Masakatsu Kakogawab, Takeshi Haraa,

[18] Hiroshi Fujitaa, Proc. of SPIE Vol. 6514 65142Z-1, 2007

[19] X. Luo, T. Liang, and W. Wang, ‘‘Static image segmentation using polar space transformation technique,’’ in Computer Engineering and Networking,

[20] W. E. Wong and T. Zhu, Eds. Cham, Switzerland: Springer, 2014, pp. 533–540.

[21] M. Abdullah, M. M. Fraz, and S. A. Barman, ‘‘Localization and segmentation of optic disc in retinal images using circular Hough transform and grow-cut algorithm,’’ PeerJ, vol. 4, p. e2003, May 2016.

[22] P. S. Mittapalli and G. B. Kande, ‘‘Segmentation of optic disk and optic cup from digital fundus images for the assessment of glaucoma,’’ Biomed. Signal Process. Control, vol. 24, pp. 34–46, Feb. 2016.

[23] M.A. Luengo-Oroz, E. Faure, and J. Angulo, ‘‘Robust iris segmentation on uncalibrated noisy images using mathematical morphology,’’ImageVis. Comput. vol. 28, no. 2, pp. 278– 284, 2010.

[24] S.Kavitha, S.Karthikeyan, Dr.K.Duraiswamy, Early Detection of Glaucoma in Retinal Images Using Cup to Disc Ratio 2010, Second International conference on Computing, Communication and Networking Technologies

[25] T.Walter, J.-C. Klein, Segmentation of color fundus images of the human retina: detection of the optic disc and the vascular tree using morphological techniques, Int. Symp. Med. Data Anal. 2199 (2001) 282–287

AIRCRAFT RECOGNITION IN REMOTE SENSING IMAGES BASED ON CONVOLUTIONAL NEURAL NETWORKS

Abin O. Bright [1], J.Blessy[2]
PG Student M E Applied Electronics[1]
Assistant Professor[2]
Department Of Electronics and Communication Engineering
Narayanaguru College of Engineering Manjalumoodu, KanayaKumari, Tamil Nadu, India

Abstract— Automatic aircraft recognition is a challenging task. Conventional methods always extract the overall shapes of aircraft at first and then represent the aircraft based on the extracted shape with different features for recognition. The major problem of these methods is that they have a high requirement on shape extraction, which is too idealistic for targets in Remote sensing images. To address these challenges, propose a new aircraft recognition framework, which can be divided into three processes: region proposal, classification, and accurate aircraft localization process. First, a region proposal method is used to generate candidate regions with the aim of detecting all objects of interest within these images. Then, generic image features from a local image corresponding to each region proposal are extracted by a combination model of 2-D reduction convolutional neural networks (CNNs). Haar cascade method is used to classification of aircraft. To improve the location accuracy, introduces an unsupervised score based bounding box regression (USB-BBR) algorithm, combined with a non-maximum suppression algorithm to optimize the bounding boxes of regions that detected as objects. Experiments show that the dimension-reduction model performs better than the retrained and fine-tuned models and the detection precision of the combined CNN model is much higher than that of any single model. The proposed USB-BBR algorithm can more accurately locate objects within an image. Compared with traditional features extraction methods, such as elliptic Fourier transform based histogram of oriented gradients and local binary pattern histogram Fourier, the proposed localization framework shows robustness when dealing with different complex backgrounds.

Keywords— Aircraft recognition, Convolutional neural networks (CNN), unsupervised score-based bounding box regression (USB-BBR), Haar Cascade method.

INTRODUCTION

To recognize the types of aircraft is very important. Identification of the activity patterns of aircraft, detect the unusual trends of aircraft, and make judgment through type recognition. However, aircraft recognition with high-resolution space borne Remote sensing images is a challenging task. It is still difficult to distinguish targets of some types from the others. In conventional aircraft recognition methods, several methods are based on using rotation-invariant features after binarization.

Currently, there is small demand for accurate localization in the remote sensing field. The majority of studies focuses on detection rather than localization (the two processes have been confused by some people). Aircraft detection in remote sensing images faces far more challenges because of more complex background information they contain than that of natural images. Remote sensing images offer information about the texture, shape, and structure of ground objects, and they can be used for precise object identification. However, in addition to providing ample information for object detection, they also present information redundancy problems. Moreover, because of noise interference, weather, illumination intensity, and other factors, object detection in remote sensing images is a troublesome issue.

In this paper, focus on accurate localization of detected objects rather than simple object detection. Based on this aspect, use object localization to summarize this paper. In this paper, we tackle the feature extraction problem for aircraft detection in remote sensing images using convolutional neural network (CNN) models. CNN relies on the specific layer structure to learn the essential features of input images, thus avoiding the effort of designing a feature extraction strategy. In addition, CNN models have a wide range of application. CNNs with deeper layer structure tend to have better learning abilities. In this paper, the feature extraction strategy is based on CNN models with a deep layer that can describe objects in remote sensing images. Finally, propose a new aircraft localization framework for remote sensing images that can detect, classifying and locate objects accurately by using Haar cascade and unsupervised score based bounding box regression (USB-BBR) method.

RELATED WORK

Qichang Wu, Hao Sun, Xian Sun, Daobing Zhang, Kun Fu, and Hongqi Wang have proposed a targets in high-resolution remote sensing images. Automatic aircraft recognition is a challenging task. Conventional methods always extract the overall shapes of aircraft at first and then represent the aircraft based on the extracted shape with different features for recognition. The major problem of these methods is that they have a high requirement on shape extraction, which is too idealistic for targets in satellite images. In this paper, propose a new aircraft recognition approach that can recognize aircraft robustly without perfect extraction of silhouette or shape of aircraft as a precondition, and can deal with the situation of parts missing and shadow disturbance. Specifically, a direction estimation method is proposed first to align aircraft to a same direction. Then, a reconstruction-based similarity measure is proposed, which transforms the type recognition problem into a reconstruction problem. Finally, a jigsaw matching pursuit algorithm is proposed to solve the reconstruction problem. The main advantage of the method lies in that the method can recognize aircraft robustly and excludes the target overall shape extraction phase, which is usually included in the traditional recognition methods and is not practical due to disturbing background. Experimental results show that our recognition method yields a good performance

Yu Li, Xian Sun, Hongqi Wang, Hao Sun, and Xiangjuan Li(2010) have proposed contour-based spatial model which can detect geospatial targets accurately in high resolution remote sensing images. To detect the geospatial targets with complex structures, each image was partitioned into pieces as target candidate regions using multiple segmentations at first. Then, the automatic identification of target seed regions is achieved by computing the similarity of the contour information with the target template using dynamic programming. Finally, the contour-based similarity was further updated and combined with spatial relationships to figure out the missing parts a CBS model has been proposed to solve the problem of detecting geospatial targets present in high resolution remote sensing images accurately and automatically. Multiple segmentations are employed to produce candidate target regions. According to their contour similarities, the seed regions are identified. Spatial relationship is utilized to obtain missing parts of the target instances. They use dynamic programming to calculate shape similarities efficiently since it utilizes the ordering information between contour points. Experiments with aircraft as example target demonstrate the precision, robustness, and effectiveness of the proposed method. The CBS model is a global shape model, which captures the global characteristic of targets

PROPOSED METHOD

The proposed aircraft localization framework follows a pipeline approach. Which can be divided into three processes: region proposal, classification, and accurate aircraft localization process. First, when dealing with a test image, use a selective search algorithm to generate category independent possible regions. Then, all these candidate regions are sent to a combined model consists of 2-D reduction CNNs. Class labels and classification scores for each candidate region are an average output of two CNN models. Finally, perform an accurate object localization process to address these classified regions. For accurate aircraft localization, the propose method using the unsupervised score-based bounding box regression (USB-BBR) method to improve box localization precision after using the non-maximum suppression (NMS). For classification Haar cascade method is using. In this section, present our design for each procedure. The proposed object localization framework is shown in Resulted figure.

REGION PROPOSAL

Traditionally, a sliding window technique has been used for aircraft detection; however, the sliding window technique is an exhaustive search method and is computationally expensive. Recently proposed a selective search algorithm that produces object regions by taking the underlying image structure into account. The selective search algorithm yields a completely class-independent set of locations. It also generates fewer locations, which simplifies the problem because the sample variability is lower. More importantly, it frees up computational power, which can then be utilized for more robust machine learning techniques and more powerful appearance models.

Aircraft can occur at any scale within an image because of the diverse means for acquiring images. Moreover, images at the same scale may be different sizes. Therefore, we collect images that share approximately the same image with the aim of acquiring all the similar objects at one scale. Then, apply the selective search algorithm to address the objects that have different sizes within an image.

The experiments also indicate that the greater the number of candidates, the higher the recall will be. While the recall value may be different for remote sending images, in any image classification task, it is a key factor that influences both the CNN detection result and the accuracy of object localization.

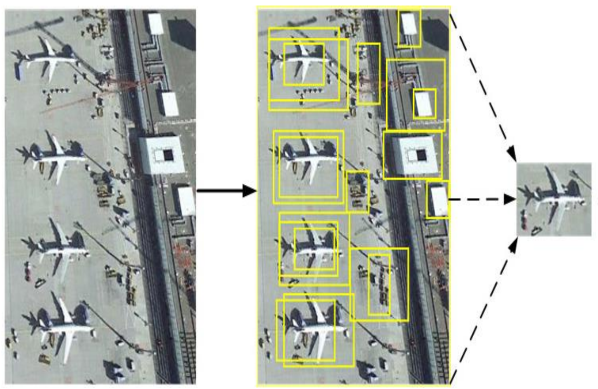

Proposed aircraft localization framework. Fig. 1 Test image. Fig. 2 Selective search method produces most of the candidate object regions from the test image and adds some candidate regions extracted from low region density areas, where the selective search method generates few regions

FEATURE EXTRACTION

A CNN model consists of convolution layers, pooling layers, and full connection layers. A convolution layer has several filters and generates different feature maps using these filters on local receptive fields in the maps of the previous layer or input. The filter size can be $n \times n$ (where n is smaller than the input size). Weights are shared between convolution layers. The pooling layer uses filters to generalize the brief representation of the convolution layer to reduce the number of parameters. There are several pooling types; these include max pooling and average pooling. The pooling operation provides a form of translation invariance. The feature becomes more complex and global as the layers become deeper.

In this paper, the CNN models chosen to extract features are Alex Net and Google Net due to their superior performance. To retain more information for back propagation, for both the Alex Net and Google Net networks, add a 64-D inner product layer before the last inner-product layer. For Alex Net, we reduce the dimension of the second full-connection layer from 4096 to 64, and for Google Net, add a 64-D layer after the last convolutional layer. Moreover, the two CNNs are combined to detect objects simultaneously and the result of this combined CNN models is the averaged outputs of the two CNN models

To perform feature extraction, first extract image patches from the candidate regions generated by the region generation process. Then, normalize the image patches to 227×227 to fit the input dimensions of the CNN models and use them as input to the CNN to extract features. The last layers of the CNN models are softmax classification layers. For the combined CNN model, need to perform forward propagations of the two CNN models. After forward propagation, the two CNN models produce classification results of these candidate regions. The regions will have class labels and class scores after forward propagation. For examples, assume that the candidate region is b and that the class label and classified scores for the entire set of classes computed by model A are lA and sA, while the class label and classified scores for the entire set of classes computed by model B are lB and sB. The class score S of the model combination is the average of sA and sB, while the class label L of the model combination is the label according to the maximum of S.

International Journal of Engineering Research and General Science Volume 6, Issue 2, March-April, 2018
ISSN 2091-2730

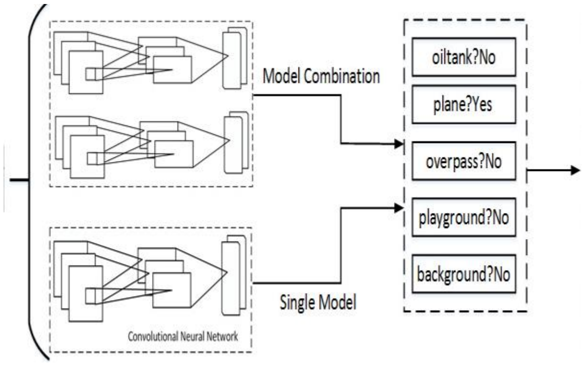

Fig. 3 CNN is applied to extract the features from these candidate regions. Fig. 4 Classification results of the regions. We used two approaches to obtain the classification results of candidate regions: one is a single model strategy and the other is a model combination strategy that averages the outputs of two CNN models.

ACCURATE AIRCRAFT LOCALIZATION

To produce the optimum bounding box for locating the object, propose method a two-stage object accurate localization method: NMS and USB-BBR. The NMS method is mainly used to eliminate region overlap. The USB-BBR method to reduce the location errors. All the scored regions are allocated into different groups; each group belongs to one object that needs to be detected. For a set of scored candidate regions $B = \{b1, b2, . . . , bn\}$ where n is the total number of regions in the set, the regions in B are first sorted by their area in ascending order. The next step is to classify the regions of B into m groups, where a group $G = \{G1, G2, . . . , Gm\}$. The grouping begins with the first sorted region, computing the overlap area ratio of the first sorted region to that from the rest of B. If the overlap area ratio is greater than or equal to a given threshold, the two regions are classified into the same group; otherwise, only the first sorted region is classified into the group. The group process completes when all the regions in B have been computed.

Though this grouping process, each object that needs to be detected may have a group of scored regions. The goal is to regress the regions of each group Gk, namely, to produce the optimum bounding box for locating the object. Assume that $Ik = (xk , yk,wk , hk)T$ is the regressed bounding box of Gk, where (xk, yk) is the center coordinate of Ik and (wk , hk) are the width and height of Ik , respectively. Thus, the goal is to obtain Ik. For bki Gk, $Dki = (xki,, yki, wki , hki)T$ corresponds to the i th scored region in Gk. Given $ci = Ik - Dki$, we can obtain Ik by

$$L(Ik) = \text{argmin} \sum_{i=0}^{n} u_i \, c_i^T \, c_i$$

where ui is the region score bki in Gk .

Algorithm 1 USB-BBR

Input: The full set of regions $B = \{b1, b2, . . . , bn\}$, a

threshold δ, where $0 < \delta < 1$, a max iteration, t, and

an iteration step s, where $0 < s < \delta$

1: **Set**: $G = \{b1, b2, . . . , bm\}$ $(m = n)$

2: **Set**: $R = \{b1, b2, . . . , bm\}$

3: $I = \emptyset$

4: **while** $t > 0$ and $\delta > 0$ **do**

5: sort the elements of G in ascending order by the corresponding

region areas of R

6: $i = 0$

7: **while** G _= $\emptyset$ **do**

8: $i = i + 1$

9: get the area a of r which is the first element of R

10: get the first element G' of G

11: $G'i= G'$

12: remove G' from G

13: get L (the length of G)

14: **for** $j = 1, 2, . . . , L$ **do**

15: get the overlap area *overa* between $r\,j$ and r

16: **if** $overa/a \geq \delta$ **then**

17: $Gi= G'i$ Ù$G\,j$

18: remove $G\,j$ from G

19: **end if**

20: **end for**

21: **end while**

22: $m = i$

23: $G = \{G1, G2, . . . , Gm\}$ $(G1 = G'1, G2 =G2, . . . , Gm = G'm)$

24: update the elements of R according to G

25: $t = t - 1$

26: $\delta = \delta - s$

27: **end while**

28: obtain the final region grouping set $G = \{G1, G2, . . . , Gm\}$

for $k = 1, 2, \ldots, m$ **do**

Ik = *argmin_li*=1 *ui cTi ci* (*l* is the length of *Gk*)

append *Ik* to I

end for

Output: *I*

The first iteration regression result of *G* is denoted as $R = \{r1, r2, \ldots, rm\}$, computed by (1). The regions in *R* may belong to the same object, so using an iterative process to update *G*. Each iteration uses a descending threshold and the same grouping method to update *G* by comparing the overlap area ratio of regions in *R*. Then, *R* is computed from the updated *G*. The grouping results occur in the next update iteration, and the iteration process completes when it reaches a specified maximum number of iterations or the threshold is less than or equal to 0.The *I* is computed by the final grouping set, *G*. The threshold for the overlap area ratio decreases as the iteration time increases. The USB-BBR algorithm is solved by the least-squares method. Algorithm 1 describes the process of USB-BBR. Fig. 7 shows the USB-BBR process. After sorting the classified regions in *B*, the grouping process begins moving from the first sorted region to the last one. All regions are divided into three groups by computing their overlap area ratio. Then, the regression optimal region of each group is computed. The regression result of *B* is *R*. The regions in *R* may still belong to the same object, so we use an iterative process to update *G* and *R*. The final regression result is computed when the iterative update process completes. Here, *I* is the regression result computed by the final grouping set.

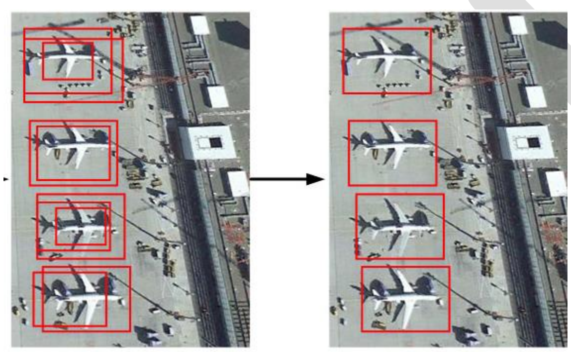

Fig. 5 Classification results of the candidate regions. Fig. 6 Final detection results after the accurate object localization process using USB BBR.

AIRCRAFT CLASSIFICATION

Haar cascade classifier consists of a list of stages, where each stage consists of a list of weak learners. The detected aircrafts in question by moving a window over the image. Each stage of the classifier labels the specific region defined by the current location of the window as either positive or negative – positive meaning that an object was found or negative means that the specified aircrafts was classified in the image. If the labelling yields a negative result, then the classification of this specific region is here by complete and the location of the window is moved to the next location. The classifier yields a final verdict of positive, when all the stages, including the last one, yield a result, saying that the object is found in the image.

A true positive means that the aircrafts in question is indeed in the image and the classifier labels it as such – a positive result. A false positive means that the labelling process falsely determines, that the aircrafts are located in the image, although it is not. However, each stage can have a relatively high false positive rate, because even if the n-th stage classifies the non-object as actually being the object, then this mistake can be fixed in n+1-th and subsequent stages of the classifier. Finally aircrafts was classified according to their shapes. In Haar cascade method the final output will mention according to the structure. In output it is shown in various colours.

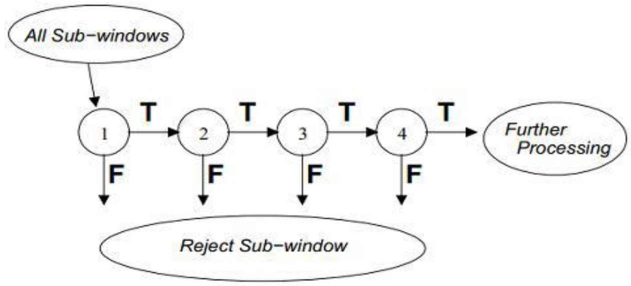

Fig. 7 Aircraft Classification Based on Haar Cascade Method

EXPERIMENTS AND RESULTS

The proposed framework on detection performance. For the proposed aircraft localization framework, used a large data set to train the CNN models and applied model fine-tuning to initialize the weighs. Also used a model combination method when classifying candidate regions, and the accurate object localization process to enhance the location precision. Systematically analyses the performance effects caused by these strategies.

Table 1. Final output accuracy, recall, precision is detected

Type	Accuracy	Recall	Precision
RED	94.2%	0.9603	0.9235
GREEN	94.5%	0.9302	0.9333
BLUE	95.0%	0.9403	0.9001

FEATURE EXTRACTION AND CLASSIFICATION

The results show that weight initializations play a crucial role in the learning ability of CNN models, and the model combination strategy can improve the precision value to a certain extent. Namely, the fine-tuned model can increase the learning performance of CNN models and the detection precision of a combination mode is higher than that of a single model.

To deal with the problem of several regions corresponding to one object, we used the USB BBR algorithm after NMS. The detection results of using the GoogleNet-finetune model. Compared with the result from using a CNN with NMS, using a CNN with USB-BBR can greatly increase the localization precision, because the process optimizes several regions into one region; consequently, the location accuracy is much higher

Table 2. Details of the Transformation of positive Training Samples

Type	Argument
Translation Transform	$dw = 0.1w\ dh=0.1h$
Scale Transform	$ds=(0.8,0.9,1.1,1.2)$
Rotation Transform	$d0= 90°, 180°,270°$

The above table shows the translation transform, scale transform and rotation transform of an aircraftThe rotation transform typically performs 90°, 180°, and 270° rotation; however, when there are few instances of a class, the angle of rotation deceases to increase the number of rotations. When the IoU was greater than or equal to 0.5 compared with a ground-truth region chosen during the first positive sample collection process, the region became a positive sample; otherwise, when the IoU was less than 0.3 with the ground-truth region, the region became a negative sample The ratio of positive samples selected from the first and second positive data set sources is 5:1, and the positive samples from the second part of the positive data set were used to enhance the adaptability of the CNN models. All the CNN data set samples were resized to 227 × 227.

REGION PROPOSAL AND UNSUPERVISED SCORE-BASED BOUNDING BOX REGRESSION

Fig.8 shows a portion of the comparison detection results both with and without the USB-BBR method. The first column is the detection result without using the bounding box regression method and the second column is the detection result using the USB-BBR method. As Fig.9 shows, the USB-BBR has better localization precision. Therefore, the USB-BBR method can increase the detection localization precision. Comparative detection results both with and without USB-BBR

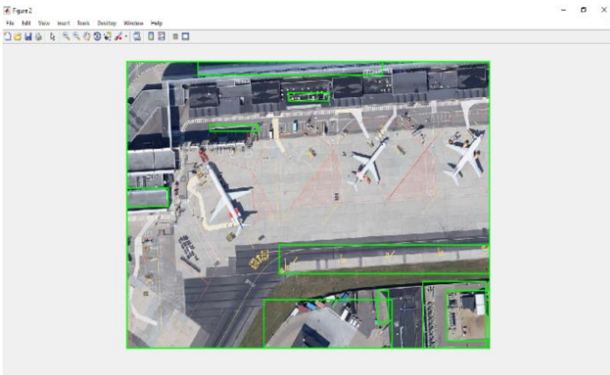

Fig.8 Comparative detection results both with and without USB-BBR. The first column shows the detection results without USB-BBR.

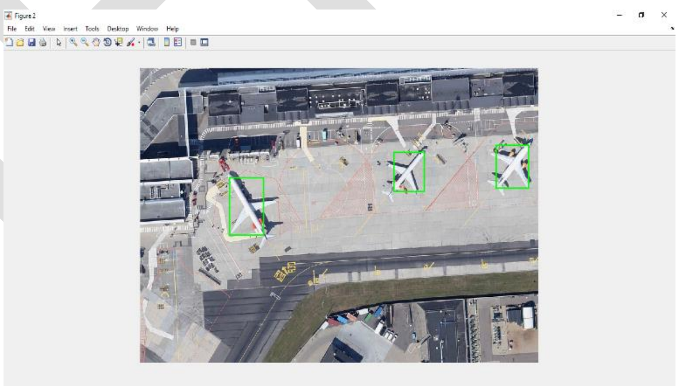

Fig. 9 The second column shows the detection results with USB-BBR.

CLASSIFICATION OF AIRCRAFT

The final output of aircraft recognition and classification by using CNN and Haar cascade method it will show on the below fig.10 the classified output mention in various colors and it is classified according to the shape and structure of the aircraft. The recalling and precision values are better than existing method. Haar cascade method is also used for feature extraction of aircraft.

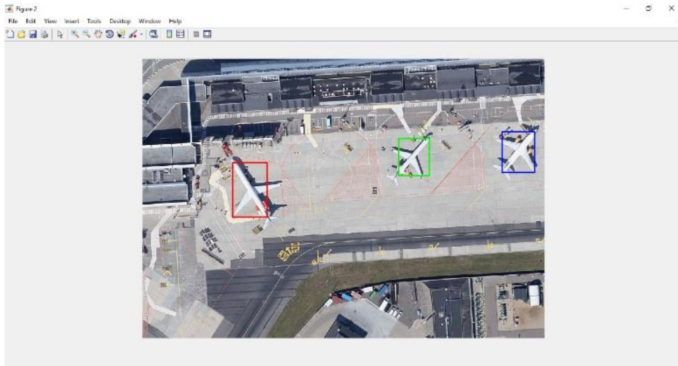

Fig. 10 By using Haar cascade method final output showed in various colors

CONCLUSION

Proposed aircraft localization framework based on CNN in remote sensing images. The framework uses the CNN and Haar models to extract object features and obtain classification results. In the first stage, used a selective search method to generate the major part of the candidate object regions. In the second stage, designed a dimension reduction model using trained models to initialize the network weights and then use it to extract features and classify the aircraft to different categories by using Haar cascade method. Also tested a retrained model and a fine-tuned model. In the third stage, the proposed a new USB-BBR algorithm, as part of the accurate object localization process, to obtain better detection localization precision, and used NMS to decrease the number of overlapped regions. The addition of the USB-BBR method can help to obtain an optimal bounding box for each group of classified regions. In addition, investigated the influences of different sizes of training data sets, different weight initialization methods, and different model combinations on detection performance. These results can help guide other researchers to obtain good results. The results of the experiments indicate that the proposed localization framework is both simple and robust. In further work, the aim is to enhance this framework and improve its detection and localization performance using GPS technology and the features describe of the objects

REFERENCES:

1. P. Agrawal, R. Girshick, And J. Malik, 2014, "Analyzing The Performance OfMultilayer Neural Networks For Object Recognition," In Proc. Eur. Conf.Comput. Vis., Pp. 329–344.
2. H. Azizpour, A. S. Razavian, J. Sullivan, A. Maki, and S. Carlsson, Sep. 2015, "Factors of transferability for a generic convnet representation," IEEE Trans. Pattern Anal. Mach. Intell., vol. 38, no. 9, pp. 1790–1802.
3. Y.L. Boureau, J. Ponce, and Y. Lecun, 2010, "A Theoretical Analysis of Feature Pooling In Visual Recognition," In Proc. Int. Conf. Mach. Learn., Pp. 111–118.
4. G. Cheng and J. Han, 11–28 Mar. 2016, "A Survey on Object Detection in Optical Remote Sensing Images," Isprs J. Photogram. Remote Sens., Vol. 117.
5. G. Cheng, J. Han, P. Zhou, And L. Guo, Dec. 2014, "Multi-Class Geospatial Object Detection And Geographic Image Classification Based On Collection Of Part Detectors," Isprs J. Photo Gramm. Remote Sens., Vol. 98, Pp. 119–132.
6. G. Cheng, P. Zhou, and J. Han, Dec. 2016, "Learning Rotation-Invariant Convolutional Neural Networks for Object Detection in Vhr Optical Remote Sensing Images," Ieee Trans. Geosci. Remote Sens., Vol. 54, No. 12, Pp. 7405–7415.
7. G. E. Dahl, T. N. Sainath, And G. E. Hinton, May 2013, "Improving Deep Neural Networks For Lvcsr Using Rectified Linear Units And Dropout," In Proc. Ieee Int. Conf. Acoust., Speech Signal Process. (Icassp), Pp. 8609–8613.
8. Dean Et Al., 2012, "Large Scale Distributed Deep Networks," In Proc. Neural Inf. Process. Syst. (Nips), Pp. 1–11.
9. A. Grubb and J. A. Bagnell, Oct. 2013, "Stacked Training for Overfitting Avoidance in Deep Networks," In Proc. Int. Conf. Mach. Learn., P. 1
10. J. Han Et Al., Mar. 2014, "Eficient, Simultaneous Detection Of Multi-Class Geospatial Targets Based On Visual Saliency Modelling And Discriminative Learning Of Sparse Coding," Isprs J. Photogram. Remote Sens., Vol. 89, Pp. 37–48.
11. J. Han, D. Zhang, G. Cheng, L. Guo, And J. Ren, Jun. 2015, "Object Detection In Optical Remote Sensing Images Based On Weakly Supervised Learning And High-Level Feature Learning," Ieee Trans. Geosci. Remote Sens., Vol. 53, No. 6, Pp. 3325–3337.
12. A.G. Howard, 2013, "Some Improvements on Deep Convolutional Neural Network Based Image Classification." Unpublished Paper. [Online]. Available: Https://Arxiv.Org/Abs/1312.5402
13. Y. Huang, L.Zhang, P. Li, and Y. Zhong, 2010, "High-Resolution Hyper-Spectral Image Classfication with Parts-Based Feature and Morphology Profile in Urban Area," Geo-Spatial Inf. Sci., Vol. 13, No. 2, Pp. 111–122.

ISSN 2091-2730

14. T. Ishii, R. Nakamura, H. Nakada, Y. Mochizuki, And H. Ishikawa, May 2015, "Surface Object Recognition With Cnn And Svm In Landsat 8 Images," In Proc. Iapr Int. Conf. Mach. Vis. Appl., Pp. 36.
15. Jiang, L. Cao, M. Cheng, C. Wang, and J. Li, Oct. 2015, "Deep Neural Networks-Based Vehicle Detection In Satellite Images," In Proc. Int. Symp. Bioelectron. Bioinf, Pp. 184–187.
16. Krizhevsky. (2014), "One Weird Trick For Parallelizing Convolutional Neural Networks." [Online]. Available: Https://Arxiv.Org/Abs/1404.5997
17. Y. Li, X. Sun, H. Wang, H. Sun, and X. Li, Sep. 2012 "Automatic Target Detection in High-Resolution Remote Sensing Images Using A Contour-Based Spatial Model," Ieee Geosci. Remote Sens. Lett. Vol. 9, No. 5, Pp. 886–890
18. Mahendran and A. Vedaldi. 2014, "Understanding Deep Image RepresentationsBy Inverting Them." Unpublished Paper. [Online]. Available: Https://Arxiv.Org/Abs/1412.0035
19. Paine, H. Jin, J. Yang, Z. Lin, and T. Huang, 2013, "Gpu Asynchronous Stochastic Gradient Descent to Speed Up Neural Network Training." Unpublished Paper. [Online]. Available: Https://Arxiv.Org/Abs/1312.6186
20. S. Razavian, H. Azizpour, J. Sullivan, and S. Carlsson, Jun. 2014, "Cnn Features Off-The-Shelf: An Astounding Baseline for Recognition," In Proc. Cvpr, Pp. 806–813.
21. Shao, W. Yang, G. Liu, and J. Liu, Jul. 2012, "Car Detection From High Resolution Aerial Imagery Using Multiple Features," In Proc. Ieee Int. Geosci. Remote Sens. Symp. (Igarss), Pp. 4379–4382.
22. H. Sun, X. Sun, H. Wang, Y. Li, and X. Li, Jan. 2012, "Automatic Target Detection In High-Resolution Remote Sensing Images Using Spatial Sparse Coding Bag-Of-Words Model," IEEE Geosci. Remote Sens. Lett, Vol. 9, No. 1, Pp. 109–113.
23. J. R. R. Uijlings, K. E. A. Van De Sande, T. Gevers, and A. W. M. Smeulders, Apr. 2013, "Selective Search for Object Recognition," Int. J.Comput. Vis., Vol. 104, No. 2, Pp. 154–171.
24. Z. Xiao, Q. Liu, G. Tang, and X. Zhai, 2014, "Elliptic Fourier Transformation Based Histograms Of Oriented Gradients For Rotationally Invariant Object Detection In Remote-Sensing Images," Int. J. Remote Sens., Vol. 36, No. 2, Pp. 618–644.
25. F. Zhang, B. Du, and L. Zhang, Apr. 2015, "Saliency-Guided Unsupervised Feature Learning For Scene Classfication," Ieee Trans. Geosci. Remote Sens., Vol. 53, No. 4, Pp. 2175–2184.

CROWD ATTRIBUTES RECOGNITION AND ALERTING USING SPARSE RECOGNITION

Arya Mohan.S.[1], Danya Mercline[2]

PG Student [1](M.E-Applied Electronics) , Assistant professor [2]

Department of Electronics and Communication Engineering, Narayanaguru College of Engineering,Manjalumoodu, TamilNadu

Abstract— Human behavior analysis has become a critical area of research in computer vision and artificial intelligence research community. In recent years, video surveillance systems of crowd scenes have witnessed an increased demand in different applications, such as safety, security, entertainment, and personal mental health. Although many methods have been proposed, certain limitations exist, and many unresolved issues remain open. In this work, the proposed novel-temporal sparse coding representation, based on sparse coded features with k-means singular value decomposition for robust classification of crowd behaviors has been considered. Extensive experiments have shown that, with sparsely coded features captured with vital structures of video scenes yields discriminant descriptors for classifications than conventional bag-of-visual-features. Relying on the measurable features of crowd scenes and motion characteristics, it can be used to represent different attributes of crowd behaviors. Experiments on hundreds of video scenes were carried out on publicly available datasets. Quantitative evaluation indicates that, the proposed method display superior accuracy, precision and recall in classifying human behaviors with linear support vector machine when compared with the state-of –the-art methods. The detected image will be processed by a processing unit and then an alert can be send to the authorized person through Gmail.

Keywords— Human behavior, crowd scenes, histogram of optical flow, histogram of oriented gradient, artificial intelligence, sparse coding, bag-of-visual features.

INTRODUCTION

In recent years, recognizing human activity in physical environment finds importance in different applications in areas such as intelligent video surveillance[14], and healthcare surveillance[15]. However, accurate detection and recognition of human activity remain an open problem due to the background noise, occlusions, scale and view point changes. Moreover, the interest in the field of video surveillance technology[7],[12], is increasing with the availability of low-cost sensors and processors; especially in order to understand human behavior. As a result, a large volume of video data containing excessive behavior information is available, which is not adequately analyzed by human operators. The field of intelligent crowd surveillance recently received an increase in global funding and attention, because of its usefulness in the monitoring of public areas: shopping centers, banks, airports, train stations, subway stations, sports areas, and traffic control and congestion prediction. Crowd analysis can be sub-classified based on the following area of Applications: crowd behavior, crowd segmentation, crowd tracking, crowd motion detection and crowd density estimation. A substantial analysis of the existing reviews in [7] and [6] reveals a wider perspective on the potential application of computer vision and artificial intelligence in the efficient representation of human behavior in crowded scenes.

There are different contextual terms used in the definition of human behavior including atomic actions, action sequences, and activity[3]. Atomic actions correspond to instantaneous entities upon which an action is formed. Actions correspond to a sequence of atomic actions that fulfils a task or purpose; while activities consists of a sequence of actions over space and time. The overall objective of any behavior recognition system is to detect, analyze and interpret the contextual activity. To bring about intelligent aid to human capability, the crowd analysis aims to create an efficient platform with the capability of mimicking the human intelligence by learning and classifying behaviors in normal and abnormal context. Despite many efforts, detecting appearance and dynamic information from a crowd scene remains challenging in activity analysis. Theoretically, in most activity analysis findings, objects of interests are extracted from the background, and followed by tracking the object. One can inferred that the foreground extracted is used in holistic behavior understanding. Unluckily, this mainstream representation is considered too difficult for crowd videos analysis.

Human behavior analysis in crowd offers opportunities for a wide range of applications; for instance, visual surveillance, video indexing, searching, robotics, health-care, animation, and gaming. Visual surveillance plays a vital role in the monitoring of the human activities in realistic scenes using visual sensors; such as Closed-Circuit Television (CCTV)cameras. The traditional surveillance systems essentially depend on human operates to monitor people activities, a region of interest tracking from one camera to another, or detecting of anomaly occurrence in a scene. However, the majority of the miss-detected incidences in crowd scenes are due to the manual handling of the system and poor observation by the CCTV operators. These shortcomings could be due to excessively displayed video screens, boredom due to prolonged observation, and lack of basic knowledge in classifying behaviors, and distractions by additional operational responsibilities; consequently, important events may be miss-detected in critical surveillance task[3]. A human behavior analysis system tends to solve the aforementioned problems, by providing automated high-performance framework, which assists human operators to achieve an effective management of crowds.

A novel spatio-temporal sparse coding representation**,** based on Sparse Coded features with K-means Singular Value Decomposition(SCKSVD) for robust classification of human behavior especially student for learning, improve accuracy and simplify model structure. The notion of space-time features used is [17] extended, which was formulated based on 3D interest points and bag-of-visual feature. The bag-of-visual feature was used for quantization and estimating the motion and appearance gradients of a video scene. However, among the limitations of the Bag-of-visual feature, it was observed that spatial relationship among the video patches was poorly captured which resulted to low recognition rate in [17] . The SCKSVD models was evaluated on the following crowd datasets; University of Central Florida (UCF), Chinese University of Hong Kong (CUHK), and University Technology PETRONAS Crowd dataset(Crowd-UTP),in comparison with baseline methods.

RELATED WORKS

In this section, the review of existing studies on crowd analytic models are presented. Existing works on crowd analysis can be categorized into holistic methods, particle/track let based methods, trajectory based and spatio-temporal models.

A. HOLISTIC METHODS

Holistic methods analyze the crowd pattern in global perspective[4],[10] and [11]. Chan and Vasconcelos in[8] analyzed crowd setup based on dynamic textures models, which represent video sequences as observations from a linear dynamical system. Mahadevan *et al.* in extend the concept of dynamic texture models to anomaly detection in crowd scenes. There are also works that utilize local level features, e.g., optical flow, to build up models for analyzing the motion trajectories in crowded scenesin X.wang *et al.*[18] and D.Kuettel *et al.*[8]. These approaches prove effective in global scene visualization. However, these approaches are computationally complex due to tedious training. In addition, as a result of applicability of some local level visual features, pedestrian's motion detection is difficult in sparse crowd scenes.

B TRAJECTORY-BASED METHODS

Trajectory-based methods consider a crowd as a collection of pedestrians and analyze the communality between individual pedestrians. Trajectories analysis of crowd scene is presented in [9] and [19]. Choi and Savares [5] reported a hierarchical activity model that identify the relationship between individual trajectories and collective actions. Wang *et al.*[19] proposed a technique for trajectory clustering and semantic region recognition. These techniques analyze the motion patterns of individual pedestrian. However, the computed models are not deployable to different scenes. Morris and Trivedi in [13] proposed a model that captured pedestrians trajectories, action recognition and anomaly detection in crowd scenes. The goal of our work is different. We aim at recognizing and classifying crowd scenes by analyzing the crowd spatio-temporal features of the input scenes.

C. PARTICLE-BASED METHODS

Particle-based also called tracklet-based models are effective in analysis of dense crowd scenarios [12] ,[1] and [16] Saad work in [16] is based on a particle-based approach that is used in analysis of interactions between crowd members and also in measurement of flow complexity. The tracklet-based methods deal with tracklets generated by Kanade Lucas Tomasi (KLT) trackers in [20] and.Zhou *et al* [20]. in proposed a mixture model to learn motion patterns and predict individual behaviors from tracklets. Shao *et al.* in measure the collective crowd motions based on the path similarities on the collective manifold. These methods provide a trade-off between holistic approaches and trajectory-based methods. The limitation is that individual information cannot be fully covered in the scene. Our proposed method studies not only the global information but also the individual local information.

D. SPATIO-TEMPORAL FEATURES MODELS

Spatio-temporal models found in the literature include.C.S.J.Junior *et al.* [6] ,S.Ali *et al* [2] Moreover, model for activity recognition in a video has been reported. In this study, distance metric learning was implemented using physical activity recognition and intensity estimation. In another recent development,the authors proposed a novel multi-view feature selection method via joint local pattern-discrimination and global label-relevance analysis (mPadal). The proposed mPadal employs a new joint local-and-global approaches of human pose. Experimental findings show that mPadal outperforms other baseline methods on publicly available activity recognition dataset. Multi-view models, based on histogram of motion intensities (HMI) and histogram of oriented gradient (HOG) descriptors are used in analysis of human action in video scenes. A novel approach for human action recognition using 3D skeleton joints recovered from RGB-D cameras. Recently, a computer vision algorithm for classification of gait anomalies from kinect is proposed in for neurodegenerative diseases like Parkinson and Hemiplegia. These approaches may not be suitable for real time application because of the computational complexity involved. Another limitation of the approaches is that, they are suitable to few individual scene as such may not be applicable to crowded scenarios. Another closely related work on behavior recognition has been presented recently. They conducted a detailed survey on activity recognition using semantic space features such as pose, pose let, attributes, related object, and scene context. They extensively exploited the aforementioned features to recognize behavior in video data and still images. The literature survey revealed that the studies in the domain of activity recognition and crowd behavior classication rely heavily on BoVF algorithms in training the classification models.

BoVF algorithms A.N.Shuaibu *et al* [17] lack convergence speed and poor accuracy due to long iterative nature, and its performance is greatly affected by number of k-clusters. The local convergence of BoVF algorithms can lead to computational complexity for real-time behavior analytic application. However, sparse representation approach performs better and avoid possibility of being trapped in local minima which is commonly observed with BoVF -[17]. Sparse features algorithms has been proven to effectively work with linear classifiers for simplification of the models and performance improvement of image lesio discrimination. Reviews on more efficient methods on crowd scene classification have been reported. The proposed SCKSVD model overcomes the limitations listed in the aforementioned methods. Innovative model design, appearance and dynamic information can be effectively learned from sparsely coded features. In addition, the proposed model is capable of extracting HOG and histogram optical flow (HOF) from long-range scenes (i.e.200 frames or more) without sampling or compression. The SCKSVD addresses the common limitations of the state of-the-art models such as complexity in training and poor classification accuracy.

PROPOSED WORK

This section describes the proposed method for behavior understanding in crowd scene based on learned spatiotemporal sparse feature representation. Sparse signal representations are becoming increasingly popular and lead to state-of-the-art results in various applications such as face recognition, image demising and imprinting, and image classification. The main reason being the intrinsic sparse nature of image representations when using fixed bases such as discrete cosine transforms or wavelets. In addition, the basis vectors can be learned from the data itself and be constrained to produce a sparse representation. The entire process is presented in the flowchart.

A. DENSE SPATIO-TEMPORAL INTEREST POINTS

This section gives an overview of the feature extraction used, by reading the video input data (*v*), followed by extraction of interest point patches (*i*). We extend the concept of Space Time Interest Points (STIP) used, and detect the key interest points using spatio-temporal extension of Harris corner detector. Histogram of Oriented Gradient (HOG) and Histogram of Optical Flow (HOF) are extracted as stated *extractHOG*(*patch*) and *extractHOF*(*patch*) respectively. The features are concatenated and train with the sparse model. In this work we carried out scale selection at multiple levels and then extracted features as compared to single scale selection. The multiple-scale selection of spatiotemporal features reduced the computational complexity and present good recognition performance as presented.

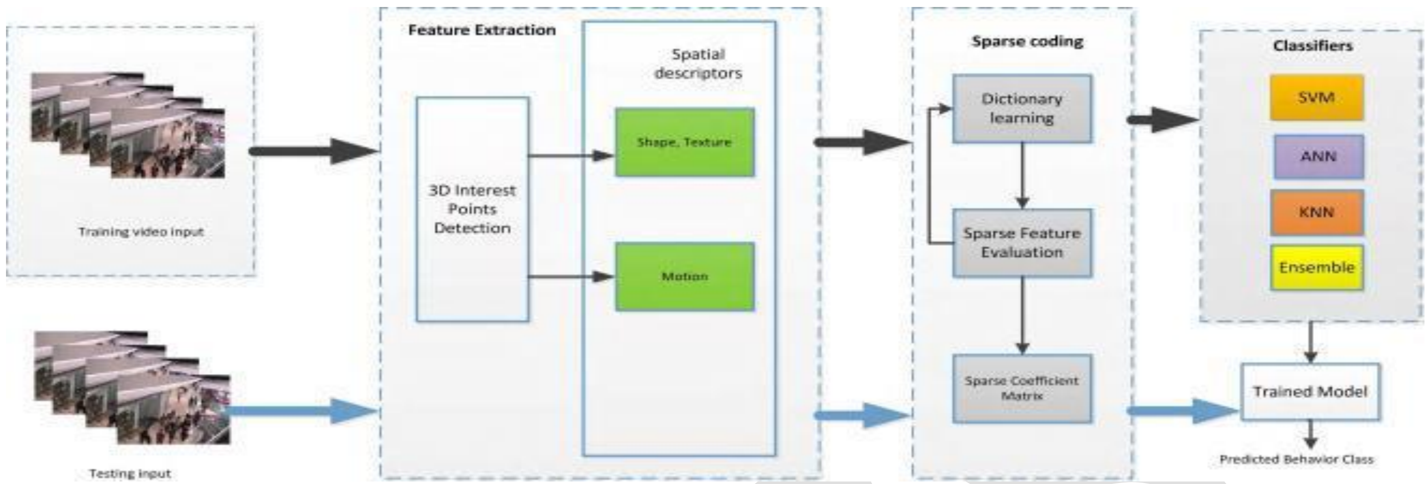

FIGURE 1. Schematic flow pattern of crowd behavior analysis.

The interest points give sign cant information on video data. They provide a compact video representation and tolerance to background clutter, occlusions and scale change. The extracted features are used in training and evaluation of specific behaviors. Appearance and motion features are obtained by computing HOF descriptor and HOG descriptor in the dense grid. It is worth mentioning that this approach does not require tracking. The motives behind the HOGHOF is that local object appearance, shape, and motion information can be effectively computed by a distribution of local intensities. This is implemented by dividing the video sequence into 3D patches 1x, 1y, and 1of spatial regions (cells). Each volume is further divided into *n* tx, *n* y, and *n*. grid of cuboids, then coarse HOG and HOF are extracted for each sub-volume segment. Then normalized histograms are concatenated into HOG, HOF and HOGHOF feature descriptor vectors and are closely alike to the well-known scale invariant feature transform descriptor. T The STIP is based on Harris 3D detector and dense detector. In the spatial domain `*s*' an image `*f* ' can be model in space-time domain by its corresponding linear scale representation. The convolution of *f* with Gaussian kernel of scale parameters `_21' and `_21 is given in Eq. (1).*L*_*x*; *y*; *t* I _2; _2_D *g*_*x*; *y*; *t* I _2; _2__ *f*.*x*; *y*; *t*(1)Where `_' denote the convolution sign and *L* is the Gaussian operator obtained at local scale. The spacetime second moment is computed using the relation:_.:I _; _/D *g*.O*L*(:I *s*_; *s*_/) __O*L*.:I _; _/where O*L* is the space-time derivative. Interest points are detected based on local maxima *H* corresponding to positive values *H* > 0 as given in:*H* D *det*/ *ktrace*3*T*._/.*H* D _1C _2 *k*._C _2/2.

Algorithm for behaviour recognition from input video.

1:Read video data.
2:n← number of videos in the dataset.
3: for (v:= 1 to n,v++) do
4: [I]<- detect interest Point(v)
5: for each i€[I] do
6: patch ←extract Patch(i)
7: [hog] ←extract HOG(Patch)
8: [hof] ←extract HOF(Patch)
9: Desct(v,i) ←(hog+hof)
10: end for
11: end for
12: for ←1,2,_ _ _ ,p do
13: D_k←[Desct]y
14: v_i← TrainedSparseDictionary
15: v_i← histogram(v_i)
16: v_i←normalized(v_i)
17: end for

ISSN 2091-2730

18: model ⟵ TrainClassifier(V)

19: Evaluate the trained Model

B. SPARSE MODELING REPRESENTATION

The aim of sparse coding is to locate an effective method of images pattern illustration by fusion of multiple features selected from a dictionary. Given a sparse dictionary matrix *D* D *d* that contains *K* atoms as column vectors *d*, the sparse coding problem of extracted HOG-HOF video descriptor *T* (HOG,HOF,HOGHOF) can be stated sanding the sparsest vector *y* such that *T* is approximately as *Dy*. A signal *T* can be represented by the linear combination of atoms;1; *d*2; : : : *dT nn*X1*yDn*_12_.1C_/D *Dy* (5) Where *n* is the total number of sparse dictionaries, *y* is the sparse code representation (mostly zeros entries) of T over D. The procedure to solve *y* is called sparse decomposition. The system of linear Eq. (5) is ill-posed and has no unique solution; however,, if *y* is sparse or approximately sparse, it can be uniquely determined by solving the following Optimization problem:*y* D*minyk*y*k*0*subject to*k*T Dy*k Where k_k represents the *lp*2 *norm* operator and _ is the reconstruction error of the signal *T* using the dictionary *D* and the sparseness code vector *y*. The combinatorial problem associated with Eq. (6) is NP-hard [38], so it is impossible to solve this problem by analyzing all possible sparse subsets. There are two types of methods to solve this problem. The first is the greedy algorithms [50], [51]; the second method relaxes the highly discontinuous *l norm*, replacing it by a continuous or even smooth approximation. Typically, when *l*00 *norm* is used, the problem becomes D*miny*k*T Dy*k2 *subject to*k*y*k0 where _ indicates the sparsity level. This convex minimization problem can be cast as a least squares problem with a penalty.

C. VIDEO CLASSIFICATIONS WITH SPARSE CODED FEATURES

As stated, sparse coding process follows immediately after the extraction of 3D spatio-temporal interest points and HOG, HOF, HOGHOF descriptors. The sparse representation is to learn a dictionary that captures vital and discriminative features of the video scenes. SCKSVD is employed for dictionary learning process.

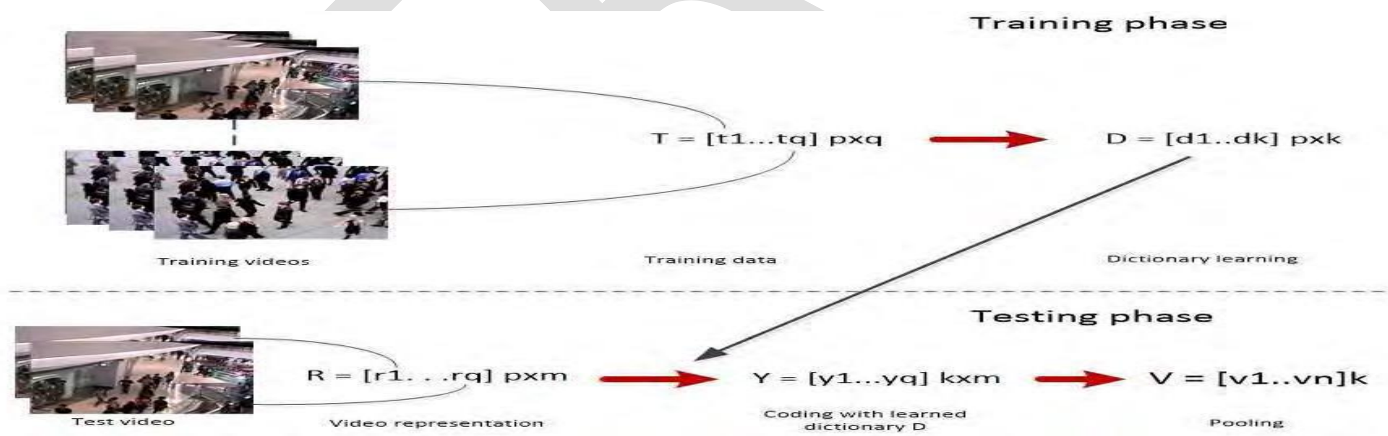

FIGURE 2. Pipeline for feature extraction and sparse coding technique.

The dictionary is learn from low-level features obtained from the training video data. Literatures have shown that using sparse representation method to video descriptors can reveal high-level of discriminated features. In this work, we resize the input videos to size 120 _ 160 resolution. The following low-level feature descriptors are extracted from the video scene:

HOG: Histogram of Oriented Gradient (HOG) are extracted over a regular grid on each frame of the video. In our evaluation, each video sequence is split into 3 _ 3 _ 2 grid cells with parameters *n* D 3, *n y* D 3, and *n* D 2 and 4-bin, a descriptor dimension 72 is extracted. The choice of the grid scale is motivated by the reduced computational complexity.

HOF: Histogram of Optical Flow (HOF) are extracted over regular grid as computed for HOG, with *n x* D 3, *n* D 3, and *n* D 2 and 5-bin. For every frame, we extract a feature vector of dimension 90.*t*

HOG-HOF: This is the overall concatenation of the aforementioned extracted features. For every frame sequence, we have 72 C 90 D 162 extracted feature vector.

The vector y comprises the representation coefficients of the feature descriptor signal *T* w.r.t. the dictionary *D*. The main problem encountered in practical applications is the choice of dictionary size *D*. One can use a pre-determined and fixed dictionary size as commonly used in wavelets, curve lets, and steerable _liters transforms. It is imperative to use varying dictionary size for a given set of training data in order to justify the number of atoms that give best performance measures. For each extracted feature type, they are arranged in the column of a matrix *T* D [*t*], where each *ti*1*y*; : : : *t*is a feature vector and q is the total number of the local patches in the training and testing videos. A dictionary *D* D [*d*] is learnt with K-SVD algorithms [33], where *k* is the size of the visual dictionary. A test video can be coded with the learnt dictionary *D* by creating a feature matrix *R* D [*r*11; : : : *d*; ::*rqk*] with a set of low-level features from the video descriptors.

EXPERIMENTS AND RESULTS

In this section describe the evaluations of sparse coding technique with STIPs 3D feature descriptors, and presents the results for combined descriptors:HOG-SCKSVD, HOFSCKSVD, and HOGHOF-SCKSVD for video classifications. In particular, it show the discrimination between crowd walking, crowd crossing and crowd merging, intervened escalator, smooth escalator etc. using sparse coding and bag-of-visual-features representation.

The dataset is split based on Leave-One-Out (LOO) cross validation scheme. It is apply in order to optimize the sparse coefficients matrix. The analysis is repeated over all the training set in each case by leaving one sample out for testing. The training group is used to build SVM classifier and the testing group is used to calculate the performance of the classifier. The performance evaluation is carried out in terms of classification accuracy, sensitivity and specificity accuracy, recall and precision. They are regarded as more appropriate than other statistical metrics in performance evaluation on common platform.

Performance evaluation is computed using confusion matrix. Confusion matrix comprises of actual and predicted classifications with the following components: True Positive(*TP*), False Positive (*FP*), False Negative (*FN*), and True Negative (*TN*) as presented in contingency. Accuracy is given by the total number of correct prediction. The True Positive Rate (*TPR*) also called Sensitivity or the Recall is the proportion of actual positive classes that were correctly identified. The Precision also called Positive Predictive Value (*PPV*) is the proportion of predicted positive cases that were correct. The True Negative Rate (*TNR*) also known as Specificity is referred to the proportion of negatives cases that were classified correctly.

$$\text{Accuracy} = \frac{TP + TN}{TP + FP + TN + FN}$$

$$\text{Recall} = \frac{TP}{TP + FN}$$

$$\text{Precision} = \frac{TP}{TP + FP}$$

The performance analysis of the sparse coding is presented for STIPs feature descriptors. It carry out different experiments, and in each case LOO cross validation with linear SVM is used. The dataset is randomly divided into (*n* - 1) clusters, and the visual dictionaries are learn with (*n* - 1) clusters in each case by testing on one set. The analysis is repeated for total number of videos *n* times using both training and testing videos and the mean classification result is recorded by taking the average. As stated in pedestrian sample frames , then eight classes of pedestrian attributes, compute the classification result for each behaviour classes.

CONCLUSION

This paper proposed an approach that combines spatio-temporal feature descriptors of crowd scenes with sparse coding model. The sparse signal representation techniques was used to detect robust features of crowd scenes and produce discriminant descriptors for classification between videos containing different behaviour classes. The proposed technique achieves higher performance than other feature extraction schemes such as bag-of-visual features approaches and deep learning approaches. Experimental results was tested on three publicly available datasets (CUHK, UCF and Crowd-UTP). The statistical paired test comparing the average accuracies of both the hand-designed and deep learning-based approaches shows that there was no difference in the result obtained from the techniques on CUHK, UCF and Crowd-UTP datasets. It obtained excellent and comparable classification results on all the datasets. In particular, using a dictionary of size 1000 and a linear SVM with sparse coded features, the method achieves better results in terms of accuracy, precision and recall for all the behaviour classes. The model proposed in this study will be of useful help in the area of crowd surveillance and monitoring. The proposed model is built based on eight (8) attributes of crowd videos, which restrict prediction of behaviours outside the scope of the datasets. It intend to extend to 3D adaptive features learning approach with large attributes dataset to accommodate broader prediction of behaviour classes.

REFERENCES:

[1] S. Ali and M. Shah, ``Floor fields for tracking in high density crowd scenes," in *Proc. Eur. Conf. Comput. Vis. (ECCV)*, 2008, pp. 1-14.

[2] S. Ali and M. Shah, ``A lagrangian particle dynamics approach for crowd flow segmentation and stability analysis," in *Proc. IEEE Conf. Comput. Vis. Pattern Recognit. (CVPR)*, Apr. 2007, pp. 1-6.

[3] X. Cai, W. Zhou, L. Wu, J. Luo, and H. Li, ``Effective active skeleton representation for low latency human action recognition," *IEEE Trans. Multimedia*, vol. 18, no. 2, pp. 141-154,Feb. 2016.

[4] A. Chan and N. Vasconcelos, ``Modeling, clustering, and segmenting video with mixtures of dynamic textures," *IEEE Trans. Pattern Anal. Mach. Intell.*, vol. 30, no. 5, pp. 909-926, May 2008.

[5] W. Choi and S. Savarese, ``A uni_ed framework for multi-target tracking and collective activity recognition," in *Proc. Eur. Conf. Comput. Vis. (ECCV)*, 2012, pp. 1-6.

[6] J. C. S. J. Junior, S. R. Musse, and C. R. Jung, ``Crowd analysis using computer vision techniques," *IEEE Signal Process. Mag.*, vol. 27, no. 5, pp. 66-77, Sep. 2010.

[7] V. J. Kok, M. K. Lim, and C. S. Chan, ``Crowd behavior analysis: A review where physics meets biology," *Neurocomputing*, vol. 177, pp. 342-362, Sep. 2015.

[8] D. Kuettel, M. Breitenstein, L. van Gool, and V. Ferrari, ``What's going on? discovering spatio-temporal dependencies in dynamic scenes," in *Proc. IEEE Conf. Comput. Vis. Pattern Recognit. (CVPR)*, Apr. 2010, pp. 1-6.

[9] R. Li, R. Chellappa, and S. K. Zhou, ``Recognizing interactive group activities using temporal interaction matrices and their Riemannian statistics," *Int. J. Comput. Vis.*, vol. 101, no. 2, pp. 305-328, 2013.

[10] W. Liu, R. Lau, and D. Manocha, ``Robust individual and holistic features for crowd scene classi_cation," *J. Pattern Recognit.*, vol. 58, pp. 110-120, Apr. 2016.

[11] V. Mahadevan, W. Li, V. Bhalodia, and N. Vasconcelos, ``Anomaly detection in crowded scenes," in *Proc. IEEE Conf. Comput. Vis. Pattern Recognit. (CVPR)*, Sep. 2010, pp. 1975-1981.

[12] R. Mehran, A. Oyama, and M. Shah, ``Abnormal crowd behavior detection using social force model," in *Proc. IEEE Conf. Comput. Vis. Pattern Recognit. (CVPR)*, Sep. 2009, pp. 935-942.

[13] B. Morris and M. Trivedi, ``Learning and classi_cation of trajectories in dynamic scenes: A general framework for live video analysis," in *Proc. IEEE Adv. Video Signal-Based Surveill.*, Apr. 2008, pp. 154-161.

[14] Y. Nam, S. Rho, and J. H. Park, ``Intelligent video surveillance system:3-tier context-aware surveillance system with metadata," *Multimedia ToolsAppl.*, vol. 57, no. 2, pp. 315-334, 2012.

[15] B. Pogorelc, and M. Gams, ``Detecting gait-related health problems of the elderly using multidimensional dynamic time warping approach with semantic attributes," *Multimedia Tools Appl.*, vol. 66, no. 1, pp. 95-114, 2013.

[16] A. Saad, ``Measuring _ow complexity in videos," in *Proc. IEEE Int. Conf. Comput. Vis. (ICCV)*, 2013, pp. 1097-1104.

[17] A. N. Shuaibu, A. S. Malik, and I. Faye, ``Behavior representation in visual crowd scenes using space-time features," in *Proc. 6th Int. Conf. Intell. Adv. Syst. (ICIAS)*, Kuala Lumpur, Malaysia, Sep. 2016, pp. 1-6.

[18] X. Wang, K. Ma, G. Ng, and W. Grimson, ``Trajectory analysis and semantic region modelling using nonparametric hierarchical Bayesian models," *Int. J. Comput. Vis.*, vol. 95, no. 3, pp. 287-312, 2011.

[19] H. Wang, M. M. Ullah, A. Klaser, I. Laptev, and C. Schmid, ``Evaluation of local spatio-temporal features for action recognition," in *Proc. Brit. Mach. Vis. Conf.*, 2009, p. 12411.
[20] B. Zhou, X. Wang, and X. Tang, ``Understanding collective crowd behaviors: Learning a mixture model of dynamic pedestrian-agents," in *Proc. IEEE Conf. Comput. Vis. Pattern Recognit. (CVPR)*, 2012, pp. 1-8.

Comparative study of co-digestion of composted mixtures of cassava peels and coffee pulp with or without cow dung.

Nkodi* T.M[1], Kayembe J.S[2]., Biey M. E [3].and Taba K.M[2]
[1]Department of Petrochemistry, Faculty of Gas, Oil and New Energies, University of Kinshasa.
[2]Department of Chemistry and Industry, Faculty of Sciences, University of Kinshasa
[3] Department of environment sciences, Faculty of Sciences, University of Kinshasa.
Corresponding Author: E-mail: nkoditimothee@gmail;com,

Abstract- This work aims to study co-digestion of composted mixture of cassava peels and coffee pulp with cow dung .Cassava peels was mixed with coffee pulp in the following ratios by weight, 1:1, 3:1, 1:3, Cassava peels alone (1:0) and coffee pulp alone (0:1) served as controls. The mixtures and controls were submitted to composting for 30 days then placed in five digesters C1 for 1:1 blend,C2 for 3:1 blend,C3 for 1:3 blend , C4 for cassava peels alone and C5 for coffee pulps alone. Another batch of five digesters consisting of each composted mixture of cassava peels and coffee pulps to which was added equal amount of cow dung labeled as follows: CB1, CB2, CB3, CB4 and CB5. Biodigestion was conducted under mesophilic conditions into 5L biodigesters with a loading rate of 5% of total solids. Biogas production was measured by using water displacement method for 35 days. The highest cumulative volume of biogas was produced by composted mixture with cow dung and the yield decreased in the following order 16.50, 15.38, 15.07, 12.68 and 10.97L/KgTS respectively for CB3>CB1>CB5>CB2>CB4. The composted mixture alone yielded the following amount of biogas: 10.26, 9.11, 8.86, 7.50, and 7.07L/KgTS respectively for C1, C5, C4, C3 and C2. Co-digestion of the composted mixture of cassava peels and coffee pulps with cow dung can be considered as a good system to enhance biogas production from cassava peels.

Key words: biomethanization, cassava peels, coffee pulp, co-digestion, biogas.

1. Introduction

The rapid growth of World population lead to fast urbanization, increase industrialization, waste generation and energy consumption (Ojolo et al., 2007, Sun and Cheng 2002, Subramani and Ponkumar, 2012). To feed the growing population, agriculture and animal production have to be increased (Habtamu Lemma, 2014) and consequently the generation of large amount of organic solid wastes. These improperly manage leads to uncontrolled dumping and create serious environment problems (Oparaku et al., 2013; Ojolo et al., 2007).

One way in which energy consumption and organic solid waste management problems could be solved is by biomethanization to produce biogas and digestate. Biogas has about 55 to 65% of methane gas and 30 to 45% of carbon dioxide. Biogas can be used as replacement of natural gas in industrial and domestic consumption whereas digestate obtained from anaerobic digestion, could be used as fertilizer for crops and vegetables, as feed for fish ponds and livestock and as material to produce charcoal briquette (Akwaka et al., 2014; Lennart and Anne, 2013).

Cassava (*Manihot Esculenta Grats*) is the main source of carbohydrates for human population in Sub-Saharan Africa (Oparaku at al., 2013). DR Congo is the second producer in Africa after Nigeria. In the process of cassava roots, wastes (mostly peels) which constitute one third of the weight of the roots are discarded.

Of the many ways to recycle cassava peels, anaerobic digestion is considered a major promising process. Adelekan and Bamgboye (2009) reported that cassava peels alone produced less biogas than when it's mixed with animal manure and biogas yield depended on the type of manure and on the ratio of cassava peels to the livestock wastes. They showed that the highest cumulative yield of biogas (21.3L/kgTS) was achieved by mixing cassava peels with cow waste in a ratio of 1:1, whereas cassava peels alone produced 0,6L/KgTS.

We reported recently biodigestion of cassava peels with various amount of urea. The highest biogas yield (80.82L/KgTS) was obtained with 0.01% of urea mixed with cassava peels (Nkodi et al., 2016). Co-digestion of cassava waste with agriculture biomass waste have received less attention, therefore, we set here to investigate co-digestion of cassava peels with coffee pulp in different ratio for biogas generation.

Coffee is among the largest export agriculture products of DR Congo. The process of coffee leaves a large amount of waste (80,000 tons /yearly) which is discarded. It is reported that composting coffee pulp prior to its digestion achieved large amount of biogas (Taba et al., 1999). Coffee pulp compost could be obtained in 20 days while in the due process the C/N ratio value decreases from 43.4 to 22, a value favorable for biodigestion (Kayembe et al., 1999).

Hence, in this work cassava peels and coffee pulp were mixed in different ratio and composted for 30 days prior to anaerobic digestion. Then to each of the composted mixture was added equal amount of cow dung. The obtained mixtures of these three wastes (cassava peels, coffee pulp and cow dung) were also submitted to anaerobic digestion.

2. Materials and methods

2.1. Material

Cassava peels were collected from Mbanza-Lemba (Kinshasa) market and pretreated as previously reported to remove cyanide (Nkodi et al., 2017). Coffee pulp was obtained from the African Coffee Company in Kinshasa/Kingabwa. Cow dung was obtained from the slaughterhouse in Masina/ Kinshasa and kept in cold until used. Standard methods were used to determine the proximate composition of materials (pH, moisture, total solids, organic matter, organic carbon and ash) before and after composting.

2.2. Composting

Cassava peels (CaP) were mixed with coffee pulp (CoP) in the following ratios 1:1 (CaP/CoP), 3:1 (CaP:CoP) and 1:3(CaP/CoP) by weight. Cassava peels alone (1:0) and coffee pulp alone (0:1) with the same total solids weight as the mixture, served as control. Each mixture and the controls were placed in polyethylene bags of 10L and composted for 30 days as described by Kayembe et al. (1999).

Composted mixture of Cassava peels and Coffee pulp were then put in five digesters labeled as followed C1 for 1:1 mixture, C2 for 3:1 for mixture, C3 for3:1 mixture, C4 for cassava peels alone (1:0) and C5 for coffee pulp alone (0:1).

To another part of each composted mixture and controls was added equal amount of cow dung by weight (1:1) and placed in the following five digesters labeled as followed, CB1 for 1:1 composted mixture (CaP/CoP), CB2 for the 3:1 composted mixture CaP:CoP),CB3 for the 1:3 composted mixture (CaP:CoP),CB4 for composted cassava peel alone and CB5 for composted coffee pulp alone. The different digesters composition are shown in table 1

Table 1: Composition of various digesters

Ratio CaP:CoP (gTS/gTS)	Digesters	Ratio CO:CD (gTS/gTS)	Digesters
1:1	C1	1 :1	CB1
3:1	C2	1 :1	CB2
1:3	C3	1 :1	CB3
1:0	C4	1 :1	CB4
0:1	C5	1 :1	CB5

CaP: cassava peels, CD: cow dung, CoP: coffee pulp, CO: compost and gTS: gram of total solids.

2.3. Biogas production essays

Each of the ten digesters had a working volume of 5L; the slurry was made with distilled water and then loaded to about three quarter of working volume to achieve 5% of total solids (TS). Digesters were shaken manually twice daily, morning and evening and the volume of biogas produced was measured by water displacement method. Experiments were conducted in mesophilic conditions and the retention time dependent on the essays. Each experiment was carried out in triplicate

3. Results and discussion

A. Physico-chemical properties of substrates

The physico-chemical parameters of feedstock are presented in tables 2, while those of mixture before and after composting are shown in tables 3 and 4 respectively.

Table 2: Physicochemical properties of feedstock

Parameter	Cassava peels	Coffeepulp	Cow dung
pH	5.30± 0.31	7.13±0.32	8.13±0.55
Moisture (%)	12.16 ±0.73	12.63±2.62	80.59±0.81
Total solids (%)	87.84±0.73	87.37±2.62	19.41±0.77
Organic matter (%)	95.98±0.28	91.88±0.32	88.56±5.90
Organic carbon Total (%)	53.32±0.16	51.04±0.18	49.20±3.39
Ash (%)	4,03±0,28	8,12±0,32	11.44±5.90

Cassava peels have acidic pH due most likely to the presence of cyanogenic glycosides (Cuzin et al.1992; Ofoefule and Uzodimna, 2009), cow dung has a slightly basic pH (8.13) and coffee pulp have a neutral pH of 7.13 (Table 2). Total solids and ash obtained from the substrate are closed to those reported by other researchers (Steiner, 2011; Habtamu, 2014 and Corro, et al., 2013). According to Steiner (2011), coffee pulp can be digested as mono-charge without inhibiting the process and it is a good bioresource for methane generation because of its high nutrient content.

Table 3: Physicochemical properties of cassava peels blended with coffee pulp before composting

Composter / Parameter	C_1(50%CaP)	C_2(75%CaP)	C_3(25%CaP)	C_4(100%CaP)	C_5(0%CaP)
pH	6.2±0.20	5.5±0.1	6.7±0.1	5.2±0.1	6.9±0.2
Total Solids (%)	77.59±0.10	82.56 ±1.17	78.56±1.48	87.84 ± 0.73	87.33± 2.59
Organic Matter (%)	93.03 ±0.27	93.95±0.78	91.98± 0.40	95.98 ± 0.28	91.88±0.32
Org. Total Carbon (%)	51.68±0.15	52.19±0.45	51.09± 0.23	53.32 ± 0.16	51.04±0.18
Ash (%)	6.97± 0.27	6.05±0.78	8.02±0.40	4.02± 0.28	8.12±0.32

Table 4.Physicochemical properties of cassava peels blended with coffee pulp after composting

Compost / Parameter	C_1(50%CaP)	C_2(75%CaP)	C_3(25%CaP)	C_4(100%CaP)	C_5(0%CaP)
pH	8.4± 0.1	9.0±0.1	7.8±0.1	9,1±0.1	8.5±0.1
Total Solids (%)	71.8 ±3.25	79.05±0.48	74.12±10.2	84.11±0.86	55.64±0.98
Organic Matter (%)	68.01±0.44	69.05±0.18	64.19±0.11	62.00±0.92	80.01±0.15
Org.Total Carbon (%)	37.78±0.25	38.36±0.10	35.66±0.06	34.44±0.53	44.45±0.09
Ash (%)	31.99±0.44	30.95±0.35	35.81±0.11	38.00±0.92	19.99±0.15

Physicochemical parameters of cassava peels mixed with coffee pulp before and after composting are shown in tables 3 and 4. The pH of the mixture moved from neutral to slightly basic after composting, a favorable pH for biomethanisation. The change of pH was very remarkable for cassava peels alone with a change of about 4 units (5.2 to 9.1) It has been pointed out that change in pH could be an indication of bacterial activities during composting. The total organic matter decreased in all the composted mixtures whereas ash increased in the process of composting which is a clear indication of significant mineralization during the composting processes (Montgomery and Bochmann, 2014). The slight decrease in organic matters could be due to the low rate of hydrolysis in most biological pretreatment processes (Cheng, 2002). Thus, 30 days of composting could be deficient to allow bacteria to break down all the cellulose cristallinity in solid wastes used.

B. Comparative biodigestion of composted mixture of cassava peels and coffee pulp

The cumulative values of biogas produced from the ten digesters are reported in figure 1.

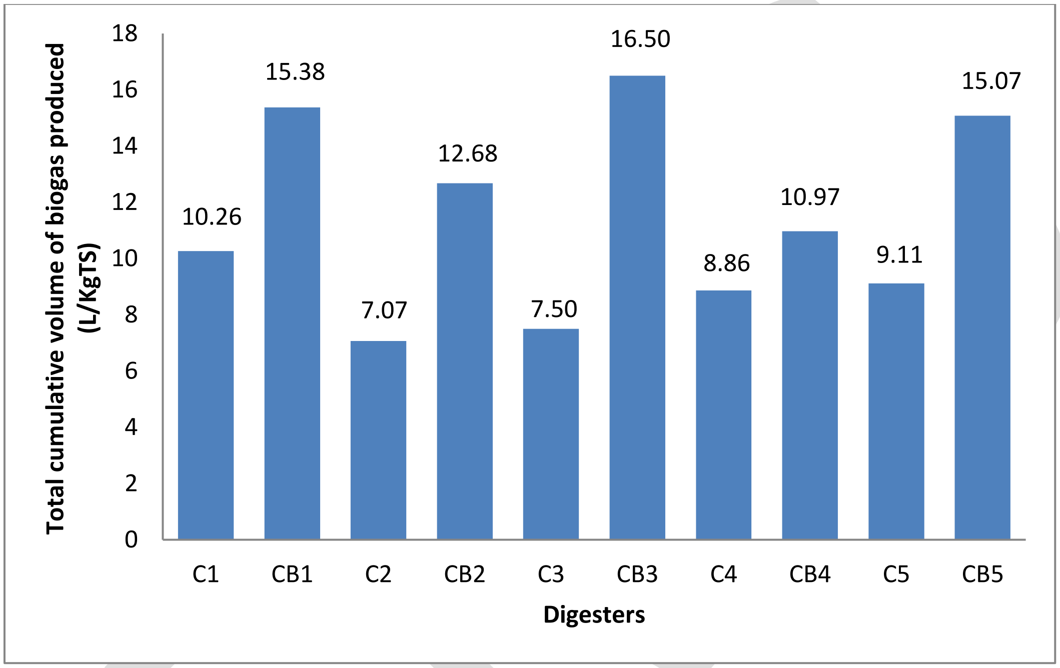

Figure 1. Cumulative volume of biogas produced from biodigesters of different composted mixture of cassava peels and coffee pulp with cow dung.

The cumulative volume of biogas was much higher for the composted mixture of cassava peels and coffee pulps blended with cow dung than the composted mixture alone. Cow dung improved the biogas yield in all the digesters. Composted cassava peels with coffee pulp gave higher biogas yield than the composted of cassava peels alone (C1>C4). This shows that co-digestion of cassava peels with coffee pulp give better results than cassava peels alone. Cassava peels alone gave less biogas than cassava peels mixed with cow dung or with its blend with coffee pulp and cow dung (C4<CB4 or C4<C1). Coffee pulp alone gave more biogas than cassava peels (C5>C4), their mixture with cow dung showed the same CB5>CB4. Increasing biogas production by co-digestion of animal manure to organic solid waste is well documented (Ezekoye Ezekoye (2009); Ofoefule and Uzodimna (2009), Oparaku and al. (2013)). Our results shows that digester CB3 produced the highest amount of biogas (16.50L/KgTS), followed by CB1 (15.38L/KgTS), CB5 (15.07L/KgTS), CB2 (12.68L/KgTS) and then CB4 (10.97L/KgTS). The biodigesters which produced the highest amount of biogas (CB3 and CB1) were made by 50% of compost and 50% cow dung respectively. The cumulative biogas obtained for composts alone decreased in the following order of the mixture (peels-coffee pulp): 1:1>0:1>1:0>1:3>3:1 respectively for digester C1>C5>C4>C3>C2. Digester C1 produced 10.26L/KgTS of biogas with a mean daily production of 0.29L/KgTS per day, while digesters C4 and C2 with higher quantity of cassava peels 100% and 75% respectively, produced 8.86 and 7.07L/KgTS respectively. It means that different combination of wastes can give different composition of nutrients (Oparaku et al., 2013). It is found that the yield of the digester CB1 were lower (15.38L/KgTS) than that of digester CB3 (16.50L/KgTS) containing (37.5% pulp;

12.5% peels; 50% dung) (Adelekan and Bamgboye (2009). The lower biogas production in digester CB1 could be due to the low presence of coffee pulp (25%), rich in nutrients (C: 58.5%, N: 1.3%), (Pujol, D. et al., 2013).

4. Conclusion

In this work, two set of experiments were carried out for producing biogas: composted mixture of cassava peels and coffee pulp alone and then composted mixture with cow dung by varying quantities. The combination of compost with cow dung yielded the largest volume of biogas on the cumulative basis than the compost alone. After 35 days of digestion, the highest cumulative volume of biogas flammable at the 4^{th} day was produced by the compost mixed with cow dung and the cumulative yields were 16.50, 15.38, 15.07, 12.68 and 10.97L/KgTS respectively for CB3>CB1>CB5>CB2>CB4. However, composts alone produced biogas in the following order 10.26, 9.11, 8.86, 7.50 and 7.07L/KgTS respectively for C1, C5, C4, C3 and C2. This work showed that co-digestion of composted mixing of cassava peels and coffee pulp give more biogas than any single substrate antd that addition of cow dung to composted mixture improve tremendously of biogas production.

REFERENCES:

1. Akwaka, J-C., Kukwa, D.T. and Mwekaven, S.S. (2014). Preliminary study on co-digestion of cow manure with pretreated sawdust for production of biogas and biofertilizer. IJST, vol.(3):4, pp.222-228.
2. Corro G., Paniagua L., Umapada P., Bañuelos F. and Minerva R. 2013. Generation of biogas from coffee-pulp and cow-dung co-digestion: Infrared studies of postcombustion emissions. Energy Conversion and Management, 74: 471–481
3. Corro, G., Umapada Pal & Surinam Cebeda. (2014). Enhanced biogas production from coffee pulp through deligninocellulosic photocatalytic pretreatment. Energy science & Engineering published 2(4):177-187.
4. Esposito, G., Frunzo, L.; Liotta, F.; Panico, A.; Pirozzi, F. (2012). Bio-Methane potential tests to measure the biogas production from the digestion and co-digestion of complex organic substrates. Open J.Environ. Eng. 5: 1-8.
5. Estevez, M.M., Linjordet, R., and Morken, J. (2012b). Effects of steam explosion and co-digestion in the methane production from Salix by mesophilic batch essays. Bioressour.Technol. 104, 749-756.
6. Ezekoye, V.A. and Ezekoye, B.A.(2009). Characterization and storage of biogas produced from the anaerobic digestion of cow dung, spent grains/cow dung and cassava peels/rice husk. The Pacific Journal of Science and Technology, vol.10 (2), pp.898-904.
7. Habtamu Lemma Didanna, (2014).A critical review of feed value of coffee waste for livestock feeding. World Journal of Biology and Biological Sciences Vol. 2 (5), pp. 072-086.
8. Kayembe S.,Yengula H.M., Ndunga D., Litanga J., Taba K.M., (1999). Compostage contrôlé des parches de café, Med.Fac.Landbouww, Univ.Gent ; 64/1,281-284.
9. Montgomery, L.F.R. and Bochmann, G. (2014). Pretreatment of feedstock for enhanced biogas production.IEA Bioenrgy.
10. Mshandete, A., Bjornsson, L., Kivaisi, A.K., Rubindama-Yugi, M.S.T., Mattiasson, B. (2006). Effect of particle size on biogas yield from sisal fibre waste.Renewable Energy 31, 2385-2392.
11. Nkodi T.M., Taba, K.M., Kayembe, S., Mulaji, C. and Mihigo, S. (2016). Biogas production by co-digestion of cassava peels with urea. IJSET, vol.(5):3, pp.139-141.
12. Ofoefule, A.U and Uzodimna, E.O. (2009). Biogas production from blends of cassava (Manihotutilissima) peels with some animal wastes. International Journal of Physical Sciences, Vol.4 (7), pp.398-402.

13. Ojolo, S.J., Dinrifo, R,R. and Adesuyi, K.B. (2007). Comparative study of biogas production from five substrates.Advanced Materials Research Vols 18-19, pp.519-525.
14. Oparaku, N.F, Ofomatah, A.C and Okoroigwe, E.C. (2013). Biodigestion of cassava peels blended with pig dung for methane generation. African Journal of Biotechnology. Vol.12 (40), pp. 5956-5961.
15. Pujol, D., Liu, C., Gominho, J., Olivella, M.A., Fiol, N., Villaescusa, I. and Pereira, H. (2013). The chemical composition of exhausted coffee waste. Industrial crops and products, 50: 423-429.
16. Steiner, R. (2011). Biogas production of coffee pulp & waste waters. Renewable Energy & Energy Efficiency promotion in international cooperation.
17. Subramani, T. and Ponkumar, S (2012). Anaerobic digestion of aerobic pretreated organic waste. International Journal of modern Engineering Research, vol.2, issue.3, pp.607-611.
18. Sun, Y and Cheng J. (2002). Hydrolysis of lignocellulosic materials for ethanol production: a review. Bioressource Technology 83, pp.1-11.
19. Taba K.M., kayembe S., Mutombo L.D., Nzita N. (1999). La biométhanisattion des déchets de café pré- compostés ; Med.Fac. Landbouww. Univ. Gent : 64/1, 174-176.

International Journal of Engineering Research and General Science Volume 6, Issue 2, March-April, 2018
ISSN 2091-2730

TOTAL CONSOLIDATION SETTLEMENT OF A LOCAL SOIL IN THE FIELD CONDITION (LABORATORY INVESTIGATION)

Dhirendra Kumar Singh[1], Shashi Shekhar Singh[2]

Associate Professor, Department of Civil Engineering, IEC College of Engineering and Technology, Greater Noida, India[1]

Associate Professor, Department of Civil Engineering, Madda Walabu University, Bale Robe, Ethiopia [2]

india_dhirendra@yahoo.co.in, +919958429844[1]

Abstract— Estimating consolidation settlement, and the rates at which they will occur, plays an important part in many civil engineering projects. Accurate predictions of settlement magnitudes require accurate evaluations of soil properties and pre consolidation pressure. Accurate predictions of settlement rates require improved methods to take into account important factors such as variations in 'cv' within clay layers, nonlinear stress-strain behavior, and non uniform strain profile effects, and research to develop an improved model of soil compressibility that can determine the accurate value of total consolidation settlement of soil in the field condition. This study also tries to develop a model of soil layer and to determine accurate value of total settlement. A laboratory investigation on consolidation settlement has been done. For this purpose a soil bed was made in a model tank and consolidated by applying some pressure. The determination of total settlement by making model of soil bed and doing direct loading on soil for consolidation is an approach to predict accurate total settlement of a soil.
Keywords: Consolidation settlement, Atterberg's limit constants, Clay Soil, Field Condition, Laboratory Investigation.

Introduction:
In this research determination of general soil properties of the local soil along with estimation of settlement of soil layered in the field condition. For this purpose fabrication and preparation of the laboratory set up of soil similar to a field condition, loading on the soil sample and determination of settlement with time.

Fabrication of the laboratory set up:
Two square boxes of 18' X 18' and 24' X 24' have been fabricated. All the boxes are made by fiber with appropriate shape. In each box, there are one out let in one face at a height of two inches from bottom are also made. This out let is used for flow of water from the box. One iron clamp for each small box is made for prevention of lateral expansion of the soil under the box. Similarly two iron clamps are used for bigger boxes for prevention of lateral expansion. In each small box at a height of 12 inches from bottom, there is one small circular hole in each face. Similarly in bigger boxes, the holes are made at the height of 16 inches. There is a scale, on each of the face of the all boxes from the bottom side of the boxes for the purpose of measurement of settlement of the soil layer.

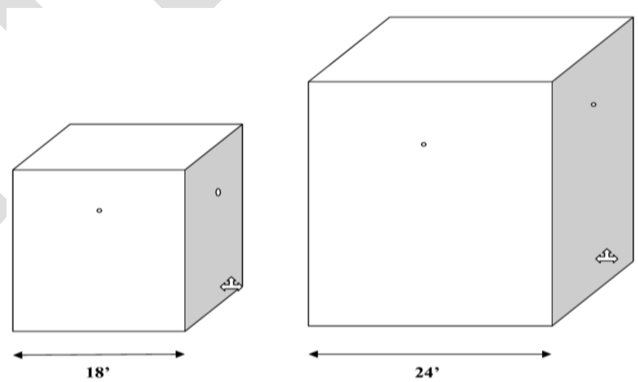

Fig. 1. Fabricated Smaller and Bigger Boxes.

Arrangement and Preparation of the soil (clay) sample:
The soil sample was collected from a pond in Balrampur village near IIT Kharagpur. The soil was cut from bottom of the pond. The 30 bags of soil were brought from that pond. The soil was mixed with organic fossils and undesirable matters. So it has been put in the

water tank and then it has been washed in water. All the undesirable materials with soil were removed by sieving the soil with a sieve. In this way obtained fresh soil sample is taken in a big tank. Soil water suspension with water content sufficiently more than the liquid limit of soil and natural water content were kept up to desired height for some time.

Determination of soil properties:

A. Determination of water content of the soil sample:

The water content of the soil sample just taken from the pond is determined by the oven dry method in the laboratory. For that small quantity of soil sample was taken in two cans and put in the electric oven for 24 hours for being dry. After 24 hours soil was weighed and water content of the sample has been determined. The water content of the sample was **65.45%.** This is the natural water content of the sample. Similarly when the clay was being put in the boxes again the water content of the respective clay of individual box has been taken.

B. Determination of Atterberg's limits constants:

For determining Atterber's limits constant the sample is prepared as accordance with BIS code 2720 part 1. Soil is first dried in the sun and later by oven between the temperatures 105^0c to 110^0c after that it has been powdered by using hammer. When soil is almost converted to dust, it is sieved by the 425 micron sieve. The Liquid limit of prepared soil sample is determined by the Mechanical method. Plastic limit is also determined by the BIS code 2720 part 5 methods. In the last shrinkage limit is determine by BIS 2720 part 6 methods. By using these methods the obtained data are as follow.

Table 1 Atterber's limits constant

Liquid limit of the soil	(W_L)	43%
Plastic Limit of the soil	(W_P)	21%
Shrinkage limit of soil	(W_s)	17%
Plasticity index	(I_p)	22%

From the Plasticity chart the soil sample is **Inorganic clays of low to medium plasticity (CL).**

C. Determination of specific gravity of the soil:

The specific gravity of the soil sample is determined by the IS 2720 part 3: section – 1:1980 or density bottle method. The specific gravity of the soil **G = 2.43.**

D. Determination of organic content of the soil:

The organic content of the soil sample is determined by the IS 2720 part 22: 1976. The percentage organic content in the soil is found 12.23 %. This data shows that the soil has low organic contents hence the soil have greater compatibility characteristics. It means it has high co-efficient of compression.

Table 2 Properties of Clay

Parameters	Value	Relevant IS codes
Classification	CL	IS : 1498-1970
Specific Gravity	2.43	IS:2720 (Part III)-1980
Liquid Limit	43%	IS:2720 (Part V)-1985
Plastic Limit	21%	IS:2720 (Part V)-1985
Plasticity Index	22%	IS:2720 (Part V)-1985
Shrinkage Limit	17%	IS:2720 (Part VI)-1982
Organic content	12%	IS:2720 (Part XXII)-1972

Preparation of Laboratory set up with the soil similar to field condition:

A. Process of preparation of soil layer

For the preparation of experimental set up similar to field condition following procedure has been done.

- The prepared soil sample is poured in to the box very slowly to a fixed height.
- The box was leaved for 15 days for squeezing out of the water from the soil and to settle the soil layer by self weight.
- After 15 days gravels were put on the soil layer slowly and uniformly, each day 3 inches heights, until the box is filled fully by gravel.
- The out let of the box is being closed after putting the gravel and each day the settlement of the soil layer is noted due to weight of gravel.
- After 20 days the settlement of the soil layer was become almost constant and some water is raised in gravel zone.
- Now for full saturation of the soil, the water is added very slowly from the top and uniformly up to the height of a hole in the box.
- Thus in this way a model of saturated soil layer under the layer of a gravel has been prepared in two tank which is ready for consolidation test.

Fig. 2. Model of soil sample prepared for consolidation test

B. Loading on the soil layer and settlement of the soil layer with time:

After completion of settlement under the self weight and gravel surcharge weight the external loads were placed for one dimensional consolidation of soil layer in single drainage condition. Before loading some water was added from the top to the boxes for keeping the soil fully saturated. Then the upper Portion of the gravel was leveled by the leveling device. A square iron plate had been put in the middle of the box. On this plate the concentric weights are loaded for the settlement purpose. Upon concentric loads a dial gauge of least count of 0.01mm is set for measuring settlement (Fig. 3 & Fig. 4). After just applying the load the settlement has been noted in the interval of 30 minutes, 1 hour, 2 hours, 4 hours, 6 hours and 24 hours. Then every day at a fixed time the settlement of clay has been noted up to when the settlement of clay becomes almost constant.

Table 3 Loading detail of the soil layer

Box	**Weight W (kg)**	**Area of plate A_S (m^2)**	**Load P (kN/m^2)**	**Ht. of clay H_t (cm)**
Smaller box	94.107	0.052	17.648	17.46
Bigger box	88.220	0.041	21.270	25.72

Fig. 3. Loading on the smaller box model

Fig. 4. Loading on the bigger box model

Settlement data of soil layer in the boxes:

After just applying the load on the soil, settlement was noted in the interval of 30 minutes, 1 hour, 2 hours, 4 hours, 6 hours and 24 hours. Then every day at a fixed time the settlement of soil was noted up to when the settlement of clay becomes almost constant. The settlement data of the soil of smaller box and bigger box are shown in the table 4 and table 5 respectively.

Table 4 Settlement of soil in smaller box

No. of Days	Dial Reading R (mm)	Difference from initial (mm)	Cumulative difference (mm)
1	4.90	0.00	0.00
2	3.05	1.85	1.85
3	2.40	0.65	2.5
4	1.86	0.54	3.04
5	1.33	0.53	3.57
6	0.92	0.41	3.98
7	0.76	0.16	4.14

8	0.58	0.18	4.32
9	0.44	0.14	4.46
10	0.32	0.12	4.58
20	-0.27	0.59	5.17
30	-0.69	0.42	5.59
40	-1.06	0.37	5.96
50	-1.32	0.26	6.12
60	-1.51	0.19	6.41
70	-1.68	0.17	6.58
80	-1.83	0.15	6.73
90	-1.95	0.12	6.85
100	-2.05	0.10	6.95

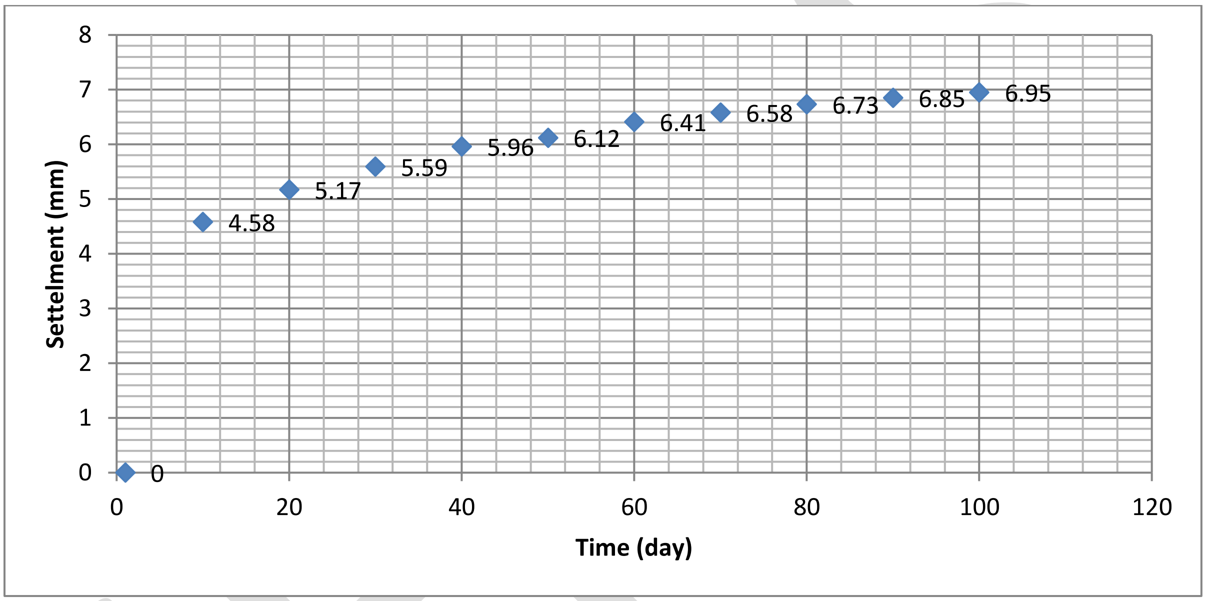

Fig. 5. Settlement in smaller box

Table 5 Settlement of soil in bigger box

No. of Days	Dial Reading R (mm)	Difference from initial (mm)	Cumulative difference (mm)
1	18.45	0.00	0.00
2	17.73	0.72	0.72
3	17.11	0.62	1.34
4	16.55	0.56	1.90
5	16.04	0.51	2.41
6	15.56	0.48	2.89
7	15.13	0.43	3.32
8	14.72	0.41	3.73
9	14.31	0.39	4.12
10	13.92	0.38	4.50
15	12.38	1.54	6.04
20	11.23	1.15	7.19
30	10.50	0.73	7.92
40	10.04	0.46	8.38
50	9.63	0.41	8.79

60	9.31	0.32	9.11
70	9.08	0.23	9.34
80	8.77	0.18	9.52
90	8.66	0.11	9.63
100	8.58	0.08	9.71

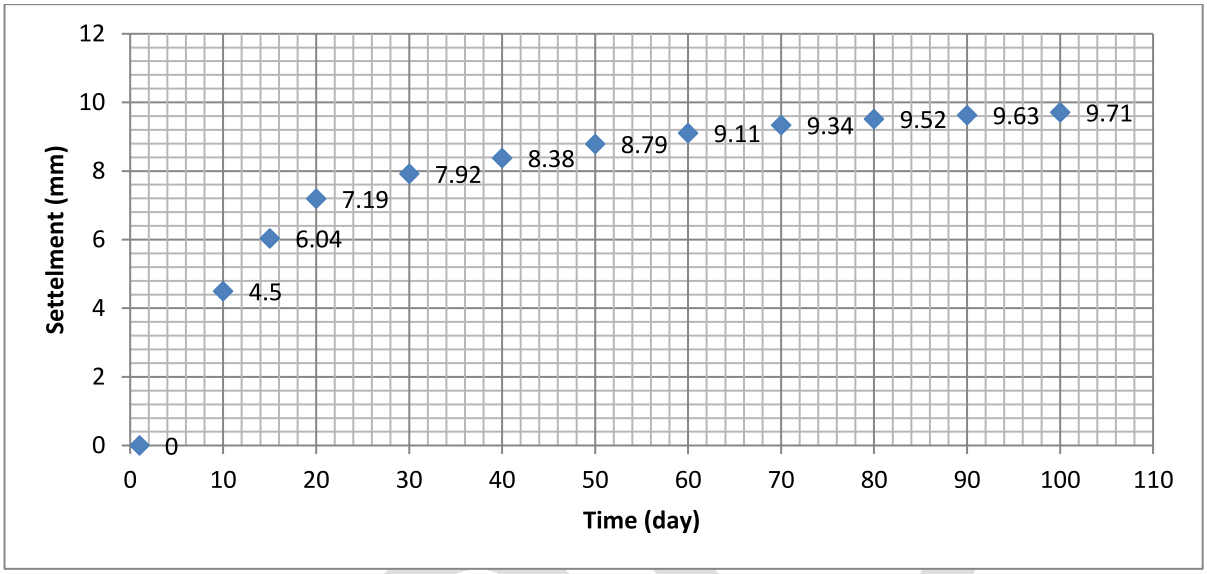

Fig. 6. Settelment in bigger box

Comparision of the data obtain:
On comparision of data obtained in table 4 and table 5, we can plot following graphs.

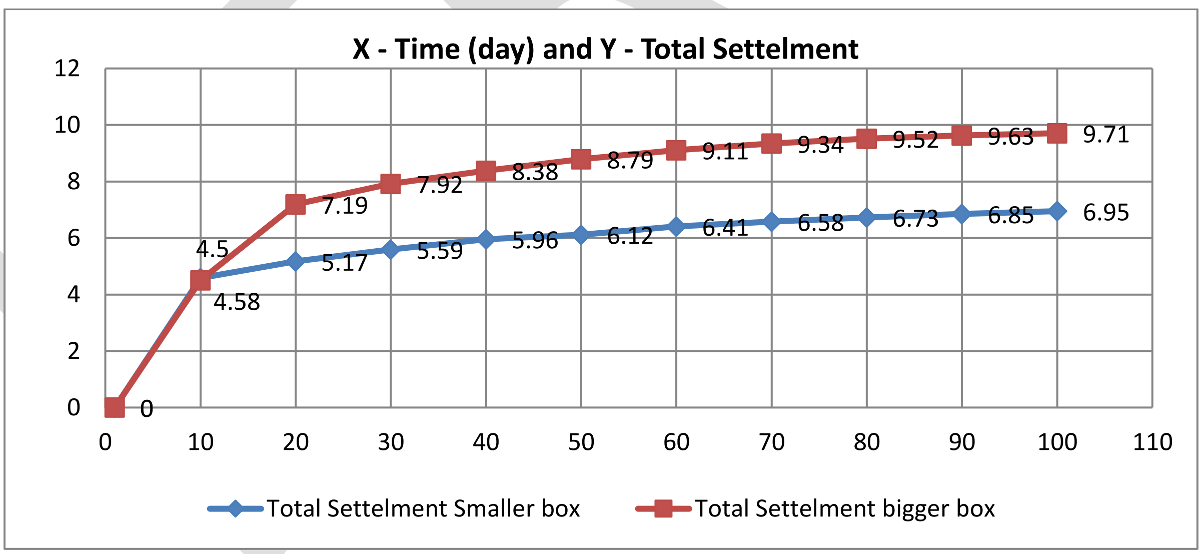

Fig 7 Comparative settlement in smaller and bigger boxes

Conclusions:
1. The settlement of clay soil in smaller box in 100 days is 6.95 mm
2. 70% of the total settlement of clay soil in smaller box in only 15 days.
3. The settlement of clay soil in bigger box in 100 days is 9.71 mm.
4. 75% of the total settlement of clay soil in bigger box in only 20 days.
5. At the 100 days the settlement of clay soil in both boxes stop or negligible.
6. Bigger box having 39.71 % more settlement than smaller box.

7. In First 10 day's settlement rate in both the boxes are approximately equal. After 10 days settlement rate increases in bigger box with respect to smaller box.
8. The settlement rate is more in first 10 days in both the boxes as compared to the other days.
9. This study ensures that this settlement data of soil by direct load settlement experiment in the laboratory can be used for designing of structure.

REFERENCES:

1. IS 2720 : Part 1 : 1983 Methods of Test for Soils - Part 1 : Preparation of Dry Soil Samples for Various Tests.
2. IS 2720 : Part 2 : 1973 Methods of test for soils: Part 2 Determination of water content.
3. IS 2720 : Part 3 : Sec 1 : 1980 Methods of test for soils: Part 3 Determination of specific gravity Section 1 fine grained soils.
4. IS 2720 : Part 5 : 1985 Method of Test for Soils - Part 5 : Determination of Liquid and Plastic Limit.
5. IS 2720 : Part 6 : 1972 Methods of test for soils: Part 6 Determination of shrinkage factors.
6. IS 2720 : Part XV : 1965 Methods of Test for Soils - Part XV : Determination of Consolidation Properties.
7. IS 2720 : Part 22 : 1972 Methods of test for soils: Part 22 Determination of organic matter.
8. Casagrande, A., Fadum, R.F., 1940. Notes on Soil Testing for Engineering Purposes. Harvard Soil Mechanics, Series No. 8, Cambridge, Mass.
9. Taylor, D.W., 1948. Fundamentals of Soil Mechanics. John Wiley and Sons, New York.
10. Singh, S.K., 2001. Confined aquifer parameters from temporal derivation of drawdowns. Journal of Hydraulic Engineering 127 (6), 466–470.
11. Al-Zoubi, M.S., 2004a. Coefficient of Consolidation cv from the Linear Portion of the δt− fit Curve. Proceedings of the *International Engineering Conference* (IEC 2004) at Mutah University, 26–29 April 2004, pp. 1–13.

International Journal of Engineering Research and general science is an open access peer review publication which is established for publishing the latest trends in engineering and give priority to quality papers which emphasis on basic and important concept through which there would be remarkable contribution to the research arena and also publish the genuine research work in the field of science, engineering and technologies

International Journal Of Engineering Research and General Science

ISSN 2091 - 2730